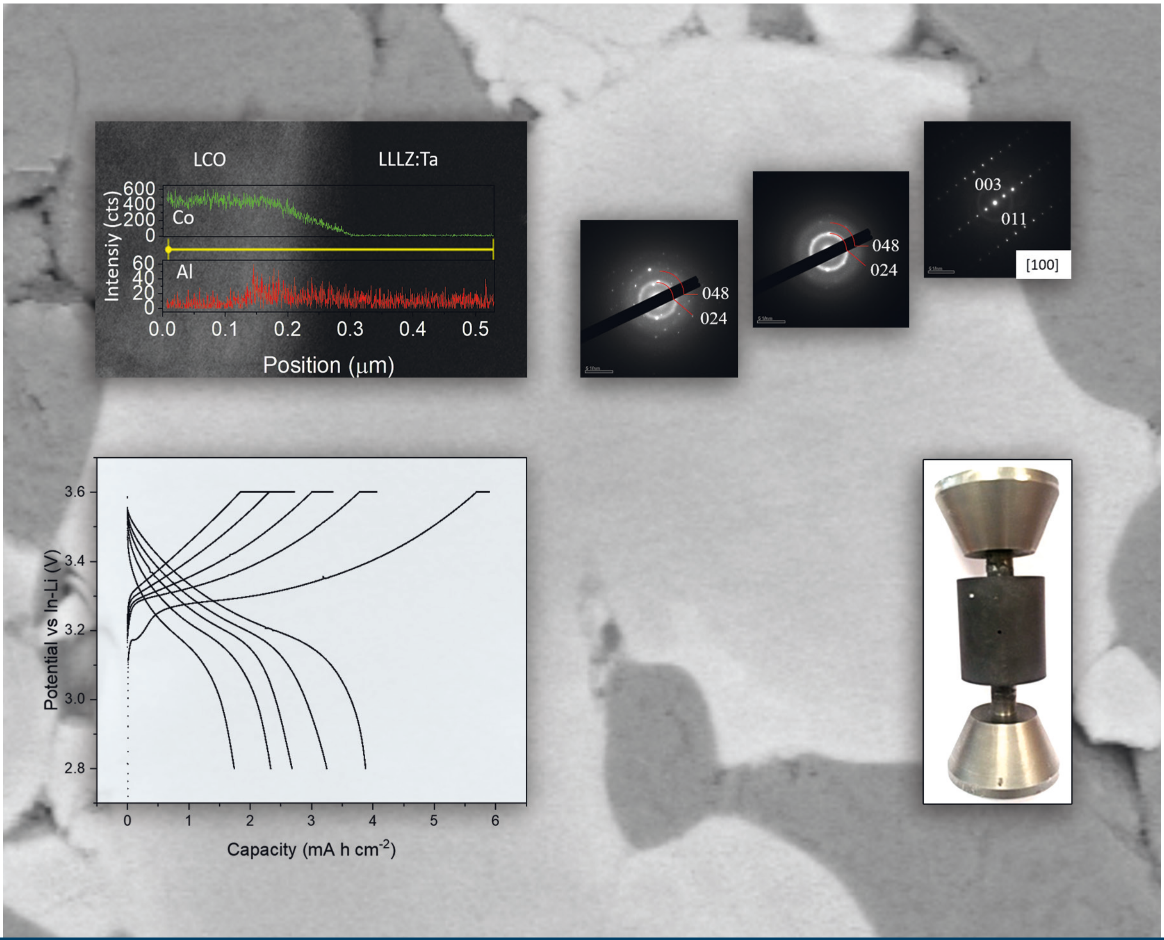

Advanced Sintering of Garnet-Based Ceramic Composite Cathodes for All-Solid-State Lithium Batteries

Martin Ihrig

Energie & Umwelt / Energy & Environment
Band / Volume 571
ISBN 978-3-95806-616-8

Mitglied der Helmholtz-Gemeinschaft

JÜLICH
Forschungszentrum

Schriften des Forschungszentrums Jülich
Reihe Energie & Umwelt / Energy & Environment Band / Volume 571

Forschungszentrum Jülich GmbH
Institut für Energie- und Klimaforschung
Werkstoffsynthese und Herstellungsverfahren (IEK-1)

Advanced Sintering of Garnet-Based Ceramic Composite Cathodes for All-Solid-State Lithium Batteries

Martin Ihrig

Schriften des Forschungszentrums Jülich
Reihe Energie & Umwelt / Energy & Environment Band / Volume 571

ISSN 1866-1793 ISBN 978-3-95806-616-8

Bibliografische Information der Deutschen Nationalbibliothek.
Die Deutsche Nationalbibliothek verzeichnet diese Publikation in der Deutschen Nationalbibliografie; detaillierte Bibliografische Daten sind im Internet über http://dnb.d-nb.de abrufbar.

Herausgeber und Vertrieb: Forschungszentrum Jülich GmbH
Zentralbibliothek, Verlag
52425 Jülich
Tel.: +49 2461 61-5368
Fax: +49 2461 61-6103
zb-publikation@fz-juelich.de
www.fz-juelich.de/zb

Umschlaggestaltung: Grafische Medien, Forschungszentrum Jülich GmbH

Druck: Grafische Medien, Forschungszentrum Jülich GmbH

Schriften des Forschungszentrums Jülich
Reihe Energie & Umwelt / Energy & Environment, Band / Volume 571

D 82 (Diss. RWTH Aachen University, 2021)

ISSN 1866-1793
ISBN 978-3-95806-616-8

Abstract

Oxide-ceramic based All-Solid-State Lithium Batteries (ASSLBs) can provide high intrinsic safety, extended operational temperature range, and high energy density. As the first two are intrinsic to the materials system, one prerequisite to obtain high energy densities with such ASSLBs is the manufacturing of thick, mixed electronic and ionic conductive composite cathodes, analogous to those of conventional liquid electrolyte-based lithium batteries. The preparation of composite cathodes using oxide-ceramic electrolytes is challenging since high temperature sintering steps are necessary during electrode and cell manufacturing to achieve proper mechanical stability, contact between the individual phases, and good ionic and electronic conductivity. Since oxide-based electrolyte materials like $Li_7La_3Zr_2O_{12}$ (LLZ) require sintering temperatures above 1050 °C, they often exceed the thermal stability windows of the cathode active materials like spinels (e.g. $Li_2NiMn_3O_8$) or layered materials (e.g. $Li[Ni_{1-x-y}Co_xMn_y]O_2$ and $LiCoO_2$ (LCO)). One well established method to achieve consolidation at lower temperatures is high-pressure assisted Field-Assisted Sintering Technique/Spark Plasma Sintering (FAST/SPS).

The first part of this dissertation will focus on the material selection and show that LCO is compatible with LLZ. Through the application of high-pressure assisted FAST/SPS, the sintering temperature was reduced to 675 °C – 750 °C and the dwell time to 10 minutes, reaching a relative density of 95 % for LCO/LLZ pellets. The high mechanical pressure was found to be a crucial factor for achievement of high density and phase purity. However, low sintering temperature leads to a significant influence of surface impurities in the initial powders and influences the crystallinity and impedance of the sintered LCO/LLZ interface. Therefore, a special heat treatment for the cleaning of the starting powders and post-sintering annealing was conducted. The annealed composite cathode can provide a high areal capacity in fully inorganic and polymer-ceramic ASSLBs.

The all-solid-state composite cathode with rigid interfaces is mechanically stable during electrochemical cycling, which is attributed to the high relative density of the cathodes achieved via FAST/SPS processing. Although, no mechanical degradation is observed, the composite cathodes show a fading electrochemical performance due to increasing LCO/LLZ:Ta interface impedance while cycling. Detailed interface characterization and thermodynamic calculations imply an electrochemical driven Al-Co exchange that can explain the fading electrochemical performance. A subsequent thermal annealing step helps to nearly fully recover the electrochemical performance of the composite cathode.

Kurzfassung

Oxidkeramik-basierte Festkörper-Lithium-Batterien (ASSLBs) bieten ein hohes Sicherheitslevel, einen breiteren Betriebstemperaturbereich und eine hohe Energiedichte. Da die ersten beiden Punkte intrinsisch sind, ist eine Voraussetzung zur Erzielung hoher Energiedichten mit solchen ASSLBs die Herstellung von dicken, ionisch und elektronisch leitenden Verbundkathoden, analog zu denen von konventionellen Lithiumbatterien auf Flüssigelektrolytbasis. Die Herstellung von Kompositkathoden mit oxidkeramischen Elektrolyten ist eine Herausforderung, da bei der Elektroden- und Zellherstellung Sinterschritte bei hohen Temperaturen notwendig sind, um eine gute mechanische Stabilität sowie einen guten Kontakt zwischen den einzelnen Phasen und dadurch eine gute ionische und elektronische Leitfähigkeit zu erreichen. Da oxidbasierte Elektrolytmaterialien wie $Li_7La_3Zr_2O_{12}$ (LLZ) hohe Sintertemperaturen erfordern, überschreiten sie oft die thermischen Stabilitätsfenster der kathodenaktiven Materialien wie Spinelle (z. B. $Li_2NiMn_3O_8$) oder Schichtmaterialien (z. B. $Li[Ni_{1-x-y}Co_xMn_y]O_2$ und $LiCoO_2$ (LCO)). Eine etablierte Methode, um eine Verdichtung bei niedrigeren Temperaturen zu erreichen, ist die Feld-Aktiviertes Sintertechnik/ Spark Plasma Sintering (FAST/SPS) unter hohem mechanischen Druck.

Der erste Teil der Arbeit konzentriert sich auf die Materialauswahl und zeigt, dass die kompatibelsten Materialien, LCO un LLZ sind. Durch die Anwendung des Druck-gestützten FAST/SPS Prozesses wurde die Sintertemperatur auf 675 - 750 °C und die Sinterdauer auf 10 Minuten reduziert, wodurch eine relative Dichte von 95 % für LCO/LLZ-Pellets erreicht wurde. Es zeigte sich, dass der hohe mechanische Druck ein entscheidender Faktor für das Erreichen einer hohen Dichte und Phasenreinheit ist. Die niedrige Sintertemperatur führt jedoch zu einem erheblichen Einfluss von Oberflächenverunreinigungen im Ausgangspulver mit Auswirkung auf die Kristallinität und Impedanz der gesinterten LCO/LLZ-Grenzfläche. Daher wurden eine spezielle Reinigungswärmebehandlung der Ausgangspulver und eine Glühung nach dem Sintern durchgeführt. Die thermisch nachbehandelte Kompositekathode weist eine hohe Flächenkapazität in inorganischen und polymer-keramischen ASSLBs auf.

Die Festköper-Kompositkathode mit starren Grenzflächen ist beim elektrochemischen Zyklieren mechanisch stabil, was auf die hohe relative Dichte der Kathoden zurückgeführt wird, die durch FAST/SPS erreicht wurde. Obwohl keine mechanische Degradation beobachtet wird, zeigen die Kompositkathoden eine nachlassende elektrochemische Leistung aufgrund der steigenden LCO/LLZ:Ta-Grenzflächenimpedanz während der Zyklierung. Eine detaillierte Grenzflächencharakterisierung sowie thermodynamische Berechnungen ergaben, dass ein elektrochemisch getriebener Al-Co-Austausch eine Erklärung für die nachlassende elektrochemische Leistung liefert. Ein anschließender thermischer Ausheilungsschritt kann die elektrochemische Leistung der Kompositkathode nahezu vollständig wiederherstellen.

List of Abbreviations

ASR	Area-Specific Resistance
ASSLB	All-Solid-State Lithium Battery
AC	Alternating Current
b	bulk
CAM	Cathode Active Material
CC-CV	Constant-Current-Constant-Voltage
CE	Coulombic Efficiency
***c*-LLZ**	Cubic $Li_7La_3Zr_2O_{12}$
CPE	Constant Phase Element
DC	Direct Current
DFT	Density-Functional Theory
DTA	Differential Thermal Analysis
EDX	Energy Dispersive X-ray spectroscopy
EIS	Electrochemical Impedance Spectroscopy
FAST/SPS	Field-Assisted Sintering Technique/Spark Plasma Sintering
G	Graphite foil
gb	grain boundary
HOMO	Highest Occupied Molecular Orbital
HT	High-Temperature
ICDD	International Centre for Diffraction Data
ICSD	Inorganic Crystal Structure Database
IR	Internal Resistance
IoT	Internet of Things
LATP	$Li_{1.5}Al_{0.5}Ti_{1.5}(PO_4)_3$
LCO	$LiCoO_2$
LIB	Li-Ion Battery
LLZ	$Li_7La_3Zr_2O_{12}$
LLZ:Ta	$Li_{6.45}Al_{0.05}La_3Zr_{1.6}Ta_{0.4}O_{12}$ (with clean surface)
LLZ:Ta-air	$Li_{6.45}Al_{0.05}La_3Zr_{1.6}Ta_{0.4}O_{12}$ (exposed to air)
LT	Low Temperature
LUMO	Lowest Unoccupied Molecular Orbital
MEEP	poly[bis(2-(2-MethoxyEthoxy)Ethoxy)Phosphazene]
MH	Metal Hydride
MNO	$LiMn_{1.5}Ni_{0.5}O_4$
NCA	$Li_2Ni_xCo_yAl_zO_2$
NMC	$Li_2Ni_xCo_yMn_zO_2$
NMC:Mg	Mg stabilized $LiNi_{0.33}Mn_{0.33}Co_{0.33}O_2$
NMC:MgAl	Mg and Al stabilized $LiNi_{0.33}Mn_{0.33}Co_{0.33}O_2$
NMO	$Li_2Ni_{1-x}Mn_yO_2$
OCV	Open Circuit Voltage
PBE	Perdew-Burke-Ernzerhof
ppm	parts per million
ppb	parts per billion
PSD	Particle Size Distribution
QMID	Quasi Multiple Ion Detection
RT	Room Temperature
SAED	Selected Area Electron Diffraction
SDD	Spin Density Distribution

SEI	Solid Electrolyte Interface
SEM	Scanning Electron Microscopy
SoC	State of Charge
TEM	Transmission Electron Microscopy
TGA	Thermogravimetric Analysis
ToF-SIMS	Time of Flight-Secondary-Ion Mass Spectrometry
TZM	Molybdenum based alloy
UHS	Ultra-fast High-temperature Sintering
VASP	Vienna Ab initio Simulation Package
vol	Volume
wt	Weight
XC	Exchange-Correlation
XRD	X-Ray Diffraction

Table of Contents

1. Motivation and Introduction

Batteries are electrochemical devices that are the dominant form for storage of electrical energy. By now, many types of batteries have been developed and commercialized. Nowadays, the most commonly used amongst them, Li-ion batteries, are characterized by their enhanced energy storage capacity (Fig. 1.1), low weight, and long lifetime [1-4]. Li-ion batteries are broadly used in portable electronics, power tools, and electric mobility.

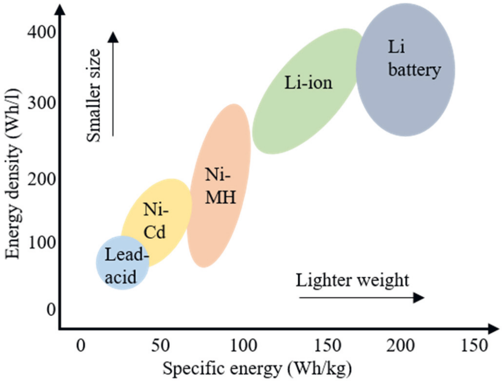

Fig. 1.1. Overview of volumetric and gravimetric energy density for batteries of various type (MH: Metal Hydride) [5].

Since their commercialization in 1991, Li-ion batteries have remarkably improved with respect to their electrochemical performance and production cost. While there is still optimization potential left, upcoming applications, e.g. the electric powered transportation and small remote devices for the internet of things, require new concepts of Li-ion batteries that provide a higher power and energy density, and prolonged lifetime under harsh conditions [6].

Another new and prospective application of Li-ion batteries is in stationary electrical energy storage facilities. Large-scale Li-ion batteries can be used to store surplus electrical energy irregularly produced by renewable energy sources [7]. The large-scale Li-ion batteries can stabilize the grid loading and thus prevent a possible blackout. In addition, new large-scale and environment friendly Li-ion batteries can be used in battery powered electric vehicles.

However, with the upscaling of Li-ion batteries, the enhanced energy density and safety concerns due to the use of flammable liquid electrolytes have to be addressed in the next battery generation. In this regard, All-Solid-State Lithium Batteries (ASSLBs) on the basis of oxide-ceramics attract the attention of researchers and engineers owing to their intrinsic safety, extended operational temperature range, and potential to achieve higher energy densities [2-4, 8-12]. One of the most prospective solid electrolytes is the garnet-type $Li_7La_3Zr_2O_{12}$ (LLZ) ceramic [3, 13, 14]. High ionic conductivity makes LLZ very promising for ASSLB application. However, the challenges during processing of LLZ ceramic and following integration into an electrochemical cell hampers the application of LLZ-based ASSLBs. Furthermore, to achieve a high energy density in ceramic ASSLB, the cathode structure has to provide a high areal capacity and an enhanced utilization of the Cathode Active Material (CAM), which requires an efficient conduction of electrons and Li-ions. The high energy density can be achieved by creation of an intertwined 3D network of CAM and solid electrolyte with well-developed contact between them. In general, the CAM/solid electrolyte interface has to possess a high total area with a low impedance to allow an efficient charge and Li-ion transport with minimum resistance losses in the battery. In conventional Li-ion batteries with liquid electrolyte, the infiltration of electrolyte into a porous CAM structure leads to spontaneous formation of a CAM/electrolyte interface. This infiltration is not realizable with solid electrolytes (e.g. LLZ). Therefore, other approaches for the improvement of the CAM/electrolyte interface in composite cathode have to be explored. One possibility to manufacture composite cathodes with high electrochemical performance is the co-sintering of LLZ and CAM powder mixtures.

In order to achieve a good contact between individual LLZ grains and to reach a desirable ionic conductivity, a sintering temperature above 1050 °C with a dwell time of a couple of hours is usually required [14]. This raises the question of stability of LLZ and CAM phases during sintering. However, the mixtures of LLZ and promising CAMs for Li-ion batteries, such as $Li[Ni_{1-x-y}Co_xMn_y]O_2$ (NMC) or $Li_2Ni_{1-x}Mn_yO_2$ (NMO) have a reduced thermodynamic stability [15]. The oxidizing nature of CAMs promotes the reaction with LLZ already at approximately 700 °C for NMC and at 500 °C for NMO, which is far below the sintering temperature of LLZ [16].

Some research groups have shown that control of the sintering kinetics, i.e. by a reduction of sintering time, or careful control of powder morphology and composition can help to overcome or to circumvent these thermodynamic restrictions [17-20]. Some published co-sintered composite cathodes show greatly increased CAM utilization and improved charge transport compared to pure CAM cathodes [21-25]. However, despite the achieved progress, the formation of secondary phases during processing on the CAM/solid electrolyte interface remains a serious limitation for cathode performance [10, 11, 15, 16, 26-28]. Additionally, the volume change of CAM during electrochemical cycling leads to fracturing. The fracturing is a reason of the high residual porosity of 20 % often obtained in conventional free sintered composite cathodes manufactured via a slurry-based route [18].

As mentioned above, the kinetics of side reactions can be effectively controlled by the schedule of thermal treatment. In particular, faster processing with higher heating and cooling rates, and shorter dwell time combined with lower sintering temperature can lead to a reduction in secondary phase formation. A decrease in sintering temperature and sintering time can be achieved by application of sintering aids or by coating of pristine CAM particles, for example with an Nb- or Li_3BO_3 layer [28,30]. However, the grain boundary composition is also altered, which often leads to an increase in interfacial resistance. For example, Li_3BO_3 has a Li-ionic conductivity of only 10^{-6} S cm^{-1} at Room Temperature (RT) which is much lower than that of LLZ (approximately 10^{-4} S cm^{-1} at RT [14, 29]). Thus, Li_3BO_3 layer limits the charge transfer across the CAM/solid electrolyte interface [30]. In order to avoid the use of sintering additives while maintaining reduced sintering temperatures and dwell times, advanced sintering technologies like the Field-Assisted Sintering Technique/Spark Plasma Sintering (FAST/SPS) can be used [17, 31]. By applying direct Joule heating and mechanical pressure, FAST/SPS enables sintering of dense ceramics at lower temperature and with significantly shorter dwell time as compared to conventional free sintering [17, 28, 31-38].

The motivation of this dissertation is to develop a FAST/SPS-based process for manufacturing a dense bulk composite cathode and half cells (composite cathode and separator) for garnet LLZ-based ASSLBs and its structural and electrochemical characterization. Additionally, a new polymer-ceramic ASSLB concept and a novel sintering technique will be introduced and shortly discussed. The dissertation is subdivided into four main parts:

i) The selection of a CAM suitable for co-sintering with LLZ and the development of a reliable FAST/SPS sintering process.

ii) The preparation of an ASSLB based on the FAST/SPS sintered composite cathode and its structural and electrochemical evaluation. The explanation of observed electrochemical performance and the optimization of manufacturing route for composite cathode.

iii) The development and evaluation of a possible approach to recover the electrochemical performance of a LLZ/LCO composite cathode after electrochemical cycling.

iv) The preparation and evaluation of a polymer-ceramic cell concept with increased areal capacities.

2. Literature Overview

2.1. Sintering

Sintering is the process of consolidation of metallic or ceramic powders, or powder mixtures to a solid body by means of heat below the melting point of the primary constituent in a powder mixture. When all mixture components remain solid, the sintering process is named solid-state sintering [39-41]. If the sintering temperature exceeds the melting point of a secondary component in the mixture, the process is defined as liquid-phase sintering. In the present work only, solid-state sintering was used. Hence, in the following the expression “sintering” always refers to the solid-state sintering.

The driving force for sintering is the decrease of free energy of the powder system [41]. During sintering the pores between particles are reduced in size or eliminated with the formation of new grain boundaries, i.e. solid-solid interfaces. This leads to an increase in grain boundary energy and to a decrease in free surface energy. If the sum of these energy changes (ΔE) is negative, the material is thermodynamically prone to sintering (Eq. 2.1).

$$\Delta E = \gamma_{gb} \cdot \Delta A_{gb} + \gamma_S \cdot \Delta A_S \qquad \textbf{Eq. 2.1.}$$

Here γ_{gb} is the specific grain boundary energy; γ_S is the specific free surface energy; A represents the interface area between particle and pore (A_S) or the area of the new grain boundary (A_{gb}) [41]. Essential for sintering is the material mass transport. In general, six distinct mechanisms can contribute to sintering of powder particles: (1) vapor transport, (2) lattice diffusion from the surface, (3) lattice diffusion from the grain boundary, (4) surface diffusion, (5) plastic flow, and (6) grain boundary diffusion (Fig. 2.1) [39-41]. Besides, only lattice diffusion from the grain boundary and grain boundary diffusion (3 and 6), and plastic flow (5) lead to densification. The remaining mechanisms lead only to material redistribution.

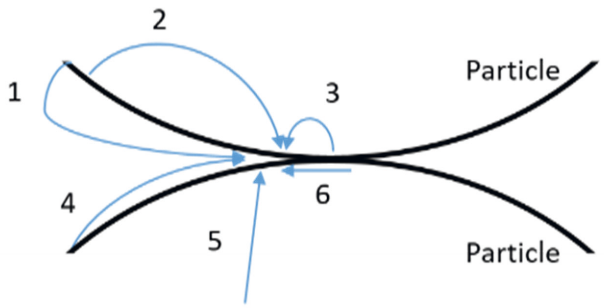

Fig. 2.1. Schematic presentation of material transfer mechanisms during sintering [41].

The sintering process is, in general, divided into three stages: initial, intermediate, and final sintering stage (Tab. 2.1) [39-41].

Initial stage: This stage is characterized by neck formation between contacting particles. During initial stage the relative density of material is increased to a value of around 65%.

Intermediate stage: In the initial stage the particles are connected only via necks. Hence, the intermediate stage starts with open porosity. The related particle structure can be idealized as a set of tetradecahedrons with cylindrical pores along the edges. Lattice and grain boundary diffusion lead to the shrinkage of pores and to densification. In course of this process, the pores become disconnected from each other resulting in a closed porosity at a relative density of 90 %.

Final stage: During the final stage the isolated pores are further reduced in size. In addition, the grain growth becomes much more intensive. Grain growth is the result of diffusion of matter from one particle to another particle. The grain growth process can be divided into normal and abnormal grain growth. In the normal grain growth, the grain number decreases, and the size of the grains is increased. The size distribution is narrow. In abnormal grain growth, larger grains grow more rapidly. This leads to a wide grain size distribution.

Tab. 2.1. Overview of sintering stages [41].

Stage	**Typical microstructural feature**	**Relative density range**	**Idealized model**
Initial	Rapid inter-particle neck growth	≤ 0.65	Two monosize spheres in contact
Intermediate	Equilibrium pore shape with continuous porosity	0.65-0.90	Tetradecahedron with cylindrical pores of the same radius along the edges
Final	Equilibrium pore shape with isolated porosity	> 0.90	Tetradecahedron with spherical monosize pores at the corners

The final density and the microstructure define the main properties of the sintered body. Through control of the sintering variables, the reproducibility and the desired microstructure design can be achieved. This means that the sintered density (or porosity), grain size, and to some extent phase composition are controllable.

Sintering is realized in many different technologies: free sintering, hot pressing, hot isostatic pressing, microwave sintering, etc. [41]. This work will focus on sintering of oxide-ceramics for battery application by Field-Assisted-Sintering-Technique (FAST), which is also known as

Spark Plasma Sintering (SPS). FAST/SPS represents an advanced sintering technology that combines fast Joule heating, application of external mechanical pressure, and electric field to accelerate the sintering process (described in section 2.2) [31, 32, 35].

2.1.1. Powder material properties

The grain size is an essential property for sintering. The driving force for sintering is the reduction of interface/surface energy. Smaller grains have higher specific surface area and consequently higher surface energy. According to Herring the sintering rate in grain boundary diffusion controlled densification is proportional to 1/(grain size)^4 and, therefore, highly dependent on the grain size [41, 42].

Smaller grain sizes show significantly enhanced sintering. Thus, either the sintering temperature can be reduced, or the dwell time can be shortened. However, smaller grains tend to agglomeration [41]. The grains will sinter firstly within agglomerates, then the agglomerates will sinter with other agglomerates. In such a case, the sintering is controlled by agglomerate properties and sizes. An optimal grain size has to be found at which the agglomerate formation is negligible, and the sintering properties are acceptable. Simply decreasing the grain size might not be beneficial [39]. In the case of agglomeration, the advantage of smaller grain sizes is less, can fully disappear, or even lead to retarded sintering. Besides, small grains show increased grain growth and the same negative effect on sintering can be observed. In FAST/SPS the applied external mechanical pressure can break usually soft agglomerates and agglomerate formation might be less problematic in comparison to free sintering [32].

Besides the grain size, the morphology of primary particles can influence the sintering. The sintering process has to form junctions between grains. Therefore, the grains have to be packed closely. An applied external pressure, as in the case of FAST/SPS, can lead to closer packed grains and assist the sintering.

2.1.2. Constrained sintering

Inhomogeneity within the powder can impact the sintering behavior [39-41]. An inhomogeneity source, for example, can be a second phase in a powder mixture. The presence of a second phase powder can interfere with the densification process of the matrix (primary) phase (Fig. 2.2). During solid state sintering the densification can be significantly reduced or even completely inhibited depending on the volume fraction of the second phase. Furthermore, the interface to the second phase can be the origin of cracks due to transient stresses. Transient stresses result from: i) different sintering kinetics of two phases, ii) formation of a rigid percolation network, and iii) the sintering behavior of individual particles can depend on the surrounding microstructure and lead to differential densification (Fig. 2.2).

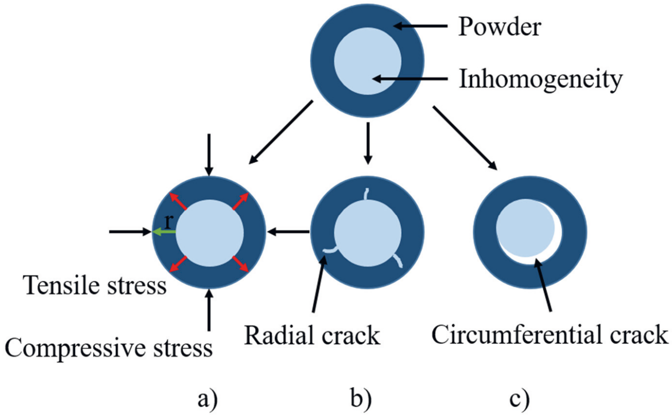

Fig. 2.2. Schematic diagram illustrating the effects of inhomogeneity in a powder: a) reduced densification (r represents the distance), b) growth of radial flaw due to a lower sintering inhomogeneity, and c) circumferential flaw due to larger sintering rate of the internal inhomogeneity [41].

The conventional theories developed for the sintering of powder mixtures are inapplicable here, as the rigid inclusions lead to major deviations [39-41]. Lower shrinkage rate of matrix surrounding an inclusion leads to the development of mechanical stresses. The stresses are compressive for the inclusion and tensile for the matrix, which is highest at the interface and decreases with increasing distance (r) by a factor of r^{-3} (Fig. 2.2a) [41].

The use of a pure viscoelastic model to simulate the sintering will lead to the prediction of unreasonably high stress [41]. Therefore, two models, the self-consistent calculation and composite sphere model, were developed to describe constrained sintering.

2.1.2.1. Self-consistent calculation

This model assumes that the inclusions forms islands in a continuum basic material, in which the powder inclusions contract with a slower rate (Fig. 2.3a) [41]. The model is only applicable to small volume fractions of rigid inclusions below 20 vol-%, as forces between the inclusions are not considered. The stress in an isolated inclusion can be calculated from the solution by Selsing [41, 43]. Using these results and the constitutive equation for the matrix phase, it is possible to calculate the sintering rates.

2.1.2.2. Composite sphere

This model assumes, that the inclusions are well dispersed within the matrix powder (Fig. 2.3b) [41]. While sintering, different shrinkage rate of the cladding/matrix and the core/inclusion leads to compressive stress within the core and to compressive radial stress and tangential tensile stress within the cladding. These stresses reduce the densification rates of the composite. Viscous flow or creep will always seek to relieve the stresses, so the model requires a time-dependent viscoelastic solution. However, the elastic strain is much smaller than the strains observed during sintering, so the observed deformation results almost entirely from viscous flow. Due to this Scherer and Bordia developed a model based solely on viscous response of the sintering material [41, 44-46]. Experimental tests of this theory showed that the model performs well if the amount of rigid inclusions is below 15 vol-% but significantly underestimated the effects of the inclusions at higher volume fractions [41].

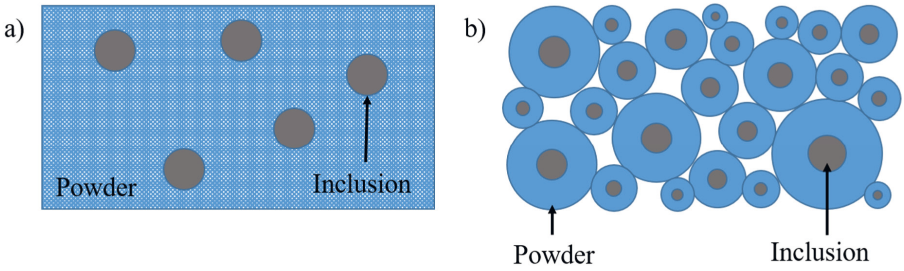

Fig. 2.3. a) Composite in which inclusions prevent the powder matrix from sintering freely [41]. b) Composite containing spherical inclusions is conceptually divided into composite spheres (cross-sectional view) [47]. Each sphere is chosen to have the same volume fraction of inclusion.

2.1.3. Percolation and Network Formation

In an ASSLB, high ionic conductivity of the electrolyte and high ionic and electronic conductivity of the electrodes is required. Thus, the amount of inclusions must be high enough for percolation and network formation. In other words, the amount of inclusions must provide a number of inclusion-inclusion contacts sufficient to produce a continuous network across the entire sample volume [41]. The ratio at which such a continuous network forms is called percolation threshold. The percolation threshold depends on the shape and dimensionality of the particles. For example, in a 3-dimensional solid, the percolation threshold is reached with a volume fraction of particles in a fully dense sample of around 16 vol-% [41]. This value varies with the relative density and grain size of the powder as pores or large particles can block percolation pathways [41].

The effect of percolation on the stiffness of the composite is an important factor since this will influence the sintering kinetics [41]. If inclusions are bonded together, the stiffness of composite will drastically increase after the percolation threshold, and alter the sintering rate, thereby affecting the densification. Depending on the interaction between the rigid inclusions and the powder matrix, the densification might be limited to a lower level or even have increased rate [41].

The simulation of the densification process is challenging, as it requires material properties of the primary phase and the rigid inclusion that are difficult to measure or estimate at the percolation threshold concentration [41].

2.2. Field-assisted-sintering-technique/Spark-plasma-sintering

2.2.1. Overview

FAST/SPS is a low voltage, pulsed Direct Current (DC) activated, pressure assisted sintering technique [32, 35, 48, 49]. In the FAST/SPS setup the powder sample is placed in a mold and external mechanical pressure is applied via two punches (Fig. 2.4). The FAST/SPS setup is, therefore, similar to hot pressing but differs in heat generation and transfer. Hot pressing heats the pressing tools by radiation, while in FAST/SPS Joule heating produced by a pulsed or continuous current is used. Thus, the heat is generated either in the pressing tools (typically graphite-based tools) or in the case of a conductive sample, within the sample itself. Due to the low electrical resistance of the FAST/SPS circuit, a voltage below 10 V can produce a high current in the kA-range that provides heating rates up to 1000 K/min [32, 35].

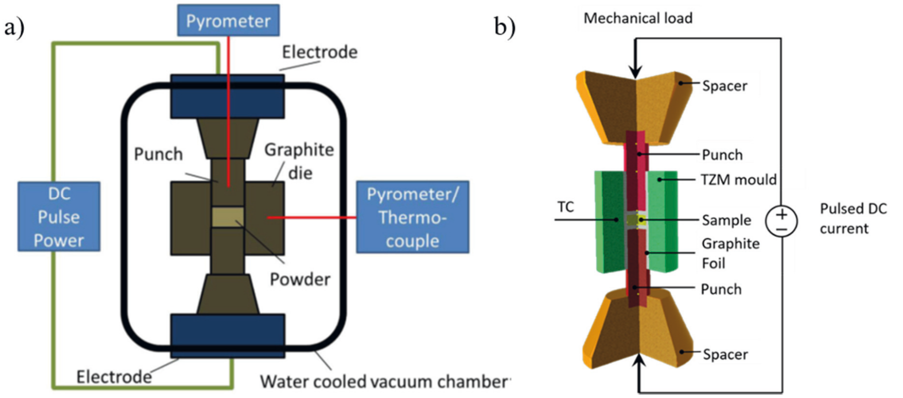

Fig. 2.4. a) Schematic view of the FAST/SPS apparatus [32]. b) The detailed view of the sintering tool [17].

FAST/SPS is beneficial for sintering processes [31, 32, 35, 48]. First, Joule heating during FAST/SPS allows a high heating rate and lowers the total time of the sintering process. A typical FAST/SPS sintering cycle is usually completed within minutes. This is much shorter compared to conventional sintering which often requires heating and sintering for hours. Second, materials can be sintered with FAST/SPS at a significantly lower temperature than with conventional free sintering due to the applied mechanical pressure [31]. Therefore, one of the strengths of the FAST/SPS process is the possibility of co-sintering of materials with different sintering or decomposition temperatures [50, 51]. In addition, inter-diffusion processes, that lead to secondary phases, may be suppressed due to short dwell time and low sintering temperature [32]. In order to optimize the co-sintering process by FAST/SPS multiple parameters have to be considered.

2.2.2. Parameters of the FAST/SPS process

2.2.2.1. Atmosphere

The atmosphere during the sintering process can influence defect formation and diffusion in the sintering material [32, 35]. This has an impact on the densification kinetics, grain growth, phase stability, and material stoichiometry. Gas adsorption on the particles can also change the thermodynamics as the free surface energy is altered. To avoid such changes and due to the graphite foil used in the tools, normally the FAST/SPS process is conducted under vacuum (around 10^{-3} bar) [49, 52, 53]. For Li-based materials the vacuum is challenging. Li is rather volatile at elevated temperatures and the low pressure in the sintering chamber will lead to Li losses in the materials [17].

Other atmospheres, commonly used in FAST/SPS, are Ar or N_2 [32, 35]. The gas pressure can be 1 bar or less. Hydrogen containing atmospheres are not suitable for sintering of oxide-ceramics, such as LLZ, as such atmospheres would strongly reduce them. Oxygen-based atmospheres are possible but require special oxidation-free tools [32].

As the sample is placed in a closed die, the local atmospheric conditions at the sample can differ from the applied atmosphere and could also be influenced by the material of the FAST/SPS setup [54].

2.2.2.2. Heating rate

One unique characteristic of the FAST/SPS process is the high heating rate up to 1000 K min^{-1} [32, 35, 48]. However, rapid heating can lead to an uncertainty in temperature measurement. The temperature during FAST/SPS is measured with a pyrometer, a thermocouple, or both (Fig. 2.4). The pyrometer measures the temperature of the focus area on the mold or punches and the thermocouple measures the temperature within the mold.

As FAST/SPS uses Joule heating, two effects have to be considered [32, 35, 48]. In the case of a conductive sample an internal heating is observed. The heat is distributed from the inside of the sample and the measured temperature at the mold or punches will be lower than the sample temperature. For a nonconductive sample, such as LLZ, Joule heating will lead to higher temperatures in the pressing tools than in the sample. The difference of the measured and actual temperature can, therefore, depend on the sample geometry and properties varying up to 100 K [32, 55]. With lower heating rates the temperature difference could be decreased. However, higher heating rates are expected to lead for nonconductive powder to higher density and lower grain growth. For conducting samples such an effect is often not observed [32].

Therefore, the heating rate has to be optimized based on the powder and the desired properties of the sintered body.

2.2.2.3. Electrical effects

The DC current applied during FAST/SPS sintering can be either continuous or pulsed. The pulsing current, however, has usually only a minor effect on sintering. [32, 35].

An electric current is used to produce Joule heating. The electric current flows for a conductive sample through the sample and/or through the pressing tools depending on the sample and tool conductivity. For nonconductive sample, such as LLZ, the electric current flows only through the pressing tools. In this case the effect of the electric current on the sintering process is indirect.

The electric current influences the heating of the sample but not the sintering process itself [32]. Depending on the sample geometry an inhomogeneous heating within the sample can be observed. However, for small samples (e.g. 12 mm in diameter as used in this work) the temperature inhomogeneity is relatively small [55].

Depending on the powder properties, the Peltier effect can be observed. This is mostly observed in semiconductors and is negligible for other materials [32].

Electric fields can impact material transport, grain boundary migration, and generation of lattice defects [32, 35, 48]. These effects correlate with the strength of the electric field. The applied voltage in FAST/SPS process is only around 10 V and is rather too weak for initiation of these field effects. However, materials with high-dielectric permittivity can amplify the electric field locally by several orders of magnitude at inter-particle junctions [32]. Furthermore, the properties of the sintered body could be influenced by the electric field, as was reported for gadolinium-substituted ceria which was electrochemically reduced [56].

2.2.2.4. External pressure

The external pressure enhances the densification during sintering [39-41]. The application of pressure results in densification and creep of powder material that leads to more inter-particle contacts and an increase in the driving force for sintering. Due to the increased inter-particle contacts, small external pressure can have significant impact on the driving force for sintering [41]. In addition, the external pressure can lead to grain sliding [39-41], which leads to particle rearrangement with related densification.

The external pressure can also break agglomerates and their impact on the sintering is reduced compared to free sintering without external pressure [32, 35, 48].

2.2.2.5. Dwell time

In comparison to conventional sintering the dwell times in FAST/SPS processes are rather short as a consequence of the applied external pressure and the electric field [32]. The dwell time is normally within several minutes. The optimization of the dwell time is usually performed according to the density and microstructure requirements [32, 35, 48].

2.2.3. FAST/SPS sintering of garnet-based electrolytes and composite cathodes

Requirements for all-solid-state lithium batteries are a dense and high conductive solid electrolyte, and an intimate contact between CAM and solid electrolyte to obtain low interfacial resistances. FAST/SPS has been used for sintering of many types of inorganic e.g. NASICON ($Na_{1+x}Zr_2Si_xP_{3-x}O_{12}$)-, perovskite-, and garnet-based solid electrolytes [10, 31]. As this work is focused on garnet-based LLZ electrolyte, the following discussion will be based on sintering of LLZ by FAST/SPS.

Multiple research groups have reported that FAST/SPS sintering is advantageous to increase the density of solid electrolytes in comparison to conventional free-sintering [14, 29, 31]. It is also a solvent free method to sinter LLZ powder into free-standing LLZ separator, without the requirement of pre-compaction of the powders [31]. Furthermore, it can prevent significant grain growth and lead to highly conductive grain boundaries [31]. The application of Joule heating and mechanical pressure assists the sintering process, and decreases the sintering temperature and the dwell time required in comparison to conventional sintering, while still achieving higher and more homogeneous density and similar ionic conductivity [36, 57]. One reason for this was reported by Baek et al., who reported that FAST/SPS significantly reduces or prevents grain growth in comparison to conventional sintering [57]. In the case of LLZ, densities of up to 99.8 % and a total ionic conductivity of up to 0.69 mS cm^{-1} at RT can be obtained by FAST/SPS within minutes at sintering temperatures between 900 °C and 1150 °C [36, 58].

Lower sintering temperature and shorter dwell time are beneficial in two ways. First, it can reduce the loss of volatile elements such as Li. Second, it allows the co-sintering of solid electrolytes with CAMs, as their mixture has, in general, only low thermal stability [50, 51]. Furthermore, the short dwell time will limit diffusion related secondary phase formation.

However, the FAST/SPS process can lead to the reduction of Li_2CO_3 [58], which is typically formed on LLZ exposed to ambient atmospheres (section 2.4.3), according to Eq. 2.2.

$$CO_3^{2-} + 4e^- \rightarrow C + 3O^{2-} \qquad \textbf{Eq. 2.2.}$$

The formed oxygen ions can react with Li-ions from the LLZ and form Li_2O. The removal of Li-ions from LLZ leads to the formation of non-Li-ion conductive $La_2Zr_2O_7$. This reaction can be suppressed by short dwell times, low sintering temperatures, or removal of Li_2CO_3 prior the FAST/SPS process.

Dense composite cathodes can be sintered by FAST/SPS. The majority of these composite cathodes have been co-sintered with solid electrolyte sintering at low temperatures such as $Li_{2.2}C_{0.8}B_{0.2}O_3$ or $Li_{2.5}Al_{0.5}Ge_{1.5}(PO_4)_3$ [31, 59, 60]. The assembled ASSLBs show promising electrochemical properties and stable cycle behavior [31].

Garnet LLZ-based composite cathodes are challenging to co-sinter, even by FAST/SPS, as the required sintering temperature exceeds the thermal stability limit of most CAMs [15, 16]. One strategy to further decrease the sintering temperature of LLZ in the FAST/SPS sintering process was reported by Laptev et al [17]. They applied a high mechanical pressure of 440 MPa and obtained a dense LCO/LLZ-based composite cathode. However, only limited information on electrochemical properties were reported and no information about the phases are available.

2.3. Li-ion batteries

In battery chemistry, energy of the active material is converted into electrical energy by an electrochemical redox reaction. The term battery describes the device consisting of the electrochemical cell, the housing, and the external connections. Technically, the redox reaction takes place only in the electrochemical cell. In the case of an irreversible redox reaction, the term primary battery is used as for example in alkaline (metallic Zn and MnO_2) or commercial Li-air batteries (recently, rechargeable Li-air batteries have been developed [61]). In Li-Ion batteries (LIBs), the redox reactions are, in general, reversible; hence the batteries are also known as rechargeable or secondary batteries. A Li-ion battery is a battery in which only Li-ions are found. In the case metallic Li is present in the anode, the term Li battery is used.

2.3.1. Functionality

In general, an electrochemical cell consists of two electrodes, a cathode and an anode, that are immersed in a liquid electrolyte and separated by a separator (Fig. 2.5). When using an LIB, as an example, LiC_6 is oxidized in the Li-graphite anode into Li^+ and C_6 during discharge (Eq. 2.3). The Li^+ migrates through the electrolyte to the cathode to incorporate into $Li_{1-x}CoO_2$ where Co^{4+} is reduced to Co^{3+} (Eq. 2.4). The electrodes are named after the process occurring during discharge and are kept the same during charging by the Battery Research Society even though the processes at the electrodes have switched. The redox reaction in the LIBs (shown for graphite anode and LCO cathode LIB) is always accompanied by ionic diffusion as well as volume expansion (oxidation) or contraction (reduction) due to intercalation/deintercalation of Li^+ (Eq. 2.3 to Eq. 2.5).

Anode: $x \cdot LiC_6 \rightleftharpoons x \cdot C_6 + x \cdot Li^+ + x \cdot e^-$ **Eq. 2.3.**

Cathode: $Li_{1-x}CoO_2 + x \cdot Li^+ + x \cdot e^- \rightleftharpoons LiCoO_2$ **Eq. 2.4.**

Cell reaction: $Li_{1-x}CoO_2 + x \cdot Li^+ \rightleftharpoons LiCoO_2$ **Eq. 2.5.**

The liquid electrolyte can compensate for these volume changes, but for rigid solid electrolytes these are the major drawbacks for successful long-term battery application [62]. The electrodes can store the Li or Li^+ either by i) alloying (i.e. In), ii) conversion (i.e. Si-based), or iii) intercalation (i.e. $LiCoO_2$) [63, 64]. The storage of Li or Li^+ is described in detail in section 2.4.1 for the anode and in section 2.4.2 for the cathode.

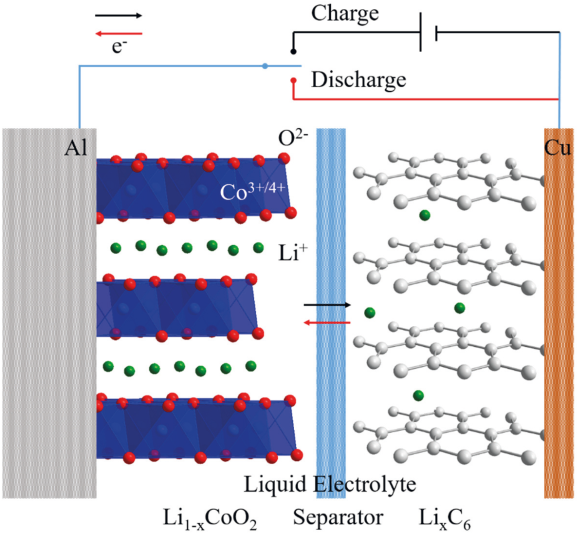

Fig. 2.5. Schematic of the electrochemical cell for graphite anode and LCO cathode LIB. The movement of electrons and Li^+ during charge and discharge are shown [64]. The current collectors are Al on the cathode side and Cu on the anode side. Different current collector materials are required to prevent their reduction or oxidation during cycling [65].

The choice of anode, electrolyte, and cathode determines the energy density of the battery. Energy density limitation occurs in general within the cathode due to lower Li^+ storage capacity than the anode (section 2.4.1 and 2.4.2). The Li^+ storage capacity (C_{sp}) and the discharge potential of the cell (V_d) are commonly used to calculate the theoretical energy density ($\rho_{E,theo}$) (Eq. 2.6).

$$p_{E,theo} = C_{sp} \cdot V_d \; [\mathrm{Wh\,l^{-1}}] \text{ or } [\mathrm{Wh\,kg^{-1}}] \qquad \textbf{Eq. 2.6.}$$

In Ragone plots different materials or even battery types can be compared graphically and suitable anode and cathode material combinations can be found (Fig. 2.6) [5]. Suitable anode and cathode combinations should, in order to obtain a high energy density, have a large difference in chemical potential.

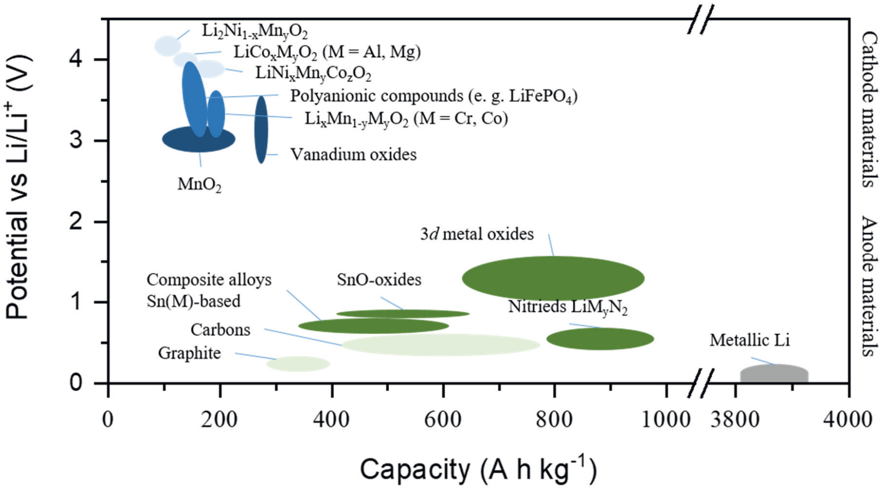

Fig. 2.6. Ragone plot (voltage vs capacity) for cathode and anode materials for present and next generation Li-ion batteries [5].

Based on the difference in chemical potential between the anode material (μ_a) and cathode material (μ_c), and the magnitude of charge (e), the open circuit voltage (V_{OCV}) can be calculated with Eq. 2.7.

$$V_{OCV} = \frac{\mu_a - \mu_c}{e} \qquad \textbf{Eq. 2.7.}$$

The Open Circuit Voltage (V_{OCV}) of a proper working battery cell is limited by the electrochemical window of the electrolyte (Fig. 2.7a). The electrochemical window is defined by the energy gap between the Highest Occupied Molecular Orbital (HOMO) and the Lowest Unoccupied Molecular Orbital (LUMO) of the material. The electrochemical potential of the anode has to be below the LUMO, while that for the cathode has to be above the HOMO of the used electrolyte. Otherwise, the electrolyte will be reduced by the anode or oxidized by the cathode. The formation of interfaces between the electrolyte and electrode can stabilize the open circuit voltage (V_{OCV}) of the battery cell but lead to higher internal resistance of the battery cell, which reduces the overall energy density [66].

Additionally, the $O^{2}:2p^{6}$ band also determines the achievable voltage in oxide materials (Fig. 2.7b) [64]. For example, in Li transition metal-based cathodes such as $LiCoO_2$, the energy of the transition metal Co^{3+}/Co^{4+} band has to be higher than the p-band of the O^{2-} anion during the whole charge/discharge process, as otherwise O_2 will be formed. In the case that the Li concentration in $Li_{1-x}CoO_2$ is lower than 0.5 ($x > 0.5$) the electrons can be removed from the $O^{2}:2p^{6}$ band rather than from the Co^{3+}/Co^{4} band since the Co^{3+}/Co^{4} band overlaps with the

O^2:2p^6 band. This results in oxygen release from the structure and can destroy the electrochemical cell.

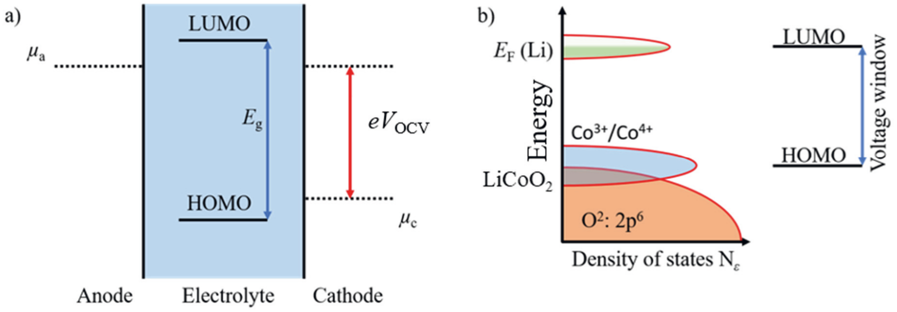

Fig. 2.7. a) Schematic of the electrochemical window of the electrolyte and the chemical potential of the anode and cathode and the resulting open circuit voltage [64]. b) Energy diagram of the electrochemical potential of a LIB with metallic Li anode and $LiCoO_2$ as cathode and the electrochemical window of the electrolyte [64].

The actual measured open circuit voltage is also called operating voltage (V_{OP}) and can be smaller than the theoretical one due to the Internal Resistance of the cell (IR_{cell}, Eq. 2.8)

$$V_{OP} = V_{OCV} - IR_{cell} \qquad \textbf{Eq. 2.8.}$$

Internal resistance of the cell is caused by activation polarization (η_{act}), ohmic polarization (η_Ω) and concentration polarization (η_{Pol}) (Fig. 2.8a). The polarization effects will lead to a potential hysteresis for charge and discharge. While the potential is decreased for discharge, it is increased for charge (Fig. 2.8b). But also, the overpotential for de-/lithiation of the cathode and anode will lead to a potential hysteresis and add to the internal resistance of the cell.

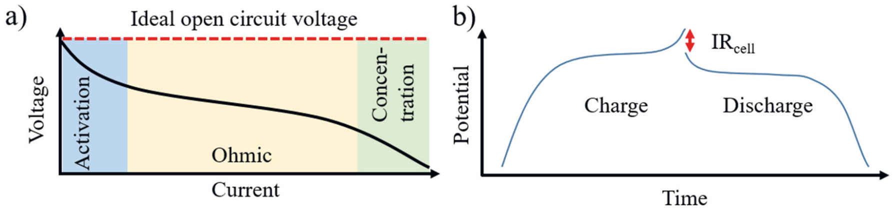

Fig. 2.8. a) The actual measured open circuit voltage V_{OC} is decreased by the activation polarization (η_{act}), the ohmic polarization (η_Ω) and the concentration polarization (η_{Pol}) [67]. b) Internal resistance of the cell (IR_{cell}) will lead to a potential hysteresis during charge and discharge [64].

As current flows in or out of the cell, the voltage will change. The cut off voltages define the charge and discharge capacity. The capacity is either based on the volume (V_c) or mass (m_c) of the limiting active material, or the electrode area (A_e). The capacity (C) of the cell can be calculated through Eq. 2.9 to Eq. 2.11 by the current (*I*) and the duration of charge or discharge (difference between t_0 and t_1).

Volumetric: $$C = \frac{\int_{t_0}^{t_1} I}{V_\mathrm{c}} \; [\mathrm{mAh\ cm^{-3}}] \qquad \textbf{Eq. 2.9.}$$

Gravimetric: $$C = \frac{\int_{t_0}^{t_1} I}{m_\mathrm{c}} \; [\mathrm{mAh\ g^{-1}}] \qquad \textbf{Eq. 2.10.}$$

Areal: $$C = \frac{\int_{t_0}^{t_1} I}{A_\mathrm{e}} \; [\mathrm{mAh\ cm^{-2}}] \qquad \textbf{Eq. 2.11.}$$

In order to compare different battery types, the real energy density (ρ_E) should be considered. The real energy density (ρ_E) is calculated by Eq. 2.12 with the help of the capacity (*C*) and the actual measured open circuit voltage (V_OP).

$$p_\mathrm{E} = C \cdot V_\mathrm{OP} \; [\mathrm{Wh\ cm^{-3}}] \text{ or } [\mathrm{Wh\ g^{-1}}] \qquad \textbf{Eq. 2.12.}$$

The energy density can be calculated for the electrodes or even for the full battery system (anode and cathode material, separator, electrolyte, sealing, and wiring). Often, different battery types are compared by either their volumetric or gravimetric energy density.

Another important parameter to evaluate a cell is the Coulombic Efficiency (CE) which represents the ratio between the output (Q_d) and input (Q_c) of charge (Eq. 2.13). The CE is relevant to measure irreversible capacities and the CE of a single cycle is related to the capacity fading.

$$\mathrm{CE} = \frac{Q_\mathrm{d}}{Q_\mathrm{c}} \qquad \textbf{Eq. 2.13.}$$

2.4. All-solid-state lithium batteries

LIBs are the preferred battery type to power portable consumer electronics for entertainment, computing, and telecommunication as they offer high energy density and a longer lifetime than other battery types [1-4]. The LIBs have been optimized for these applications. However, the upcoming electric mobility and the Internet of Things (IoT) have different requirements such as large-scale LIBs or an extended operational temperature window. In large scale LIBs, the large amount of flammable liquid electrolyte leads to safety concerns. IoT devices require miniaturized LIBs that have good low (below 0 °C) and high temperature (above 40 °C) performance as these devices are exposed to a wide range of temperatures. Additionally, for all applications of LIBs, a higher energy and power density, and increased shelf and cycle life are desirable. However, physicochemical restrictions limit the increase in energy and power density of LIBs [68].

In this regard, All-Solid-State Lithium Batteries (ASSLB) have attracted the attention of researchers and engineers as they offer high intrinsic safety, extended operational temperature, and potential to achieve higher energy and power densities with longer shelf and cycle life [69]. The higher energy density is a result of the easier stacking that leads to a simplified thermal management system of the battery [70].

An ASSLB can contain the same CAM (section 2.4.2) as that for LIBs but uses obviously a solid electrolyte (section 2.4.3) and different anode material (section 2.4.1).

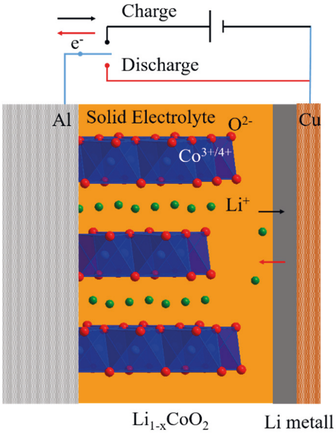

Fig. 2.9. Possible cell design of an all solid-state Li battery with a metallic Li anode and the processes during charge and discharge. The current collector are Al on the cathode side and Cu on the anode side. Different current collector materials are required to prevent their reduction or oxidation during cycling [65].

2.4.1. Anode materials

Metallic Li foils would be the optimal anode material for Li batteries [71].[1] Metallic Li can provide good electronic conductivity, high specific storage capacity of 3860 mAh g^{-1}, and a low negative electrochemical potential of -3.04 V vs the standard hydrogen electrode. It is also lightweight due to its low density of only 0.59 g cm^{-3}.

Metallic Li anodes are common for primary batteries (such as commercial Li-air batteries)[2] but uncommon in rechargeable batteries. This is due to two limitations [72]: The first one is the uncontrollable growth of Li dendrites during charging and the second one is the low coulombic efficiency due to the decomposition of liquid electrolyte when in contact with metallic Li to form a Solid Electrolyte Interface (SEI). While the loss of Li by forming the SEI can be overcome by the usage of excess Li, the Li dendrites lead to safety hazards and short cycle life.

As a work around, batteries have been designed as Li-ion batteries. For conventional Li-ion batteries the anode is graphite-based [72]. The graphite is chosen as it can provide high specific capacity and low electrochemical potential. The Li intercalation process is reversible, and the performance of the anode can be maintained for up to several thousand cycles. The advantages in safety and cycle life outweigh the disadvantages of lower specific capacity and higher electrochemical potential than metallic Li.

Next generation Li batteries are designed to prevent the Li dendrite formation and allow the use of metallic Li anodes [2]. The Li dendrite prevention is achievable by improved stability and uniformity of the SEI layer [73]. However, this approach can only guarantee limited success as metallic Li is believed to be thermodynamically unstable in organic solvents used in commercial liquid electrolytes [72]. One proposed alternative is the usage of mechanical blocking layer by solid electrolyte with a high shear modulus [73, 74]. Nevertheless, Li dendrite growth has been observed in ASSLBs with such solid electrolytes [10]. As the solid electrolyte acts just as a mechanical barrier to prevent Li dendrite growth, it does not change its root causes. The relatively slow Li atomic diffusion in metallic Li anodes still lead to the formation of Li dendrites [10].

Higher Li atomic diffusion in the anode can prevent Li dendrite formation. This is achieved with a variety of Li alloys [75]. One popular system is the In-Li alloy. The In-Li alloy is formed during charging of the Li batteries [74]. The In-Li alloy has a high Li diffusion coefficient that

---

[1] A battery with metallic Li is called Li battery, the Li-ion battery (LIB) describes a battery with only Li-ions, metallic Li is not found.

[2] Research is focusing on rechargeable Li-air batteries [61].

is beneficial to prevent Li dendrite formation [74]. High operation temperatures increase the Li atomic diffusion process further. Indium also has a high theoretical capacity for Li of 1012 mAh g^{-1} and can prevent undesired side reactions between anode and electrolyte [76, 77]. The In-Li alloy has a stable redox potential of about 0.6 V vs Li/Li^+ over a wide stoichiometry range [78].

Another promising anode material are Si-based anode materials [79, 80]. Si-based anode materials have the potential of significantly enhancing the gravimetric capacity (up to 4200 mAh g^{-1}) compared to the graphite-based anodes (372 mAh g^{-1}) [79, 80]. The Si-based anode materials have even higher capacity than metallic Li anodes (3860 mAh g^{-1} [71]). However, the volume change of Si-based anodes during de-/lithiation causes rapid capacity fading and prevents their commercial application [79, 80].

Recently, researchers try to completely eliminate the anode materials in an anode-free concept [81, 82]. In such a concept the Li-ions are simply plated onto the current collector, which will form the anode during the first charge. Anode-free Li batteries are advantageous as during the processing no metallic Li is present, which lowers the requirements concerning the atmosphere of the manufacturing process and eliminates any steps necessary to attach an anode to the cathodic half-cell [82]. While the manufacturing process is simplified, an anode-free cell faces the challenge of rather large volume changes during the first formation of the anode and cycling. This can lead to rapid fading of the electrochemical properties e.g. conductivity and capacity [82].

2.4.2. Cathode active materials

The intrinsic requirements for Cathode Active Materials (CAMs) are a high potential vs Li/Li^+ and a high specific Li-ion capacity (see also Fig. 2.6) [63]. De-/lithiation has to be a reversible process for rechargeable Li batteries.

The most commercially successful CAM is $LiCoO_2$ (LCO). LCO is a layered Li transition metal oxide. Multiple LCO phases are thermodynamically stable [83]. Among them, the rhombohedral phase, with the space group $R3m$ is the most relevant one. In the $R\overline{3}m$ LCO, the CoO_6 and LiO_6 octahedra are occupying octahedral sites in alternating LiO_2 and CoO_2 layers. The CoO_2 layers in LCO can be stacked in three different possibilities to describe the unit cell. These are classified as O3, O4, and O2-type (Fig. 2.10) [84].

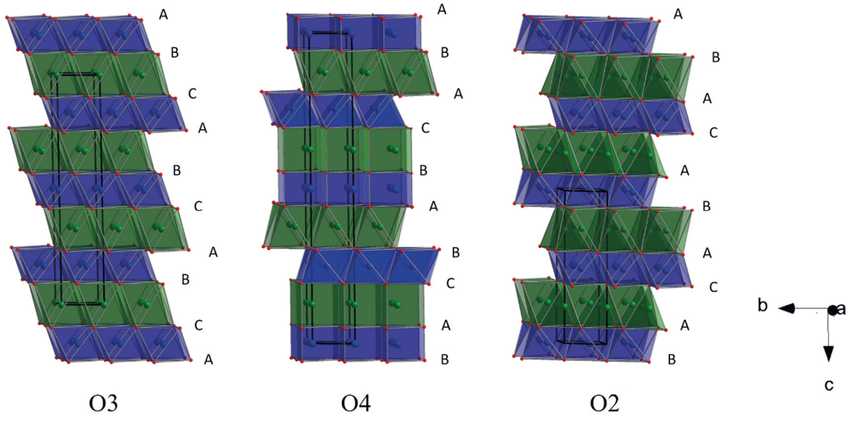

Fig. 2.10. LCO has three relevant polymorphs by different staking of the LiO_6- and CoO_6-octahedra in AB, BC, and CA layers (red: oxygen-, blue: Co-, and green: Li-ions) [84].

The electrochemical behavior of the three LCO polymorphs as CAM is distinct. De-/lithiation in the polymorphs occurs at different voltages, leading to specific charge and discharge profiles for each polymorph [84]. This also affects, the capacity and reversibility of the de-/lithiation, which is highest for O3 and O4. The O2-type has lower stability as the removal of Li-ions leads to gliding of the CoO_2 layer and irreversible phase transitions [84].

The rhombohedral LCO has higher electronic and ionic conductivity in comparison with other LCO phases and can explain its superiority for the application as CAM. Therefore, the theoretical specific capacity of 274 mAh g^{-1} and theoretical volumetric capacity of 1363 mAh cm^{-3} is also highest among LCO phases [63]. However, the practical capacity of LCO is only half of its theoretical one, as the Li-ions are essential for the stability of the LCO structure. The charge of the Li-ions counteracts the repulsive forces between the CoO_2 layers and keeps the CoO_2 layer together. During delithiation the repulsive forces between the CoO_2 layers get stronger as the counteracting Li-ions are removed and the distance between the CoO_2 layers expands. As soon as more than half of the Li-ions are removed from the structure, irreversible changes occur in the LCO structure [64]. This can be avoided by only charging the $Li_{1-x}CoO_2$ to maximum a half ($x \leq 0.5$) of the Li-ion concentration within LCO.

LCO is a classical two-dimensional conductor. The Li-ions can diffuse within the LiO_2 layers but not cross the CoO_2 layers (Fig. 2.11). Depending on the orientation of LCO and the long-range order, the LCO can only be charged/discharged in isolated locations [85, 86].

This means that the LCO can partially be overcharged even as the overall SoC of LCO is not overcharged. Hence, a change in the crystal structure, accompanied by oxygen loss can be observed from the electrolyte interface [83].

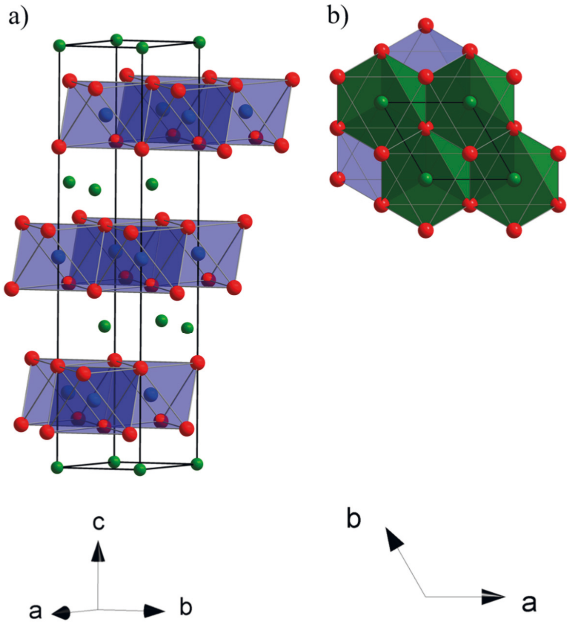

Fig. 2.11. Schematic drawing of the unit cell of LCO. a) The Li-ion migration is possible in *a*- and *b*-direction or within the LiO_2 layers. b) In *c*-direction or through the CoO_2 layers the Li-ion migration is not possible [86]. The color code is: Li: green, Co: blue, and O: red.

By charging the $Li_{1-x}CoO_2$ only to $x \leq 0.5$, a stable cycle performance is obtained. LIBs or Li batteries can be designed to successfully last for their application in most portable electronic devices. However, LCO is also a controversial material due to its release of oxygen at temperatures above 200 °C that can cause explosions and environmental concerns [63]. Additionally, battery manufacturers look for abundant and cheaper alternatives than expensive Co-based materials [5].

Substitution of Co with Ni was found to be an effective way of increasing the specific capacity and lowering the cost. Adding a small amount of Al or Mg helps to improve the thermal stability [63]. Some $LiNi_xCo_yAl_zO_2$ (NCA) and $LiNi_xCo_yMn_zO_2$ (NMC) combinations achieve reversible specific capacity as high as 200 mAh g^{-1} or 234 mAh g^{-1} with good cycle stability.

Research efforts on complete Co-free CAM are ongoing [87, 88]. Co-free CAM such as $Li_2Ni_{1-x}Mn_yO_2$ (NMO), is attractive as it can provide similar energy density as LCO (NMO: 180 mAh g^{-1}) at lower cost due to cheaper transition metals [89]. NMO is so far only used in research, as its commercialization is pending due to its high operational voltage of 4.7 V vs Li/Li^+, for which most of the commercial electrolytes face severe decomposition [63]. Besides layered CAMs also spinel-, olivine-, and tavorite-structures are relevant [63]. An overview of commercialized CAMs, as well as promising CAMs in research is shown in Tab. 2.2.

Tab. 2.2. Properties of representative intercalation cathode compounds [63, 64, 90-92].

Structure	**Compound**	**Specific capacity (theoretical/practical) (mAh g^{-1})**	**Current status**
Layered	$LiTiS_2$	225/210	Commercialized
	$LiCoO_2$	274/148	Commercialized
	$LiNiO_2$	275/150	Research
	$LiMnO_2$	285/140	Research
	$LiNi_{0.33}Mn_{0.33}Co_{0.33}$	280/160	Commercialized
	$LiNi_{0.8}Co_{0.15}Al_{0.05}O_2$	279/199	Commercialized
	$LiNi_{0.5}Mn_{0.5}O_2$	280/180	Research
	Li_2MnO_3	458/180	Research
Spinel	$LiMn_2O_4$	148/120	Commercialized
	$LiCo_2O_4$	142/84	Research
Olivine	$LiFePO_4$	170/165	Commercialized
	$LiMnPO_4$	171/168	Research
	$LiCoPO_4$	167/125	Research
Tavorite	$LiFeSO_4F$	151/120	Research
	$LiVPO_4F$	156/129	Research

Another type of CAMs are conversion type materials [93]. In conversion type cathodes the Li-ions react with the CAM. The reactions within a conversion type CAM are shown in Eq. 2.14 with a transition metal (TM, i.e. Fe^{3+}, Fe^{2+}, Ni^{2+}, Cu^{2+},…) and the anionic species (X, i.e. halogen ions or chalcogenide ions) [63, 94].

$$TM_aX_b + (b\cdot c)\cdot Li^+ + (b\cdot c)\cdot e^- \rightleftharpoons a\cdot TM^0 + b\cdot Li_cX \qquad \textbf{Eq. 2.14.}$$

Suitable transition metal compounds are transition metal oxides, sulfides, fluorides, phosphides, and nitrides [93]. The advantage of the conversion type CAM is its high theoretical-capacity around 500 to 1500 mAh g^{-1} [93]. However, conversion type CAM are still in the research stage as the volume changes during the reaction with Li are challenging to control and lead to rapid capacity fading in first experimental cells.

In comparison to the anode materials (see section 2.4.1), the specific capacity of the currently commercialized CAMs is low (Tab. 2.2). In order to obtain batteries with high energy density, the CAM is coated as a thin layer on a porous nanostructured electronic conductor, such as carbon-based structures, to achieve a large CAM/electrolyte interface area [64]. The nanostructured CAM surface can be beneficial for i) enhancing the reversibility of Li-ion insertion and extraction without damage to the crystal structure and ii) reduction of electronic and ionic pathways [64].

As shown in Fig. 2.12a, the typical discharge plateau for LCO is only observed in the bulk state. The plateau is formed during discharge of the bulk LCO. As soon as the bulk is discharged and only the surface is discharging the potential decreases due to different energy levels of the surface sites (Fig. 2.12b). Due to the high surface area of nanomaterials, only surface discharge is observed.

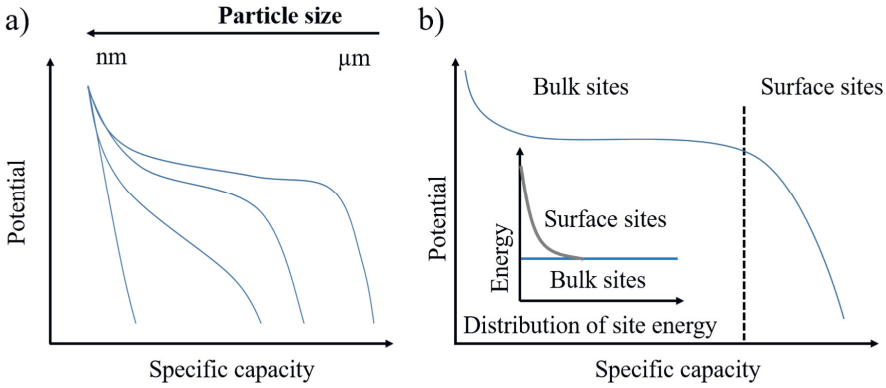

Fig. 2.12. Discharge profiles of LCO according to particle size (a). The discharge profile is defined by bulk and surface sites and their individual energy [64].

2.4.3. Electrolytes

Electrolytes can be liquid or solid. In most commercial LIBs liquid-based electrolytes are used. Liquid electrolytes are relatively cheap (in comparison to other electrolytes i.e. polymers or ceramics) [95], rather easy to handle in dry atmosphere, and established. In next-generation LIBs or Li batteries higher cycle stability and energy density, and safety concerns have to be addressed. In this regard, ASSLBs on the basis of solid electrolytes attract attention of researchers and engineers [1, 3, 96]. Solid electrolytes can be sorted in different classes such as: oxides, sulfides, hydrides, halides, and polymers [96].

A key property of solid electrolytes is their ionic conductivity [96]. However, for device integration other properties are also relevant. The most relevant ones are high ionic conductivity, low ionic area-specific resistance, high electronic and ionic (besides for the desired ions) Area-Specific Resistance (ASR), high ionic selectivity, a wide electrochemical stability window, good chemical compatibility with other components, excellent thermal stability and mechanical properties, simple fabrication processes, low cost, easy device integration, and environmental friendliness [96]. Therefore, each electrolyte class has its unique advantages (Fig. 2.13).

The focus of this work will be on oxide-type solid electrolytes. Oxide-type solid electrolytes are promising as they have beneficial intrinsic properties such as a high thermal and oxidation stability, and good ion selectivity [14, 29]. However, the device integration and the processing cost have to be optimized [4, 96, 97].

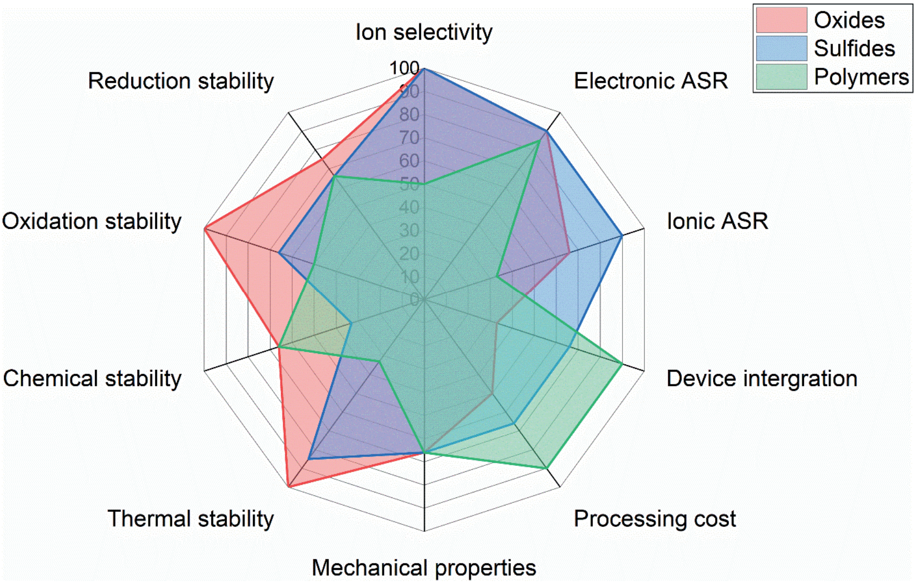

Fig. 2.13. Relevant solid electrolyte properties for oxide-, sulfide-, and polymer-based electrolytes [4, 96, 97]. In comparison to the sulfide and polymer electrolytes, the strength of the oxides is in its oxidation and thermal stability.

One of the most promising oxide-type solid electrolytes is the Li-stuffed garnet-type $Li_7La_3Zr_2O_{12}$ (LLZ) ceramic [13, 14, 29]. LLZ can crystallize in cubic or tetragonal phase. Both phases have a high Li-ion transference number (t_{Li+}≈1) and good chemical stability versus metallic Li. However, the ionic conductivity of the tetragonal phase is two orders of magnitude lower than that of the cubic phased one, due to different positions of Li-ions within the LLZ structure [7-13]. The cubic phase of LLZ crystallizes in the space group $Ia\bar{3}d$ with a lattice constant *a* of 12.95 – 12.97 Å (Fig. 2.14a). The framework of the garnet structure is an 8-fold coordinated LaO_8 dodecahedra (*24c*) and 6-fold coordinated ZrO_6 octahedra (*16a*) [14, 29]. The interstices of the framework structure are partially occupied by Li atoms. The occupied sites are the tetrahedral *24d* sites and the octahedral *48g* or off centered *96h* sites. The *96h* sites are displaced off the *48g* sites due to Li^+-Li^+ repulsion across shared site face. The *24d* tetrahedral cages form a three-dimensional network of conduction pathways. The Li^+ in *24d* sites are considered immobile. The Li^+ diffusion is a result of either the Li^+ migration via interstices of neighboring octahedral sites and bypasses the Li^+ in tetrahedral sites or the Li^+ movement through the shared triangular faces of the octahedral and tetrahedral faces (Fig. 2.14b) [29].

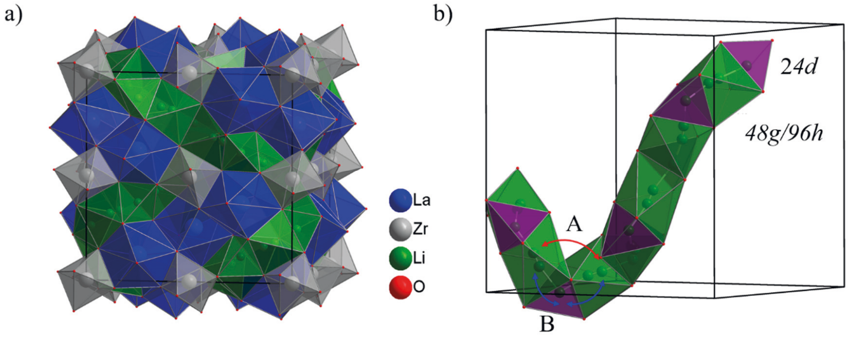

Fig. 2.14. Crystal structure of cubic LLZ in a) and the Wyckoff positions for the Li-ions in *24d*, *48g*, and *96h* sites. b) The Li-ion conduction via the tetrahedral sites are marked A and through triangular faces are marked B [29].

The activation energies for the Li^+ diffusion is 0.8 eV via interstices or 0.26 eV via octahedral and tetrahedral faces, which means the later one is the preferred Li^+ diffusion pathway. The energies, however, also depend on the Li concentration in the LLZ structure. In the case of a Li count smaller than five for the formula unit, the interstitial conduction might be preferable [98].

The Li^+ conduction via the interstices is hindered in the tetragonal LLZ phase by distortion that leads to the Li^+ occupying different sites (*8a*, *16f,* and *32g*), than in the cubic one (*24d*, and *48g* or *96h*) [29]. The tetragonal phase of LLZ is the one stable between RT and 150 °C [99, 100], which is the temperature range for battery operations [101-103]. The desired high

Li^+ conductive cubic structure of LLZ is only stable at high temperature. One possibility to stabilize the cubic LLZ structure at RT is by a partial substitution of Li and Zr in LLZ by Al and/or Ta (e.g. $Li_{6.45}Al_{0.05}La_3Zr_{1.6}Ta_{0.4}O_{12}$, LLZ:Ta) [104-107]. This results in an excellent ionic conductivity of $>10^{-4}$ $S{\cdot}cm^{-1}$ at RT and low electronic conductivity of around 10^{-8} S cm^{-1} to 10^{-7} S cm^{-1} [29]. The ionic conductivity is furthermore dependent on the surface properties of the LLZ that can be, for example, altered by the atmosphere its exposed to.

Although LLZ can be handled in ambient air, prolonged exposure leads to the formation of an insulating layer of LiOH and Li_2CO_3 at the surface due to Li^+/H^+ exchange [108, 109]. However, this insulating layer is usually removed during the following heat treatment (e.g. sintering) with restoration of the initial ionic conductivity [108].

The required high sintering temperature hampers the integration of LLZ into ASSLB. The high LLZ sintering temperature leads to chemical reaction with CAMs or severe diffusion of transition metals, which causes electronic leakage through the electrolyte [27, 110, 111].

One solution so far is that LLZ is sintered first and then coated with CAM [27, 112]. The CAM/LLZ interface area is, therefore, small and the ASSLB has a low energy density [113]. Furthermore, the low Li-ionic conductivity of most CAM limits the thickness of the cathode. Of course, it is possible to mix the CAM with liquid or polymer electrolyte and attach it to a solid electrolyte/separator [114, 115]. This would lead to thicker cathodes and higher energy density by introducing Li-ion diffusion paths into the cathode for accessing CAM. The system would, however, also contain multiple electrolytes, as well as solid-liquid electrolyte interfaces, and different CAM/solid electrolyte and CAM/liquid electrolyte interfaces. Therefore, the design can be considered a hybrid ASSLB which requires its own optimization to obtain desirable electrochemical properties. The other option is to lower the sintering temperature of LLZ and enable the co-sintering of LLZ and CAM (see section 2.2.3).

The chemical reactions between two materials are, in general, kinetically controlled by the thermal cycle. Faster processing (high heating and cooling rate and shorter dwell time) in combination with decreased sintering temperature is an alternative option to reduce the secondary phase formation [18, 22, 53]. Reduced sintering temperatures can be obtained by using sintering additives e.g. Nb- or Li_3BO_3 layers [22, 27, 116]. However, the additive coating itself,usually has a much lower ionic conductivity than that for the sintered LLZ, which can be a limiting factor for the final battery performance. For example, Li_3BO_3 has an Li-ion conductivity of only 10^{-6} S cm^{-1} at RT which is much lower than that of LLZ (approximately 10^{-4} S cm^{-1} at RT) [30]. Advanced sintering technique e.g. FAST/SPS could circumvent the use of sintering additives due to the application of mechanical pressure and Joule heating which enables the sintering to occur at lower temperatures with significantly shorter dwell times as compared with conventional free sintering [28, 31, 33, 34, 36-38].

2.4.4. Evaluation of the performance of garnet-based ASSLBs

The progress achieved by several groups allows the preparation of garnet-based all-solid-state cathodes with a high CAM loading, high initial capacity, and high capacity utilization [18, 22, 23, 53, 117, 118]. However, the problem of fast capacity fading during electrochemical cycling that is observed in nearly all published ceramic cathodes, still limits their application. For example, Tsai et al. reported the loss of most of the initial capacity (1.8 mAh cm^{-2} to 0.4 mAh cm^{-2}) just after 100 cycles at currents of 50 µA cm^{-2} for a garnet-based ASSLB with a composite LCO/LLZ cathode [18]. Only Ohta et al. have been able to cycle a garnet-based thin layer LCO cathode successfully for 100 times without observing significant capacity loss [119]. However, the stable electrochemical performance was achieved for low currents of 10 µA cm^{-2} [120]. For any possible application, this current is too small. Several phenomena were suggested as possible reasons for the fading of the performance (Fig. 2.15) [1, 3, 8, 11, 121-125].

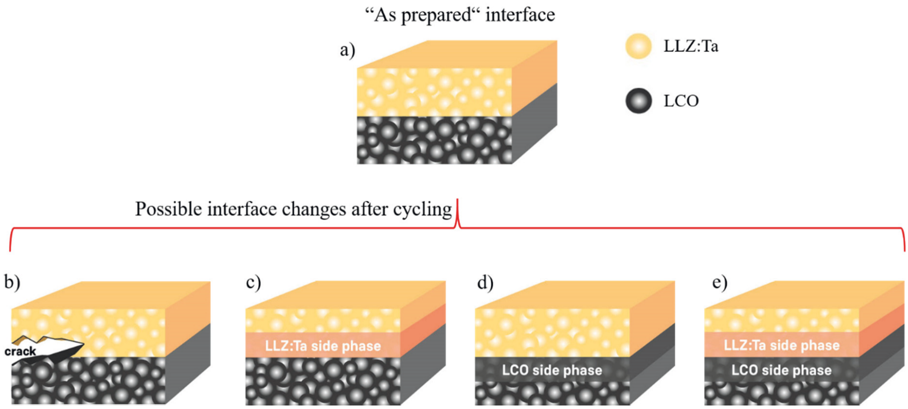

Fig. 2.15. Simplified schematic drawing of the prepared LCO/LLZ:Ta interface (possible secondary side phases are not shown) (a). In b) to e) the possible reasons for the increasing LCO/LLZ:Ta interfacial impedance are shown. This can be due to the (b) mechanical degradation of the electrode due to the bias-induced volume changes, or the electrochemical degradation of(c) LLZ:Ta; (d) LCO or (e) both phases during operation with formation of respective high-impedance products.

Besides processing-induced degradation, during the high temperature processing, leading to the formation of high impedance reaction layers [1, 3], mechanical fracturing of the cathodes due to the change in CAM volume during de-/lithiation is one of the most favored explanations for the low electrochemical performance of all-solid-state cathodes (Fig. 2.15b). In LCO, the volume change reaches up to 4 vol-% during de-/lithiation without any geometrical constraint, and can break the rigid LCO/LLZ:Ta interface [62]. Besides, the LCO and LLZ have different crystal structures. Ideally LCO is crystallized in rhombohedral crystal structure with lattice parameters of *a*: 2.87 Å and *c*: 14.05 Å [126]. LLZ, however, should have a cubic crystal structure with *a*: 12.95 Å – 12.97 Å [29]. The sintered LCO/LLZ interface, therefore, experiences stress, which is possible to be released by fracturing of the LCO/LLZ interface [127, 128]. Another hypothesis for the low cycling stability of the rigid ceramic cathodes is electrochemical degradation of either the solid electrolyte, CAM, or both during operation (Fig. 2.15c-e). While LLZ is estimated to be stable up to 6 V vs Li/Li^+, recent theoretical work has suggested the oxidation of LLZ already starts at 2.9 V vs Li/Li^+ [122]. The experimental validation still has to be provided [122, 129, 130]. Possibly, the LLZ is kinetically stabilized by a high oxidation overpotential or by a thin passivating layer formed on the LLZ surface, that prevents ongoing decomposition [122].

Besides LLZ, LCO could also show electrochemical degradation and be responsible for the fading electrochemical performance (Fig. 2.15d). Wang et al. observed a thin (below 250 nm) layer of “disordered” LCO formed on the interface with LiPON electrolyte [124, 131]. Disordered LCO accompanied by a possible phase transformation can lead to a significant decrease in ionic and electronic conductivity, and specific capacity [86, 126]. LCO in its rhombohedral crystal structure has a practical specific capacity of 140 mAh g^{-1}[126], while other LCO structures have less. The “quasi-spinel” structure for example has only a practical specific capacity of 84 mAh g^{-1}. The phase change in LCO would hence cause a significant loss in capacity. Moreover, Otoyama et al. published that the State of Charge (SoC) of LCO in a composite cathode can be inhomogeneous [132]. An inhomogeneous SoC leads to inhomogeneous expansion/contraction of LCO and as a result to disordering or even cracking.

3. Materials and Methods

3.1. Synthesis of the solid electrolyte

Ta- and Al-substituted LLZ powder (theoretical stoichiometry: $Li_{6.45}Al_{0.05}La_3Zr_{1.6}Ta_{0.4}O_{12}$, further denoted as LLZ:Ta) was synthesized by solid-state reaction [133]. The starting materials, $LiOH \cdot H_2O$ (99.995 %, Sigma Aldrich; 12 wt-% or 20 wt-% excess was added to compensate the Li loss during processing [133]), La_2O_3 (99.9 %, Merck), ZrO_2 (99.5 %, Treibacher), Ta_2O_5 (99.5 %, Inframat Corp.) and Al_2O_3 (99.9 %, Inframat Corp.), were mixed stoichiometrically. The resulting powder was pressed into pellets and calcinated at 850 °C in an Al_2O_3-crucible with an Al_2O_3 cover for 10 h (with a heating and cooling rate of 5 K/min) and crushed in a mechanical mortar RM200 (Retsch) for 1 h. This procedure was repeated twice with a calcination temperature of 1000 °C. The resulting particles had a spongy shape (Fig. 3.1a) with a particle size of $D_{10} = 5.8$ µm, $D_{50} = 10.0$ µm and $D_{90} = 16.4$ µm as determined by the laser light scattering method (method described in section 3.3.1). This powder will be denoted further as LLZ:Ta-air powder. The real composition of the LLZ:Ta powder was analyzed by Inductive Coupled Plasma-Optical Emission Spectroscopy (ICP-OES, Tab. 3.1, method described in section 3.3.2).

Tab. 3.1. Composition of the prepared LLZ:Ta powder after calcination by ICP-OES.

Element	**Theoretic stoichiometry**	**12 % Li excess**	**20 % Li excess**
Li	6.45	7.07	7.39
Al	0.05	0.05	0.07
La	3.00	3.00	3.00
Zr	1.60	1.59	1.58
Ta	0.40	0.40	0.41

A part of the LLZ:Ta powder was ball-milled (200 rpm, 3 h in isopropanol, Retsch) after calcination, dried and sieved (20 µm) to analyze the effect of grain size on the FAST/SPS process.

3.1.1. Pretreatment of the solid electrolyte

A part of the LLZ:Ta powder with 20 % Li excess was pressed into loose pellets. The LLZ:Ta pellets were transferred into an Ar-filled glovebox. The LLZ:Ta pellets were placed in an Al_2O_3

crucible and annealed in Ar at 750 °C for 2 h to remove surface impurities (LiOH and Li_2CO_3). The annealed cake was crushed into powder in the Ar-filled glovebox. The obtained powder consisted of particles with nearly the same shape (Fig. 3.1b) and particle size as the non-annealed powder with $D_{10} = 6.6$ µm, $D_{50} = 12.2$ µm and $D_{90} = 22.5$ µm. This powder is abbreviated further as LLZ:Ta. The heat treatment led to a small loss of Li according to ICP-OES results (Li: 7.18; Al: 0.05; La: 3.00; Zr: 1.61; Ta: 0.41, compare with Tab. 3.1).

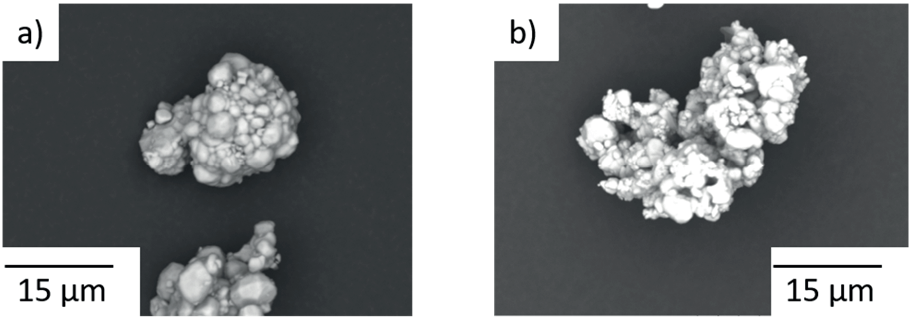

Fig. 3.1. a) Pristine LLZ:Ta powder. b) LLZ:Ta powder after 2 h annealing in Ar at 750 °C.

3.2. Pellet preparation

The pellets with one or two layers (for the use as a half-cell) were manufactured by FAST/SPS or free sintering. In one case, LLZ:Ta-air, LLZ:Ta powder, or their 50/50, 40/60, or 60/40 wt-% mixture with LCO (99.95 %, Alfa Aesar) was used. In the other case, the first layer consisted of LLZ:Ta-air, or LLZ:Ta and LCO mixture, or pure LCO and the second layer was comprised of pure LLZ:Ta-air or LLZ:Ta powder. A schematic overview of the prepared pellets is shown in Fig. 3.2.

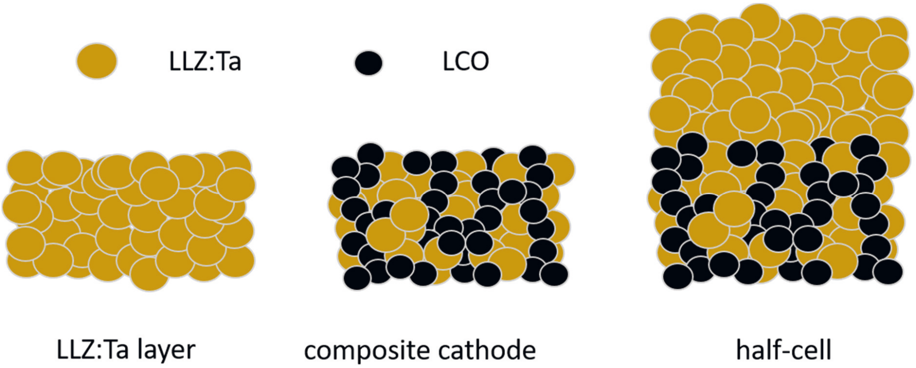

Fig. 3.2. Schematic overview of manufactured battery components.

3.2.1. FAST/SPS sintering

For FAST/SPS sintering, LCO, LLZ:Ta-air, LLZ:Ta powder or their mixture was used. In the case of co-sintering of half-cells, the first layer consisted of LLZ:Ta and LCO mixture and the second layer was comprised of pure LLZ:Ta-air or LLZ:Ta powder.

During manufacturing of pellets with single layer, a portion of 0.5 g of LCO, LLZ-air, LLZ:Ta powder, or their mixture with LCO was poured into a metallic mold made of a molybdenum-based alloy (TZM, Plansee SE, Fig. 3.3a). The mold had an inner diameter of 12 mm that was covered by wounded graphite foil (SGL Carbon). The TZM punches were also separated from the powder by two discs punched from the same graphite foil to prevent sticking with the sintered pellet.

For the half-cell, 0.5 g of powder mixture was firstly poured in the mold and pressed by hand, followed by adding another 1 g of LLZ:Ta-air or LLZ:Ta powder and pressing by hand.

The powders and powder mixtures were sintered in a HP D 5 FAST/SPS device (FCT Systeme GmbH). The sintering was performed at a temperature of 675 °C, and between 750 °C to 1050 °C in 50 K steps with 10 min dwell time in Ar flow (Fig. 3.3b). The heating rate was 100 K min^{-1} and the cooling rate was 20 K min^{-1}.

A sintering temperature of 675°C is slightly below an onset temperature of reaction between LCO, LLZ, and graphite foil (starting at approximately 700 °C) as explained in detail by Laptev et al. [17]. A temperature of 750°C is somewhat higher than the above-mentioned onset temperature. However, the reaction between LCO, LLZ, and graphite at this temperature is still not pronounced [17]. The sintering at 800 °C was performed to verify the phase stability at higher temperature. The single phases of LCO and LLZ:Ta-air and LLZ:Ta were sintered over the whole temperature range of 675 °C to 1050 °C.

A mechanical pressure between 50 MPa and 440 MPa was applied before or after heating, and during the dwell process in all experiment. The loading with 50 MPa is typical for FAST/SPS sintering in a standard graphite mold [32]. A pressure of 440 MPa is the highest pressure which can be achieved in the used 12 mm mold with a maximal load of 50 kN for a HP D 5 device. After FAST/SPS sintering the graphite foil was polished off from all pellet surfaces by SiC sandpaper (grade #4000).

3.2.2. Conventional sintering and annealing of the prepared pellets by FAST/SPS

LLZ:Ta pellets were also prepared by conventional free sintering. The LLZ:Ta-air powder was pressed into 12 mm in diameter pellets and sintered at 1175 °C for 10 h in a closed Al_2O_3 crucible in air. The temperature was increased with 5 K min^{-1} and after sintering the samples were free cooled to RT. Some of the free sintered LLZ:Ta-air pellets were used to assemble half-cells. These LLZ:Ta-air pellets were polished with SiC sandpaper (up to grade #4000). The polished LLZ:Ta-air were painted with an ink of LCO and LLZ:Ta-air mixture, prepared according to Tsai et al [18], or used in polymer-ceramic ASSLBs (section 3.4.3). The ink was dried at 50 °C and co-sintered according to the schedule in Fig. 3.3c. This process was also applied to FAST/SPS sintered samples for their annealing.

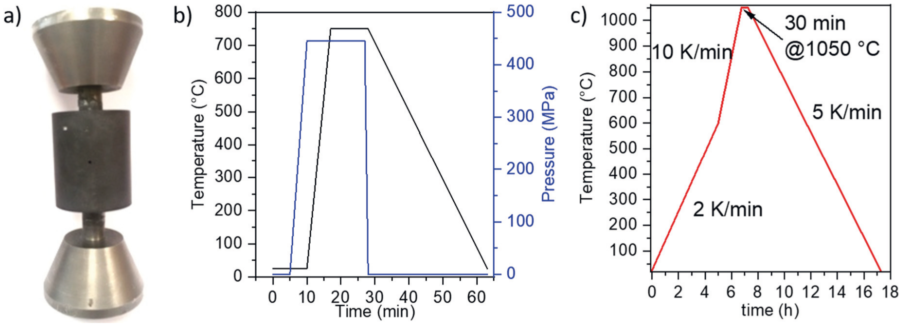

Fig. 3.3. a) Photograph of the FAST/SPS mold. b) Schematic of the FAST/SPS sintering process with 750 °C sintering temperature. c) The sintering schedule for the LCO/LLZ:Ta-air ink and annealing of the FAST/SPS samples.

3.3. Characterization

3.3.1. Particle size distribution

Particle Size Distribution (PSD) of LLZ:Ta powder was measured by the laser light scattering method in a LA950 device (Horiba) in an ethanol suspension. The laser light is scattered by the particles in the ethanol suspension. The diffraction angle is dependent on the particle size, which allows to separate grain sizes in the micro- to millimeter range [136]. Smaller particles have high scattering angles and large grains have low ones. However, the light intensity of the scattered light is dependent on the grain size and larger particles cause much higher scattered light intensity. By this a small number of large particles can hide a high number of small particles.

The measured light intensity is converted into particle sizes by the Mie theory based on the Fresnel equation or Fraunhofer approximation [136]. While the Fresnel equation is used for near field regions, the Fraunhofer approximation is applied for the far field. Far field means that diffraction pattern and the diffracting particles are far away from each other.

In this work, the Fraunhofer approximation is used to calculate the PSD. To correct for the different light distribution in the suspension in comparison to the ethanol solvent, the refractive index of 1.85 was used.

In sintered bodies the grain sizes were measured by the linear intercept method from SEM images [137]. In this method, a cross sectional SEM (described in section 3.3.6) image taken in the backscattering mode is used. A random straight line is drawn through the SEM image and then the number of grain boundaries intersecting the line is counted. By dividing the length of the line through the number of intersecting grain boundaries, the average grain size can be calculated.

3.3.2. Chemical analysis

The stoichiometry of synthesized and commercial powders was measured with Inductively Coupled Plasma Optical Emission Spectroscopy (ICP-OES) with a Thermo Scientific iCAP 7600 dual-view spectrometer. For the measurement 50 mg of the sample was dissolved with the help of 2 g $(NH_4)_2SO_4$ in H_2SO_4. The solution is then sprayed into an Ar plasma [136]. The Ar plasma produces excited atoms and ions that emit electromagnetic radiation which are characteristic to particular elements. In case the intensity is calibrated, ICP-OES can also be used to quantify the concentration of the atoms and ions.

3.3.3. Thermal analysis

The thermal stability of the CAMs powder and in combination with LLZ:Ta powder was measured with Differential Thermal Analysis (DTA) and Thermal Gravimetric Analysis (TGA) with a NETZSCH STA 4491 in vacuum and Ar atmosphere. A piece of graphite foil was added to all samples prior to the measurement to simulate the conditions in the FAST/SPS setup. The heating and cooling rate were 5 K min^{-1}.

In DTA the energy required to heat the sample is compared to a reference sample. In the case the phase of the sample changes, this will either release or consume energy. These energy changes can be measured and help to find the transition temperature of the analyzed material.

In TGA, the weight of the sample material is measured over a temperature range and gives information about the temperature at which the weight is changed. This can help to identify the decomposition temperature.

The sintering behavior was analyzed with dilatometry measurements (DIL 402C dilatometer, NETZSCH). The powder for dilatometer measurement were pressed into pellets with a diameter of 8 mm and height of 1 mm. The heating and cooling rate were 5 K min^{-1}. The Dilatometer measures the shrinkage of a sample. In ceramics, dilatometer measurements can be used to find the onset temperature of sintering.

3.3.4. X-ray diffraction

Atoms in a crystal have commonly a distance of a few nanometers to each other. The wavelength of X-rays is similar and by that elastically scattered by the atoms, or more precise by their electrons [138]. Although most of the scattered X-rays experience destructive interference, some show constructive interference. The angles at which these X-rays are measured are used to calculate the distance between atoms or planes by Bragg’s law (Eq. 3.1) [138].

$$2d \cdot \sin(\Theta) = n\,\lambda \qquad \textbf{Eq. 3.1.}$$

d is the spacing between atoms/planes, Θ is the incident angle, n is an integer, and λ is the wavelength of the X-rays. The diffraction pattern can, therefore, be used to qualitatively and quantitatively analyze phases.

The qualitative and quantitative phase analysis by X-ray diffraction (XRD) was performed with a D4 Endeavor (Bruker) device on powders or pellets (LLZ containing pellets were polished by sandpaper #4000 prior to the analysis to remove LiOH and Li_2CO_3 formed in air).

A Bragg-Brentano configuration in the 2θ range from 10° to 80° with a step of 0.02° and with Cu K_α radiation was used. The XRD device was equipped with a LYNXEYE energy-dispersive 1D detector (Bruker). The HighScore software (Malvern Panalytical) with the PDF-2 database (International Centre for Diffraction Data, (ICDD)) was used for qualitative phase analysis. The Rietveld analysis for quantification of results was conducted using the TOPAS 4.2 software (Bruker).

3.3.4.1. *In-situ* high temperature X-ray powder diffraction

The *in-situ* High-Temperature XRD (HT-XRD) was performed in air. The patterns were recorded with an Empryean (Malvern Panalytical GmbH) including a HTK1200N heating-chamber (Anton Paar GmbH) with Bragg-Brentano geometry equipped with an x-ray tube with Cu anode, and a Ni filter for the removal of the K_β radiation. The measurements were performed with a step size of 0.026°, a collection time of 150 s and 255 channels at 45 kV and 40 mA over the 2θ angular range between 10° and 90°. For HT-XRD, the CAMs: $LiMn_{1.5}Ni_{0.5}O_4$ (MNO), $LiNi_{0.33}Mn_{0.33}Co_{0.33}O_2$ (NMC) stabilized with Mg (NMC:Mg) and with Mg and Al (NMC:MgAl), or LCO (99.95 %, Alfa Aesar)) [3] and LLZ:Ta powder were mixed in a 1:1 wt-ratio and pressed into pellets of 13 mm in diameter.

The *in-situ* HT-XRD were performed at selected temperatures during heating and cooling. The heating and cooling rate were 5 K min^{-1}. The maximum HT-XRD temperature for the samples is given in Tab. 3.2.

Tab. 3.2. Maximum HT-XRD temperatures of the CAM and LLZ:Ta mixtures.

Sample	**Highest HT-XRD temperature (°C)**
LLZ:Ta	1100
LCO + LLZ:Ta	1100
NMC:Mg + LLZ:Ta	800
NMC:MgAl + LLZ:Ta	800
MNO + LLZ:Ta	800

3.3.5. Density measurement

The density of pellets was determined from their geometry and mass or via the Archimedes method, which uses the weight differences of the pellet before and after immersion in water

---

[3] MNO, NMC:Mg, and NMC:MgAl have been synthesized by Dr. S. Ivanov, TU Ilmenau.

and in water [139]. For the Archimedes method the weight of the pellet was measured first. Then the pellet was placed in vacuum and after 2 h the pellet was covered by water for another 2 h. The weight of the sample was then measured in water and outside. The density for LCO/LLZ:Ta pellets was calculated by using a theoretical density of 5.2 g cm^{-3} as an average from LLZ:Ta (5.3 g cm^{-3}) and LCO (5.1 g cm^{-3}) densities [140].

3.3.6. Scanning electron microscopy

The microstructure of powders and sintered pellets was investigated by Scanning Electron Microscopy (SEM) with TM3000 (Hitachi) or Zeiss Ultra 55 microscopes. Within the SEM, an electron beam is focused on the sample to interact with the atoms in the sample. By that different signals (electrons e.g. secondary or back-scattered, x-ray, and cathodoluminescence) are produced [136]. The signals can be used to analyze the microstructure, topography, and composition of the sample.

In this work, the images were recorded in backscattering mode with an electron beam accelerating voltage of 15 kV. The backscattering mode allows to separate heavy and light elements [136], as heavier elements backscatter electrons stronger and appear in the SEM image lighter, This effect allows the separation of LCO and LLZ areas. Often also secondary electrons are used for the SEM image which is beneficial for the analysis of the topography of the sample but is not applicable for polished sample surfaces.

Powder samples were placed on a carbon pad on a sample holder and sputter coated with Au for 10 s. Sintered pellets were embedded in epoxy and polished or used as fracture surface analysis. First SiC sandpaper up to #4000 was used followed by water free diamond suspensions (9 µm, 3 µm, and 1 µm). The surface electronic conduction was increased by sputtering of a thin Pt- (EM ACE200, Leica) or Au-layer (Cressington 108).

3.3.6.1. Energy dispersive X-ray spectroscopy

In combination with SEM analysis, Energy Dispersive X-ray spectroscopy (EDX) measurements were performed. The focused electron beam for SEM imaging generates characteristic x-rays. By detection of the emitted x-rays with EDX, the elements can be qualitatively identified.

The EDX analysis was performed with an X-Max (80 mm^2, Oxford Instruments) in the Zeiss Ultra 55 or a Quantax 70 (Bruker) in the TM3000. The data was analyzed with the Inca or Bruker software package.

3.3.7. Transmission electron microscopy

Transmission Electron Microscopy (TEM) is a technique that creates an image based on the electrons transmitted through a sample [141]. In order to allow the electrons to pass through the sample it is required to be thin, normally less than 100 nm thick. The electrons passing through the sample interact with the atoms and lead to different contrasts in the TEM image as well as different elements and crystallinity can be separated.

In this work, TEM is used to analyze the LCO/LLZ:Ta interface. The high resolution of TEM allows to analyze the LCO/LLZ:Ta interface on an atomic scale and also provides information about the crystallinity and elemental distribution.

The samples for TEM were prepared according to SEM preparation. The lamella for TEM were cut out of a polished cross section by a dual beam-focused ion beam with 30 keV and 10 pA within a Helios NanoLab G3 CX device and transferred to a carbon laced TEM grid by a glass tip micro-manipulator. The TEM images were recorded with a JEM-2100F electron microscope (JEOL) operated at 200 kV.

3.3.7.1. Energy dispersive X-ray spectroscopy

The elemental distribution of chemical species in the samples was performed using EDX with a field emission gun TEM equipped with an electron probe 1.2 nm in size. The data was analyzed with the Inca software package.

3.3.7.2. Selected area electron diffraction

The Selected Area Electron Diffraction (SAED) pattern was done by parallel incident electron beam with a diameter of few microns. The diffracted area of the specimen was selected with the selected-area aperture which is located in the image plane of the objective lens. Thus, the SAED patterns can be collected from LCO and LLZ:Ta part, and the interfaces.

The electron scattering for the SAED patterns is the same principle as for the one by x-rays, (described in section 3.3.4).

3.3.8. Raman spectroscopy

Raman spectroscopy is used to characterize the local chemical order of a sample [136, 142]. Therefore, the phenomenon of inelastic scattering of light by matter is used, also known as Raman Scattering or Raman Effect (Fig. 3.4a), while elastic light scattering is called Rayleigh scattering. The inelastic scattering transfers or receives energy from the sample by the changes in the vibrational or rotational modes of the chemical structure. As a result, the frequency of the scattered light is altered. Either the frequency is increased or decreased which is known as Stokes or anti-Stokes shift. In the case of elastic light scattering (Rayleigh scattering) the frequency remains unchanged.

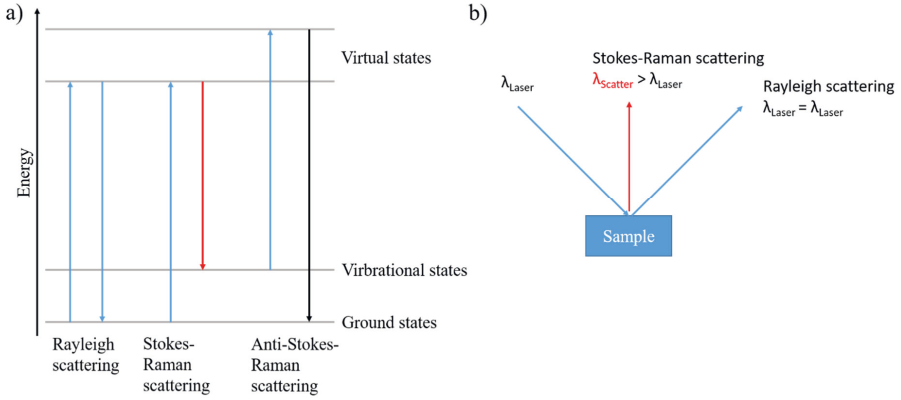

Fig. 3.4. a) Scheme of light scattering [136]. Energy will be transferred to the system and released again. The shift in energy provides information the vibrational modes in the system. b) Example of a setup with a Stokes-Raman and Rayleigh scattering [142].

Raman spectroscopy detects the changes in the vibrational or rotational modes leading to a change in polarization [136]. One main challenge of Raman spectroscopy is the low intensity of the inelastic scattered light. Most light is elastically scattered and has to be separated from the inelastic scattered light (Fig. 3.4b) [142]. Historically, the elastic scattered light was blocked out. Today, photomultipliers are used to intensify the inelastic scattered light signal. Raman spectroscopy is therefore a fingerprint method. Several techniques have been developed to improve Raman spectroscopy [136], like surface-enhanced Raman scattering or tip-enhanced Raman spectroscopy.

The Raman spectroscopy was done with a Renishaw inVia Raman microscope using a solid-state 532 nm excitation laser with a maximum power of 60 mW,[4] 1800 L mm^{-1} or 2400 L mm^{-1} grating and a 50x or 100x objective. Both materials, LCO and LLZ:Ta, decompose during exposure to high laser intensities [143-145]. LCO is less stable and will form Co_3O_4 [143, 144]. In order to preserve the materials, the laser power was reduced. Raman mappings were performed with a laser power of 1 or 5 % and a step size of 0.2 µm. Single scans were performed also at 10 % or for LLZ:Ta, also at 50 %. The spectral acquisition time was chosen with 1 s as it provided good resolution and no material decomposition. For single

---

[4] The laser power reaching the sample is around half of the theoretical value in this device.

scans a total of five scans were performed and averaged. The laser was focused with a point lens. In order to maintain focus during high-resolution Raman mappings, the auto track function (live track function) offered by the WiRE software package was applied. The collected Raman spectra were cleared from cosmic rays and noise filtered with the WiRE software package. The Raman spectra collected in mapping were additionally analyzed with direct classical least squares method by normalization to the mean center and scale to unit variance by the WiRE software package with spectra of pristine LCO or LLZ:Ta.

3.3.9. Time-of-Flight Secondary Ion Mass Spectrometry

Time-of-Flight Secondary Ion Mass Spectrometry (ToF-SIMS) is a destructive and qualitative composition analysis technique, that involves a beam of primary ions focused on the sample surface to produce secondary ions in a sputtering process [146-148]. The analysis of the secondary ions by Time-of-Flight principle can identify the elements. Depending on the mass-to-charge-ratio ($m\ q^{-1}$) of the ionized elements, the duration to hit the detector at the same accelerating voltage is different. The required time can be assigned to a certain mass-to-charge-ratio. As material is removed by sputtering, longer sputter times offer depth profiling (µm-range). The strength of the ToF-SIMS is his high sensitivity and low detection limits, however, the elements cannot be quantified.

A flat polished surface is required to perform ToF-SIMS measurements. Therefore, all ToF-SIMS samples were polished with SiC sandpaper up to #4000 followed by water free diamond suspension (3 µm).

The chemical composition at the surface was studied with a ToF-SIMS (ToF-SIMS V system, ION-TOF GmbH), using a 25 keV Bi^+ primary beam for analysis and a 1 keV O_2^+ sputter beam selected to alter the analysis depth of the measurement. The O_2^+ sputter beam screened over an area of 300 µm by 300 µm. The analyzed area by Bi^+ beam was 120 µm by 120 µm, with positive or negative secondary ions detected. The beams were operated under non-interlaced mode (using a 1s:1s sputter: analyze cycle).

Data analysis was carried out with the SurfaceLab 6.7 (ION-TOF GmbH) software package. In Fig. 3.5, the relevant areas for the ToF-SIMS measurements are schematically shown.

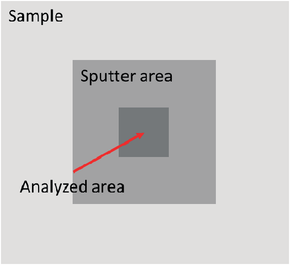

Fig. 3.5. Schematic of the areas relevant for ToF-SIMS measurements. An area of the sample surface was sputtered by O_2^+ to clean the surface and then a part of the sputtered area was analyzed by a Bi^+ beam.

3.4. Electrochemical characterization

3.4.1. Preparation of separator layer for ionic conductivity measurements

The ionic conductivity was measured for LLZ:Ta pellets. The pellets were polished with SiC sandpaper (up to grade #4000) and then sputter coated with Au to act as a current collector on both sides for 150 s. The Au sputter coated LLZ:Ta pellets were placed into spring-compressed (10 N) Swagelok cells and sealed.

3.4.2. Preparation of full cells for battery characterization

Half-cells prepared as described in section 3.2 were used for full cell preparation. The half-cells were polished with SiC sandpaper (up to grade #4000) and then sputter coated with Au (Cressington 108 sputter coater). On the cathode side the sputtering time was 30 s. The Au layer here acts as a current collector. On the LLZ:Ta separator side the Au layer helps the adhesion of an In anode. Afterwards, the half-cells were transferred into an Ar-filled glovebox (<0.1 ppm H_2O and O_2). On the LLZ:Ta-side, a metallic In foil was mechanically pressed on the samples to act as anode. The assembled full cells were placed into Swagelok cells and sealed before taking from the glovebox. The amount of active material in the composite cathodes was estimated by measuring of thickness and diameter of the cathode and by using of average density of the LCO/LLZ:Ta mixture.

3.4.3. Polymer-ceramic full cell fabrication.

A composite cathode was prepared as described in section 3.2.1. However, the graphite foil discs were replaced by mica foil discs to reduce secondary phase formation due to sample contact to the graphite foil [17]. The FAST/SPS parameters were a sintering temperature of 675 °C and an applied mechanical pressure of 50 MPa. The dense LLZ:Ta separator was prepared according to section 3.2.1. Afterwards, the composite cathode and LLZ:Ta layer were annealed as described in section 3.2.2 and polished by SiC sandpaper up to grade #4000.

The prepared composite cathode was sputter coated with Au for 150 s on one side in order to act as a current collector and for the LLZ:Ta separator for 30 s to help the adhesion of the In anode using a Cressington 108 sputter coater. As anode, metallic In foil was mechanically pressed by hand onto the sputter coated LLZ:Ta side. To improve the contact, the cell was heated to 200 °C until In started to melt and was cooled down afterwards. The uncoated sides of the composite cathode and the LLZ:Ta separator were coated with polymer electrolyte. As polymer electrolyte solution of poly[bis(2-(2-MethoxyEthoxy)Ethoxy)Phosphazene] (MEEP) monomer and $LiB[C_2O_4]_2$ as conduction salt in acetonitrile was chosen (the synthesis procedure can be found in [134, 135]). The MEEP monomer was dried for 60 min at 80 °C and polymerized under UV light in a UV cube 100 (Hönle Group) for 30 min. Afterwards the composite cathode and the LLZ:Ta separator were attached together. The polymer-ceramic ASSLBs were placed spring-compressed (10 N) Swagelok cells and sealed. All cells had a diameter of 12 mm and a thickness of around 0.5 mm. A schematic of the prepared polymer-ceramic ASSLB is shown in Fig. 3.6.

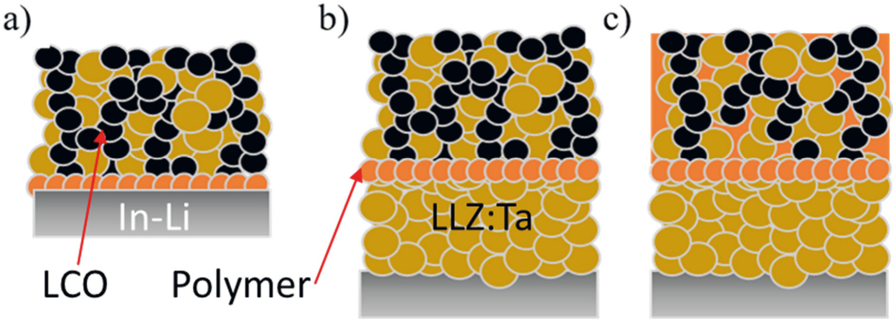

Fig. 3.6. Schematic of polymer-ceramic ASSLB designs. In a) and b) a dense composite cathode is coated with polymer electrolyte. In a) the anode is directly attached to the polymer, in b) the anode is attached to an LLZ:Ta pellet and then glued by polymer onto the composite cathode. In c) the same concept as in b) is used with a porous composite cathode.

A co-sintering of the half-cell is not possible as the high porosity in the LLZ:Ta separator will lead to the formation of Li dendrites. Attaching the anode directly to the composite cathode is the most beneficial setup regarding energy density but requires a method that allows attachment of the anode without punching holes in the polymer layer. Attaching of the liquid MEEP electrolyte to the In or Li foil is not possible as the organic solvents lead to reactions with the In or Li foil

3.4.4. Electrochemical impedance spectroscopy

3.4.4.1. Basics

Electrochemical Impedance Spectroscopy (EIS) is a unique electrochemical method to understand chemical and physical processes. EIS allows the separation of the influences of different components of an electrochemical device [149-151].

In solid electrolytes, the total ionic conductivity, as well as the contributions from bulk and grain boundaries can be accessed [152, 153]. In solid-state batteries, information about the electrodes and the electrode/electrolyte interface characteristics can be collected [153].

3.4.4.2. Theory

In general EIS is conducted by applying an Alternating Current (AC) to a sample and measuring the current flowing it [149, 151]. The excitation signal is small to ensure a pseudo-linear response. The pseudo-linear response will result in a sinusoidal response with the same frequency but shifted in phase. The sinusoidal excitation signal (E_t) is described by Eq. 3.2.

$$E_\mathrm{t} = E_0 \sin(\omega t) \qquad \textbf{Eq. 3.2.}$$

ω is the angular frequency, also described as $\omega = 2\pi f$ with f as the AC signal frequency. In a linear system the AC response signal (I_t) is shifted in phase (φ) (Eq. 3.3).

$$I_\mathrm{t} = I_0 \sin(\omega t + \varphi) \qquad \textbf{Eq. 3.3.}$$

Analogous to Ohms law, the impedance (Z) can be calculated with Eq. 3.4.

$$Z(\omega) = \frac{E_t}{I_t} = \frac{E_0 \sin(\omega t)}{I_0 \sin(\omega t + \varphi)} = Z_0 \frac{\sin(\omega t)}{\sin(\omega t + \varphi)} \qquad \textbf{Eq. 3.4.}$$

Displaying the trigonometric function as complex exponential function gives the real (Z') and imaginary (Z'') components of the complex impedance Z (Eq. 3.5).

$$Z(\omega) = Z_0 \frac{\sin(\omega t)}{\sin(\omega t + \varphi)} = Z_0\, e^{(j\varphi)} = Z' - jZ'' \qquad \textbf{Eq. 3.5.}$$

3.4.4.3. Data Presentation

Often EIS data is presented by plotting the real impedance Z' on the x-axis and the imaginary part Z'' on the y-axis [149, 151]. This representation is called "Nyquist plot" or "Cole-Cole plot". In general, the y-axis is negative [149, 151]. Each point in the Nyquist plot is measured at a certain frequency value. However, no frequency information is found in the Nyquist plot and has to be given additionally. In order to make Nyquist plots comparable a squared display is chosen [149].

In a Nyquist plot, semicircles, or parts of it are observed. The semicircles represent different polarization processes relating to the solid electrolyte, the electrode(s), and the solid electrolyte/electrode interface. The impedance spectra represent imaginary and real impedances. The imaginary impedance is capacitive, and the real ones are resistive. In order to gain information about the different processes, the EIS spectra can be fitted with an equivalent circuit.

3.4.4.4. Equivalent circuits

Possible circuit elements and their impedance response are shown in Fig. 3.7 [149, 151]. Each circuit element has a characteristic impedance. By combination of circuit elements, chemical and physical processes are described. The constructed equivalent circuit is then simulated and fitted to the experimental EIS data.

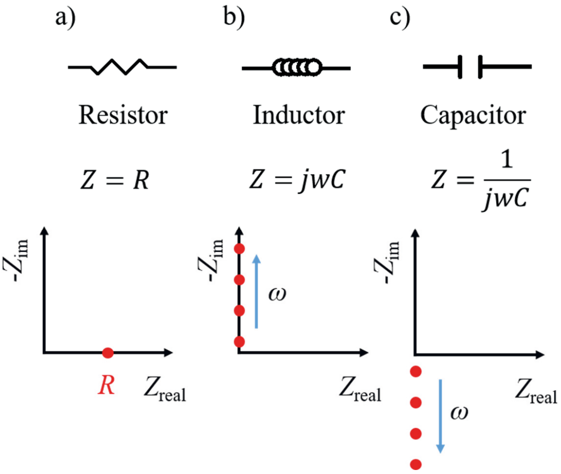

Fig. 3.7. Passive elements that serve as components of an electrical circuit, their impedance *Z* and appearance (marked in red) in the Nyquist plot (bottom) [149]. With *R* as an ohmic resistance, *j* as imaginary unit, *ω* as the angular frequency, and *C* as the capacity.

In batteries, the inductor is, in general, not necessary to fit the EIS spectra. However, the wiring could cause some inductance [149, 151].

In experimental EIS data, the observed semicircles are often flattened. In such cases the capacitor is replaced with a so called "Constant Phase Element" (CPE) [149, 151]. The CPE is a tool to mathematically describe a real, non-perfect capacity. The Z_{CPE} is described by Eq. 3.6.

$$Z_{CPE} = \frac{1}{C_{CPE}\,(j\omega)^{n}} = \frac{1}{\left(R_{CPE}{}^{(1-n)/n} \cdot C_{CPE}{}^{1/n}\right)(j\omega)^{n}} \qquad \textbf{Eq. 3.6.}$$

With *C* as the capacity, *j* as imaginary unit, *ω* as the angular frequency, and *R* as an ohmic resistance. The exponent n has a value between 0 and 1. In the case of n = 0 the CPE describes an ideal ohmic resistor and for n = 1 an ideal capacitor. Additionally, for n = 0.5 the CPE describes a pure diffusion process, a so called Warburg diffusion [149].

Furthermore, CPEs are often used to describe blocking electrodes [149]. In experimental data, blocking layers often show some diffusion, e.g. Li^+ in Au layers or LCO cathodes (e.g. Fig. 4.15 and Fig. 4.26). These blocking electrodes are, therefore, better represented with a CPE instead of a capacitor.

3.4.4.5. Interpretation of the equivalent circuit fit

The interpretation of the fit can be done via the calculated capacity values (Tab. 3.3) [154]. This can be seen as a guideline for the interpretation.

However, the calculated capacity values might not match with the values given in Tab. 3.3. In EIS spectroscopy, each chemical or physical process has a certain frequency at which the process is observed. For ASSLB, the frequency to observe the grain boundary and bulk conduction or the electrolyte/anode and electrolyte/cathode interface is similar at ambient temperatures [155]. The semicircles therefore overlap, and the calculated capacity describes both effects [153, 155]. Of course, lower measuring temperature is helpful to separate those processes but is not always possible.

Tab. 3.3. Typical capacity values and their possible related phenomena [154].

Capacity (F)	Responsible phenomenon
$\mathbf{10^{-12}}$	Bulk
$\mathbf{10^{-11}}$	Minor, second phase
$\mathbf{10^{-11} – 10^{-8}}$	Grain boundary
$\mathbf{10^{-10} – 10^{-9}}$	Bulk ferroelectric
$\mathbf{10^{-9} – 10^{-7}}$	Surface layer
$\mathbf{10^{-7} – 10^{-5}}$	Sample/electrode interface
$\mathbf{10^{-4}}$	Electrochemical reaction

3.4.4.6. Calculation of the ionic conductivity

The ionic conductivity σ of electrolytes is calculated with Eq. 3.7 by using the height of the sample l, the sample surface area A and the ohmic resistance R [156].

$$\sigma_{\mathrm{x}} = \frac{l}{A \times R_{\mathrm{x}}} \qquad \textbf{Eq. 3.7.}$$

The ionic conductivity σ of the grain boundary (gb) and bulk (b) of the solid electrolyte can be calculated by replacing R with the fitted ohmic resistances (R_{gb} and R_{b}). The total ionic conductivity σ is calculated by the sum of both.

3.4.4.7. Measurements

The electrochemical impedance spectroscopy was performed with a VMP-300 multichannel Potentiostat (BioLogic) or a system from Novocontrol, the Alpha-A, which included a temperature control unit, with a liquid nitrogen containing cooling system and a furnace. The temperature for the VMP-300 multichannel Potentiostat was controlled with an external VT 4002EMC climate chamber (Vötsch Industrietechnik).

The setup was 7 MHz or 3 MHz to 1 Hz or 0.1 Hz at intervals of 20 points per decade and with an amplitude of 10 mV for perturbation field for the VMP-300 multichannel Potentiostat. The frequency range of the Alpha-A was from 3 GHz to 1 Hz with otherwise identical parameters.

3.4.4.8. Ionic conductivity

The ionic conductivity was measured at 25 °C or 80 °C with the VMP-300 multichannel Potentiostat or from -60 °C to 120 °C with the Alpha-A. The measured data was adjusted to the dimension of the sample (multiplied with the conducting area and divided by the height of the sample). The fitting of the measured data was performed using the software “ZView” (Scribner Associates Inc.).

3.4.5. Electrochemical cycling

The assembled full cells placed and sealed in Swagelok cells were used as ASSLBs. The battery characterization was done at 80 °C or 100 °C (VT 4002EMC). Long term cycling was performed with a Constant-Current-Constant-Voltage (CC-CV) mode for charging and with constant current for discharging. The batteries were charged to 3.4 V or 3.6 V vs In–Li (i.e. 4.0 V or 4.2 V vs Li/Li^+) with a constant current density of 50 µA cm^{-2} and held at this voltage to allow the current density to drop to 10 µA cm^{-2}. Discharge of the batteries was done with a constant current density of 50 µA cm^{-2} until the voltage was dropped to 2.8 V vs In-Li.

4. Results and Discussion

4.1. Manufacturing of the composite cathode

The first priority was the selection of a thermally stable CAM/solid electrolyte material combination. This material combination was used to develop a FAST/SPS sintering process. The FAST/SPS process is influenced by multiple parameters such as material selection, atmosphere, temperature, pressure, grain size, and dwell time. Their impact on the phase stability, density, microstructure, and electrochemical properties is evaluated.

4.1.1. Material selection

In-situ HT-XRD was used to detect suitable CAM and LLZ:Ta combinations for the preparation of composite cathodes.

Firstly, the XRD patterns of pure LLZ:Ta were analyzed. The XRD patterns show the typical peaks of cubic phase LLZ:Ta at temperatures up to 500 °C and above 800 °C (Fig. 4.1). At intermediate temperatures between 550 °C to 650 °C, XRD patterns show the formation of a pyrochlore phase $La_2Zr_2O_7$. The pyrochlore phase has only negligible ionic conductivity and has to be avoided [108, 157]. In the case of LLZ, the pyrochlore phase formation is reported for the temperature range between 450 °C and 550 °C [158]. Ta substituents, which contract the lattice of the cubic LLZ phase [29], might be responsible for the elevated temperatures of pyrochlore phase formation within LZZ:Ta (Fig. 4.1).

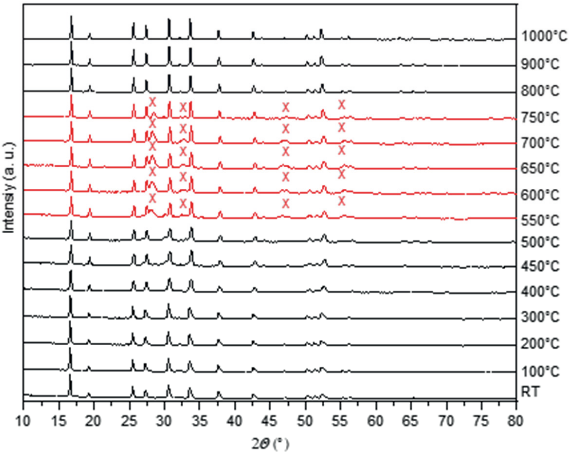

Fig. 4.1. HT-XRD of LLZ:Ta mixture in air at various temperatures. XRD patterns in red color show the peaks due to the pyrochlore phase (i.e. $La_2Zr_2O_7$ marked with X) formation.

The pyrochlore phase formation points toward a fundamental issue associated with the co-sintering of LLZ and CAMs, as the intermediate temperature range might be essential for the co-sintering of CAM and LLZ:Ta.

The thermal stability of LLZ:Ta mixture with CAMs ($LiMn_{1.5}Ni_{0.5}O_4$ (MNO), $LiNi_{0.33}Mn_{0.33}Co_{0.33}O_2$ stabilized with Mg (NMC:Mg) and with Mg and Al (NMC:Mg-Al), and LCO) was characterized by *in-situ* HT-XRD (Fig. 4.2). MNO is the least thermally stable CAM when mixed with LLZ:Ta. Decomposition phases can be seen already at around 500 °C (Fig. 4.2a). Mixtures of NMC:Mg and NMC:Mg-Al with LLZ:Ta are slightly more thermally stable, and the decomposition of phases are observed above 600 °C (Fig. 4.2b and c). On the other hand, the LCO/LLZ:Ta mixture is the highly stable one and it shows no decomposition up to 1000 °C (Fig. 4.2d) [159]. The LCO/LLZ:Ta mixture was melted at around 1100 °C, although neither LCO nor LLZ:Ta should melt at this temperature. Furthermore, the pyrochlore phase $La_2Zr_2O_7$ is also absent in the LLZ:Ta mixture with LCO. This could be ascribed to the high peak intensity of LCO and low intensity of the $La_2Zr_2O_7$ peaks.

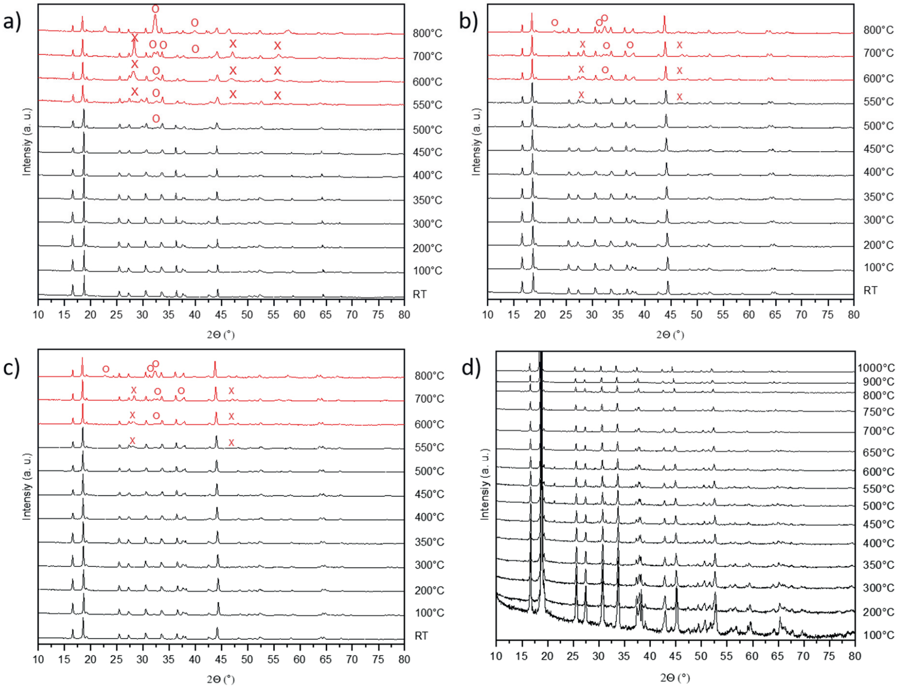

Fig. 4.2. HT-XRD of CAM/LLZ:Ta mixture in air at the given temperature: a) MNO, b) NMC:Mg, c) NMC:MgAl, and d) LCO. Besides the pyrochlore phase $La_2Zr_2O_7$ (X), unknown phases, related to the decomposition of the CAM are found (marked by red color and 0).

The reason for the decomposition within the CAMs is most likely a result of the loss of Li. Thermal Gravimetric Analysis (TGA) analysis reveal that all CAM/LLZ:Ta mixtures have a mass loss at around 100 °C, 200 °C – 250 °C, and 450 °C (Fig. 4.3) [108, 158, 160-162]. The evaporation of adsorbed water causes the weight loss around 100 °C, and evaporation of absorbed water and CO_2 occurs in between 200 °C and 250 °C [163]. At around 450 °C predominantly CO_2 is evaporated. The differential thermal analysis (DTA) signal for all CAM/LLZ:Ta mixtures decreases continuously with increasing temperature in each sample.

For MNO, the mass is decreased around 2 wt-% between 450 °C and 600 °C (Fig. 4.3a). This mass loss relates to the full amount of Li in the MNO structure. The MNO structure, therefore, is most likely wholly collapsed above 600 °C. Both NMC (Mg and Mg-Al stabilized) species show a continuous mass loss above 450 °C (Fig. 4.3b and c). This mass loss is negligible up to 800 °C (around 0.5 wt-%), and increases for higher temperatures afterwards. At 1100 °C, the mass loss for NMC:Mg is approximately 2.5 wt-% and for NMC:Mg-Al is around 2 wt-%. As the Li amount in NMC is around 7 wt-% and half of the total mass is LLZ:Ta, the Li loss is significant and should also lead to a collapse of the NMC structure. LCO shows the highest thermal stability (Fig. 4.3d). Above 450 °C, the total mass loss is around 0.3 wt-%, and the loss is observed only up to 700 °C. This might mean that the mass loss could also partially result from CO_2 removal and not Li [163].

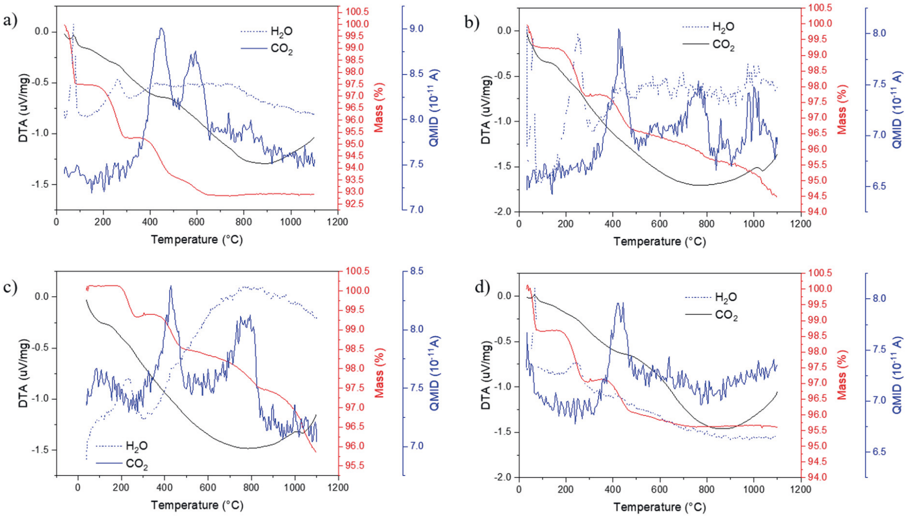

Fig. 4.3. DTA/TGA coupled with mass spectrometry measurements (Quasi Multiple Ion Detection (QMID)) for CAM/LLZ:Ta mixtures: a) MNO, b) NMC:Mg, c) NMC:Mg-Al, and d) LCO.

No significant endo- or exothermic peak, that characterize a phase change, are observed for all CAM/LLZ:Ta mixtures within the measured temperature range.

From the *in-situ* HT-XRD and the TGA analysis results, it is evident that the thermal stability of the CAMs is similar except for LCO (Fig. 4.4). Thus, co-sintering of MNO and NMC with LLZ:Ta has to be performed at a sintering temperature below 550 °C and 600 °C, respectively. This sintering temperature is significantly lower than the normal sintering temperature of LLZ (above 1000 °C) and is in the temperature range of pyrochlore phase formation in LLZ:Ta. In the case of slow kinetics, advanced sintering techniques with short dwell time could prevent the formation of significant amounts of secondary phase and enable the co-sintering of MNO and NMC with LLZ:Ta. However, LCO shows better thermal stability with LLZ:Ta. Co-sintering of LCO and LLZ:Ta is possible up to 1050 °C, which is in good agreement with the reported stability up to 1085 °C [159]. Hence, LCO is considered the most promising CAM for the co-sintering with LLZ:Ta and for preparing composite cathodes.

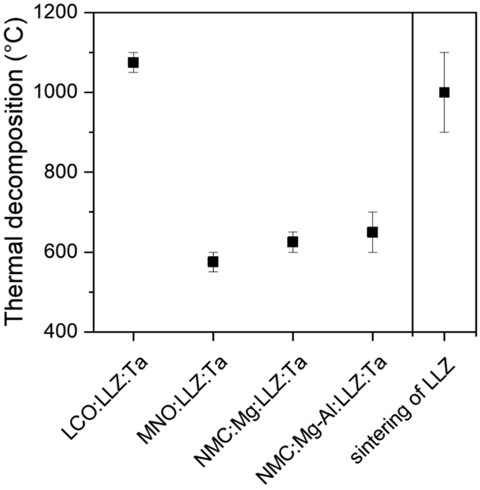

Fig. 4.4. Thermal stability of CAM/LLZ:Ta mixtures based on Fig. 4.2 and Fig. 4.3 compared to the conventional sintering temperature of LLZ:Ta [14].

4.1.2. Thermal stability in vacuum and Ar

The atmosphere significantly affect the thermal stability and sintering of materials [17, 164]. Vacuum and Ar atmospheres have been evaluated as possible atmospheres for the FAST/SPS process (Fig. 4.5). Thermal stability was measured by TGA measurements. The TGA measurements were similarly designed as the FAST/SPS process. In the LLZ:Ta and LCO powders and the LLZ:Ta/LCO powder mixture, a piece of graphite foil (G) was placed. The measurements in vacuum show that pure graphite foil is stable up to around 1000 °C, so that mass loss at lower temperatures is a result of decomposition of either LLZ:Ta or LCO (Fig. 4.5a). For the LLZ:Ta containing samples a mass loss is observed at around 200 °C and 400 °C due to the removal of absorbed H_2O and O_2 (compare with Fig. 4.3). The G-LCO sample is stable up to 850 °C. However, literature reports suggest that LCO can react with graphite above 550 °C and form $Li_{1-x}CoO_{1-y}$, CO_x, and Li_2O [165]. Besides CO_x, these materials are solid at intermediate temperatures and might not cause significant mass loss. Furthermore, the reaction kinetics might be slow.

For G-LLZ:Ta stability is observed up to a little more than 600 °C and for the G-LLZ:Ta/LCO mixture stability is between, at around 650 °C.

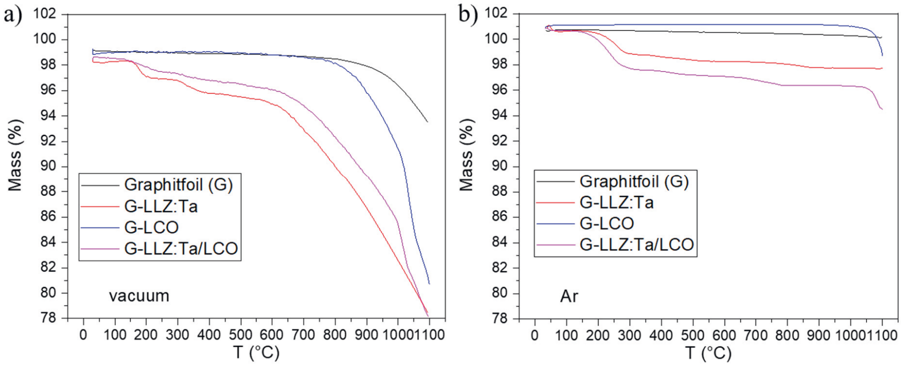

Fig. 4.5. TGA measurements of graphite foil and graphite foil with LLZ:Ta, LCO and the LLZ:Ta/LCO mixture in vacuum and Ar.

In the Ar atmosphere, the graphite foil is stable up to 1100 °C (Fig. 4.5b). The LCO, LLZ:Ta, and the LLZ:Ta/LCO mixture are thermally more stable. Only above 1050 °C the decomposition of LCO is observed (similar to section 4.1.1). This matches well with literature that reports the thermal stability of LCO in Ar is around 1050 °C [166-168]. The LLZ:Ta containing samples also show the mass loss at 200 °C and 400 °C. However, their thermal stability is high, and only a small mass loss around 2 % is observed up to 1100 °C. For G-LLZ:Ta and G-LLZ:Ta/LCO, only a slight mass loss is observed at high temperatures, which intensifies above 1050 °C in good agreement with G-LCO.

The different observed thermal stabilities are most likely a result of the atmospheric pressure. Low pressure in vacuum is beneficial for evaporation. In the TGA setup under vacuum, the pressure is around 10^{-3} mBar. This is comparable to the vacuum in the FAST/SPS sintering chamber. For Ar atmosphere, the pressure is about 1 Bar. The higher pressure will result in slower evaporation and hence higher thermal stability. Also, the O_2 in the atmosphere can be crucial. The Ar has a high purity of 99.999 %, and, therefore, the oxygen partial pressure is low. In vacuum the total pressure is 10^{-3} mBar out of which roughly a fifth is oxygen (due to the air atmosphere before evacuation). The graphite foil might start to react with the remaining oxygen and could trigger further reactions.

The vacuum could be used as FAST/SPS sintering atmosphere below 550 °C which is rather limiting. The expectation that a slow reaction rate and short dwell times of the FAST/SPS process might prevent the formation of significant secondary phases failed (Fig. 4.7a).

In order to enable higher sintering temperatures and to prevent possible degradation and secondary phase formation Ar was chosen as the most suitable atmosphere (Fig. 4.5).

4.1.3. Sintering of single phases

At first the single phases of LCO and LLZ:Ta were sintered by FAST/SPS at 50 MPa for 10 min in Ar. The obtained densities are shown in Fig. 4.6 and indicate that LCO nearly fully densifies (95 %) at 800 °C and is fully dense above 850 °C, while LLZ:Ta only reaches a density of 88 % at 1050 °C. The sintering temperature was limited due to the requirement of the thermocouple which was only usable up to around 1100 °C.

In FAST/SPS sintering, LCO is sintered at lower temperatures than LLZ:Ta (Fig. 4.6). Due to the mixing ratio of the same volume LCO and LLZ:Ta, the LCO can form a rigid percolation network. The sintering process of the LLZ:Ta can be hindered at the LCO/LLZ:Ta interface due to interfacial stresses. Such stresses can, for example, result from different densities between the phases or crystal structures (lead to residual stress during cooling). LCO has a rhombohedral structure with a lattice parameter *a*: 2.87 Å and c: 14.05 Å [126], while LLZ:Ta is cubic with a lattice parameter *a*: 12.95 Å – 12.97 Å[29]. Within the single materials, the sintering is not hindered.

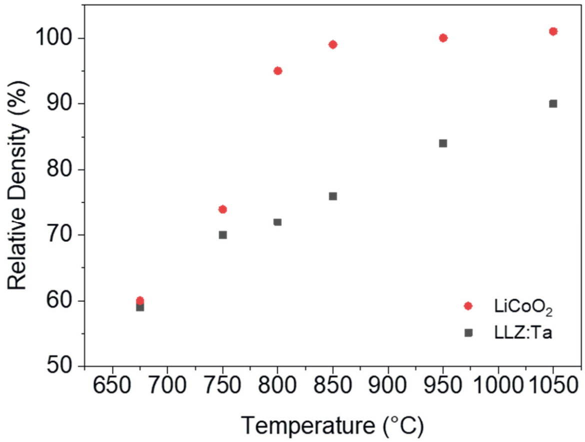

Fig. 4.6. Densities of pure LCO and LLZ:Ta pellets after FAST/SPS sintering in Ar at 50 MPa.

4.1.4. Phase stability of the composite cathode

4.1.4.1. Temperature

The phase stability of LCO and LLZ:Ta is essential to achieve good interfacial and bulk ion and electron transport in the LCO/LLZ:Ta composite cathode. XRD patterns of the LCO/LLZ:Ta composite cathode prepared at various FAST/SPS sintering temperature were used to characterize the phase stability. The obtained XRD patterns were then compared with the corresponding XRD patterns of pristine LCO and LLZ:Ta powders (Fig. 4.7a). Every observed peak is sharp and indicates good crystallinity after FAST/SPS sintering. For sintering temperatures between 800 °C and 675 °C, the typical peaks for rhombohedral LCO and cubic LLZ:Ta are found besides some other peaks with low intensities (Fig. 4.7a). Rietveld refinement suggests that these peaks are related to $La_2Li_{1-x}Co_xO_4$ (23°, 27°, and 32°) and CoO (36°, 42°, and 61 °) with an amount of 11 wt- % and 10 wt- % for the samples sintered at 800 °C and 675 °C, respectively (Fig. 4.7 and Tab. 4.1).

Although it was not observed in TGA (4.1.2) it is possible that the FAST/SPS processing lead to a significant reaction of LCO with the graphite foil to form $Li_{1-x}CoO_{1-y}$, CO_x, and Li_2O as suggested by Takahara et al. [165].Such secondary phases will lead to lower capacity and ionic conductivity [1, 3, 27].

4.1.4.2. Applied mechanical pressure

The used FAST/SPS device can apply a maximum mechanical pressure of 440 MPa with the used setup (see section 3.2.1). The XRD patterns of LCO/LLZ:Ta composite cathodes at high applied pressure show a similar high crystallinity (Fig. 4.7b). However, the intensity of peaks related to secondary phases is drastically reduced. The Rietveld analysis gives only 4 wt-% of secondary phases for 750°C and 675°C sintering temperature (Tab. 4.1). At 800 °C, the secondary phase content increases up to 13 wt-%, and shows $La_2Li_{1-x}Co_xO_4$, CoO, and $La_2Zr_2O_7$ (34°) phases. This suggests that the high applied pressure is only beneficial up to a threshold temperature, as with low pressure, the 800 °C sample shows a slightly lower amount of secondary phases.

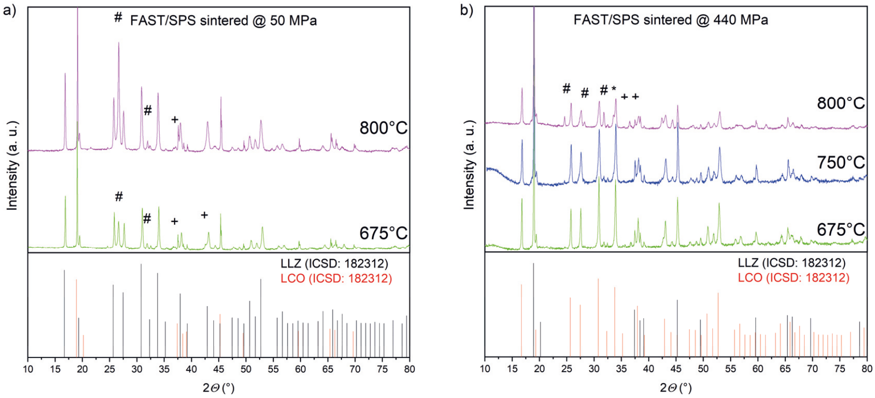

Fig. 4.7. XRD patterns of pristine LCO and LLZ powders and sintered LCO/LLZ:Ta composite cathode. The composite cathode was sintered by FAST/SPS at different temperatures under a mechanical pressure of a) 50 MPa and b) 440 MPa. The secondary phases are marked with: # for $La_2Li_{1-x}Co_xO_4$, + for CoO, and * for $La_2Zr_2O_7$.

Tab. 4.1. Rietveld refinement of the LCO/LLZ:Ta composite cathode after FAST/SPS in Ar for 10 min at a) 50 MPa and b) 440 MPa.

a)

Temperature (°C)	LLZ:Ta (wt-%)	LCO (wt-%)	Secondary phase (wt-%)	
675	54	36	CoO	8
			$La_2Li_{1-x}Co_xO_4$	2
800	56	33	CoO	7
			$La_2Li_{1-x}Co_xO_4$	4

b)

Temperature (°C)	LLZ:Ta (wt-%)	LCO (wt-%)	Secondary phase (wt-%)	
675	52	44	CoO	3
			$La_2Li_{1-x}Co_xO_4$	1
750	50	46	CoO	2
			$La_2Li_{1-x}Co_xO_4$	2
800	50	37	CoO	8
			$La_2Li_{1-x}Co_xO_4$	3
			$La_2Zr_2O_7$	2

The striking difference in secondary phase formation between FAST/SPS sintering at 50 MPa and 440 MPa can be understood when considering the effect of applied pressure and short sintering time on the origin of the secondary phases. First, the appearance of CoO is a direct result of the reaction between LCO and graphite foil at temperatures above 500 °C resulting in the formation of Li_2O, CO_x, and CoO (Eq. 4.1) [17, 165, 166]. The pores and thus the free surface area available for reaction are quickly reduced and limit carbon diffusion into the sample by applying the high mechanical pressure even before the pressure assisted sintering starts. Only the material in direct contact with graphite foil decomposes but can be removed later by surface polishing.

Second, the products of the reaction between LCO and LLZ:Ta, such as $LaCoO_3$, La_2CoO_4 or Co-substituted LLZ:Ta, are often formed in conventionally sintered LCO/LLZ samples due to long sintering time [16, 111]. Short heating and dwell time in the FAST/SPS process kinetically limit these reactions, contributing to reduced secondary phases. Moreover, the reactions are further limited by low sintering temperatures used during FAST/SPS, which are far below the reported 1085 °C at which LCO and LLZ start to react with a visible rate (Fig. 4.4) [159].

Third, the formation of a pyrochlore $La_2Zr_2O_7$ phase due to delithiation of LLZ is also often observed in conventionally sintered samples [58, 108, 111, 145]. In the FAST/SPS process, short sintering time, applied pressure, and closed sintering mold, results in negligible Li loss due to evaporation or reaction with carbon from the graphite foil up to 750°C (Fig. 4.7b).

The mechanical pressure has to be applied prior to heating (Fig. 4.8a and b). In case the high pressure is only applied to the sample at high temperature, the pressure might even enhance the reaction with the graphite foil (Fig. 4.8c). Most likely, this is explained by the loss of sample material. The mold shows clearly material residue after the FAST/SPS process (Fig. 4.8d). At 462 °C the LiOH in the LLZ:Ta (20 molar-% excess) melts and is pressed out of the mold by applying high mechanical pressure only at high temperature. This can drag additional material, and the otherwise loose or melted powder will be pressed out (Fig. 4.8d).

The application of high mechanical pressure at high temperature enhances the decomposition of the materials. First, the loss of Li by removal of LiOH will be enhanced by the application mechanical pressure at high temperature. The Li loss leads to instability in LLZ:Ta and to the formation of $La_2Zr_2O_7$ and $LaTa_3O_7$ with a higher molar density [108, 157]. Second, nearly the whole LCO has disappeared, suggesting that the decomposition rate is enhanced (Eq. 4.1 and Eq. 4.2).

$$LiCoO_2 \rightarrow Li_{1-x}CoO_{2-y} + 0.5\cdot Li_2O$$ **Eq. 4.1.**

$$Li_{1-x}CoO_{2-y} + 0.5\cdot(2-y)\cdot C \rightarrow CoO + 0.5\cdot(1-x)\cdot Li_2O + 0.5\cdot(2-y)\cdot CO_2$$ **Eq. 4.2.**

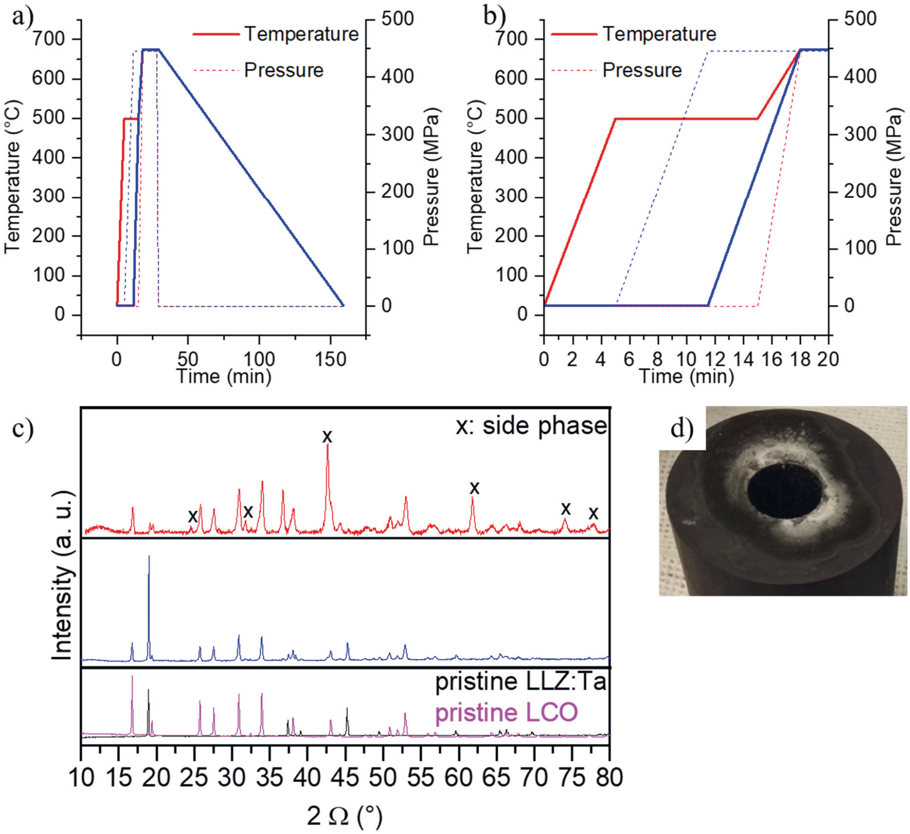

Fig. 4.8. a) FAST/SPS process scheme showing the temperature and pressure values. In b) a detailed view of a) is shown. The XRD pattern of the two possible pressure schemes varies (c). In d) the mold after the FAST/SPS process when the pressure is applied after heating shows clearly material residue.

4.1.4.3. Manufacturing of porous composite cathodes

The preparation of the porous composite cathode is challenging. Based on Fig. 4.7, the lower pressure during FAST/SPS processing leads to secondary phases. However, a possible work around was found. The secondary phases are a result of the LCO and LLZ:Ta reacting with the graphite foil discs. Replacing the graphite foil discs with mica foil discs allows the FAST/SPS sintering at lower applied mechanical pressure and avoided the formation of secondary phases such as $La_2Li_{1-x}Co_xO_4$ (23°, 27° and 32°) and CoO (36°, 42° and 61) (Fig. 4.9).

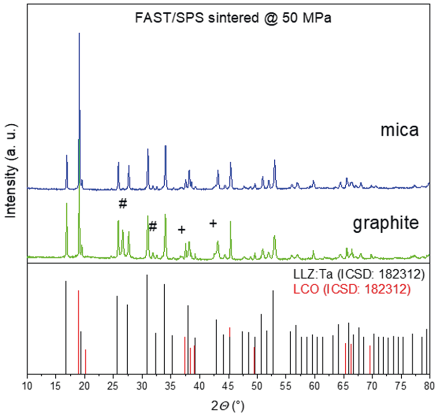

Fig. 4.9. XRD patterns of pristine LCO and LLZ:Ta powders and sintered LCO/LLZ:Ta composite cathode. The composite cathode was sintered by FAST/SPS at 675 °C under a pressure of 50 MPa and graphite or mica foil discs.

Replacing the graphite foil discs allows the FAST/SPS sintering of composite cathodes with lower applied mechanical pressure. The applied mechanical pressure can be chosen relatively freely and allows to control the porosity of the composite cathode, without the need for pore former. However, a mechanical pressure of 50 MPa was required to obtain a mechanically stable composite cathode. The porosity of the composite cathode can be controlled via the applied mechanical pressure during FAST/SPS sintering in the range between 5 % and 20 % (Fig. 4.10).

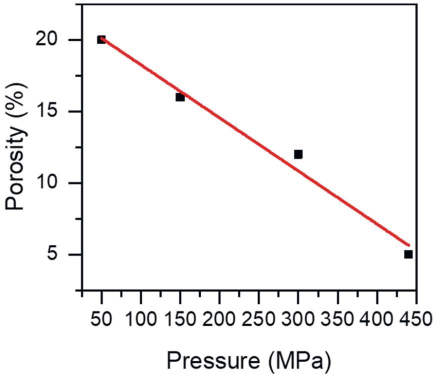

Fig. 4.10. Porosity in the LCO/LLZ:Ta composite cathode sintered by FAST/SPS at a temperature of 675 °C for 10 min in Ar with various applied mechanical pressure.

4.1.5. Grain size

The grain size significantly influences the sintering process and the total ionic conductivity [41, 169, 170].

The optimal grain size of LLZ to obtain high total ionic conductivity is a controversial topic. Some reports suggest larger grains are beneficial as they minimize the amount of low conductive grain boundaries [171, 172]. In contrast others claim that smaller grains are beneficial as the grain boundary conduction is higher than for the bulk [169, 170]. Smaller grains might also show enhanced sintering rate [41]. However, these reports normally use different synthesis, processing (sintering technique, dwell time, and sintering temperature), and measuring conditions (temperature and surface treatment) and do not allow direct comparison [169-172].

In this work, LLZ:Ta powders with a median grain size of 1 µm and 10 µm, have been used for FAST/SPS sintering in Ar with 10 min dwell time at 675 °C and 440 MPa applied mechanical pressure (Fig. 4.11). The density of both LLZ:Ta pellets with smaller and larger grains was 92 % (geometric method, error bar: ± 2 %). The initial particle size seems, therefore, to be secondary for the FAST/SPS sintering process.

Besides, the grain size, the applied mechanical pressure can significantly impact the sintering rate and final density. The high applied mechanical pressure compacts the powder which results in contact stress. The contact stress also increases the driving force for the sintering of the material, especially during the initial stage of sintering [41, 173]. This could mean that the high applied mechanical pressure is the determining factor of the sintering process. The grain size might only be a secondary parameter for the sintering process.

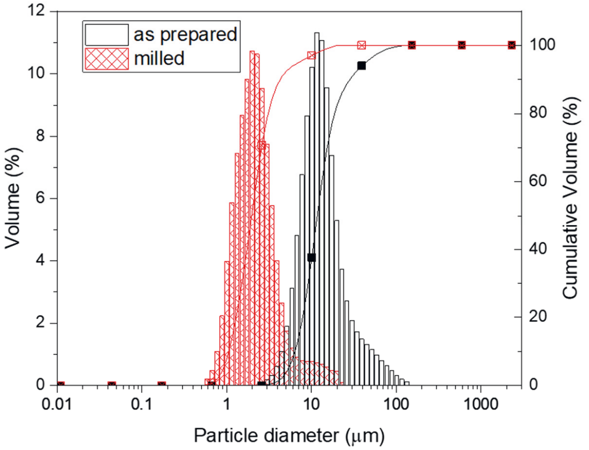

Fig. 4.11. The grain size of LLZ:Ta used as prepared and after planetary ball milling (3 h, 200 rpm) and sieving (20 µm).

4.1.6. Dwell time

In the FAST/SPS processes, the dwell time is regularly within a couple of minutes. The short dwell times are ideal for maintaining the phase of composite materials. The necessary dwell time is closely linked to the densification kinetics. In general, the densification for samples under uniaxial pressure can be calculated via Eq. 4.3 and Eq. 4.4.

$$\rho = \rho_0 \cdot \exp(-\varepsilon_Z) \qquad \textbf{Eq. 4.3.}$$

$$\varepsilon_Z = \ln\left(\frac{h}{h_0}\right) \qquad \textbf{Eq. 4.4.}$$

Where p_0 is the relative density of the initial body, and h and h_0 are the current and initial sample height, respectively. As the powders are pressed by hand prior to the FAST/SPS process, the initial density varies, and Eq. 4.3 and Eq. 4.4 cannot be used to describe the densification. Hence, the densification of LCO, LLZ:Ta, and the mixture of both will be related to the piston movement during the FAST/SPS process, and the relative density is calculated for the sintered pellet by the geometric method after the FAST/SPS sintering process (Fig. 4.12).

As the powders are only pre-pressed by hand before the FAST/SPS process, the densification starts when the mechanical pressure is applied in the FAST/SPS device. Around half of the total piston displacement can be observed by only applying the mechanical pressure (Fig. 4.12). Each densification curve shows a small step due to the waiting time between the pressure build-up and the start of the heating which is required by the FAST/SPS device. The powders have already high density when the sintering temperature is reached (more than 90 %

displacement of the piston). During the dwell time of 10 min, the piston only moves slightly, around 0.3 mm, and most of this displacement occurs within the first five minutes.

After the FAST/SPS process the relative density reaches 99 % for LCO, 90 % for LLZ:Ta, and 92 % for the mixture (Fig. 4.12). Therefore, LCO is fully dense (Fig. 4.12a and b). As the LLZ:Ta has to act as a separator in ASSLBs, only closed porosity can remain within the LLZ:Ta pellet to prevent open porosity that could lead to Li dendrite formation in an ASSLB [41, 133]. This should be the case for a density of at least 90 %. Therefore, the obtained density of LLZ:Ta is just sufficient (Fig. 4.12c and d). Shorter dwell times could lead to too low density. The mixture reaches a high density of 92 % (Fig. 4.12e and f), which allows for high energy density in the latter composite cathodes.

After 10 min of sintering, the pistons movement is very low (Fig. 4.12). Even higher densities would only be possible with prolonged dwell times. Longer dwell times would on the other hand lead to secondary phase formation with unfavorable electrochemical properties (see also Fig. 4.7 and Tab. 4.1).

The sintering temperature can be increased slightly, as otherwise significant secondary phase formation occurs (Tab. 4.1). For a sintering temperature of 750 °C, secondary phase formation is still negligible (Tab. 4.1), and the density of the LLZ:Ta pellet increased to 92 % and for LCO/LLZ:Ta mixture to 95 %.

An increase in the applied mechanical pressure could increase the final density but would either require smaller samples in diameter or another FAST/SPS device as the maximum force is applied. Also, a fully dense composite cathode might be a disadvantage due to the volume expansion of LCO during delithiation [62], leading to the destruction of the LCO/LLZ:Ta interface.

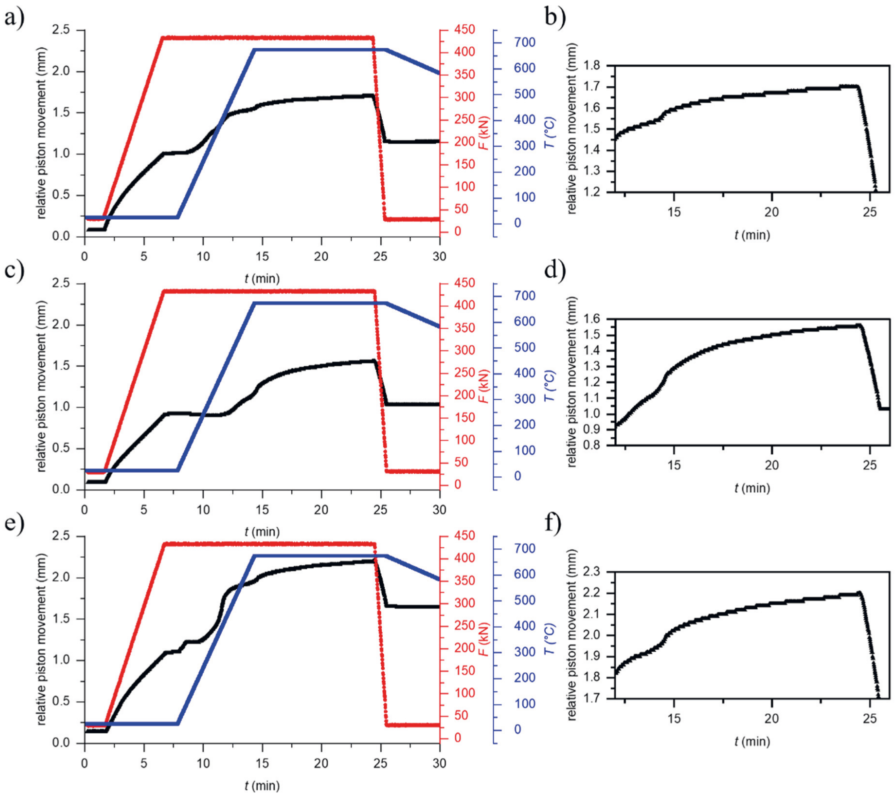

Fig. 4.12. Piston movement (black) during FAST/SPS at 675 °C and 440 MPa in Ar of a,b) LLZ:Ta, c,d) LCO, and e,f) LCO/LLZ:Ta (b, d, and f is an inset of a, c, and e). The piston movement can be linked to the densification but also contain the effects of thermal expansion of the tools. The densification is driven by the applied mechanical pressure (red) and temperature (blue).

4.1.7. Influence of LLZ:Ta pretreatment

LLZ is stable in ambient atmospheres [14, 29]. However, long-term exposure to air can lead to surface contaminants [160]. The impact of surface contaminants from the air was studied on LLZ:Ta separators prepared by FAST/SPS with respect to achieved density, microstructure and electrochemical properties.

Several research groups reported the formation of protonated $Li_{7-x}H_xLa_3Zr_2O_{12}$ and LiOH when LLZ was exposed to moisture from air according to reaction (Eq. 4.5). Subsequently, LiOH converts to Li_2CO_3 due to interaction with CO_2 [160-162, 174]. Besides, CO_2 might also directly react with LLZ (Eq. 4.6) [109].

$Li_7La_3Zr_2O_{12} + x \cdot H_2O \rightarrow Li_{7-x}H_xLa_3Zr_2O_{12} + x \cdot LiOH$ **Eq. 4.5.**

$Li_7La_3Zr_2O_{12} + x \cdot CO_2 \rightarrow Li_{7-2x}La_3Zr_2O_{12-x} + x \cdot Li_2CO_3$ **Eq. 4.6.**

Raman spectroscopy can detect the formation of Li_2CO_3 layer on LLZ:Ta surface within a few hours of air exposure (Fig. 4.13).

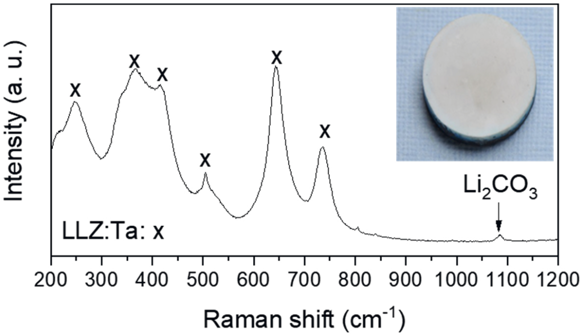

Fig. 4.13. Raman spectrum of LLZ:Ta exposed to air for a couple of days. Besides the LLZ:Ta spectra, marked by X [175, 176], the Li_2CO_3 peak at 1090 cm^{-1} is observed.

According to the literature, the Li_2CO_3 can form a closed layer of around 30 nm in thickness on LLZ particles within a few days of exposure to air [22]. The reactions in Eq. 4.5 and Eq. 4.6 are described by Larraz et al. to be reversible [108]. Besides, both LiOH and Li_2CO_3 melt and start to decompose at 462 °C and 720 °C, repectively. This means that the FAST/SPS sintering temperature of up to750 °C can remove LiOH, but the Li_2CO_3-layer could remain, since the dwell time of only 10 min is rather short compared to the commonly used 2 h annealing in Ar atmosphere at 750 °C to remove Li_2CO_3 [116].

LiOH and Li_2CO_3 layer can impact the sintering behavior and the electrochemical properties. Two types of LLZ:Ta powders were used to fabricate LLZ:Ta separators and composite cathodes. In the first set of experiments, LLZ:Ta powder stored in air for a couple of days was used for sample preparation (LLZ:Ta-air). In the second set of experiments, a part of this powder was annealed in Ar atmosphere at 750 °C for 2 h (LLZ:Ta) before use. The annealing process did not significantly change the particle size and shape (see Fig. 3.1).

4.1.7.1. Density and microstructure

For the high storage capacity and good mechanical stability, ASSLBs require a high density of sintered components. A high-pressure assisted FAST/SPS sintering process (a mechanical pressure of 440 MPa was applied) results in LLZ:Ta layers and composite cathodes with a high density. (Tab. 4.2). An exceptional feature of the developed high-pressure assisted FAST/SPS process is the possibility of achieving a relative density of over 90 % at sintering temperatures as low as 675 °C without any sintering aids. As expected, the relative density slightly increases for a higher sintering temperature of 750 °C to 92 % and 95 % for the pure LLZ:Ta-air and LLZ:Ta and for the composite cathode, respectively. The relative density by the geometric method of LLZ:Ta-air and LLZ:Ta and the composite cathode seems not to be affected by the way of powder preconditioning within the error of density measurements (around ±2 %).

Tab. 4.2. Relative density (%) of pure LLZ:Ta layer and LCO/LLZ:Ta composite cathode sintered by FAST/SPS at 440 MPa in Ar with a dwell time of 10 min at two temperatures by the geometric method with and without air exposure.

FAST/SPS temperature	**Pure LLZ:Ta layers**		**Composite cathodes**	
	LLZ:Ta-air	LLZ:Ta	LLZ:Ta-air	LLZ:Ta
675 °C	90 %	90 %	92 %	92 %
750 °C	92 %	92 %	95 %	95 %

The cross-sectional SEM images of composite cathodes prepared with LLZ:Ta-air and LLZ:Ta powders are shown in. Fig. 4.14a and b. The LCO and LLZ:Ta grains can be clearly distinguished. The LCO and LLZ:Ta-air and LLZ:Ta phases are homogeneously distributed throughout the whole volume, which is beneficial for their application in ASSLBs. Although, the average density of the LLZ:Ta-air and LLZ:Ta-based composite cathode is the same (92 %), the local microstructure is clearly different. The LLZ:Ta-based composite cathode shows a larger number of micro-pores predominantly around LLZ:Ta-air grains. In the LLZ:Ta-based composite cathode, only a small number of micro-pores are found.

The micro-pore formation can be linked to the removal of LiOH (melting and decomposition at 462°C) and Li_2CO_3 (melting and decomposition at 720°C) during FAST/SPS sintering at 750 °C. The same observation is made for the LLZ:Ta-air and LLZ:Ta layers sintered at 750 °C (Fig. 4.14c and d). The LLZ:Ta-air-based layer is compact but features a rather large amount of small encapsulated micro-pores and some relatively large pores that are uniformly distributed within the sintered layer. The small micro-pores are found predominantly around LLZ:Ta-air grains. The pores can be the structural weak points within the LLZ:Ta-air separator and lead to break-outs during polishing of the surface and form the large pores. In the LLZ:Ta layer the larger pores are absent and imply improved sintering. The same relative density of LLZ:Ta-air and LLZ:Ta supports the hypothesis (in the framework of measurement accuracy).

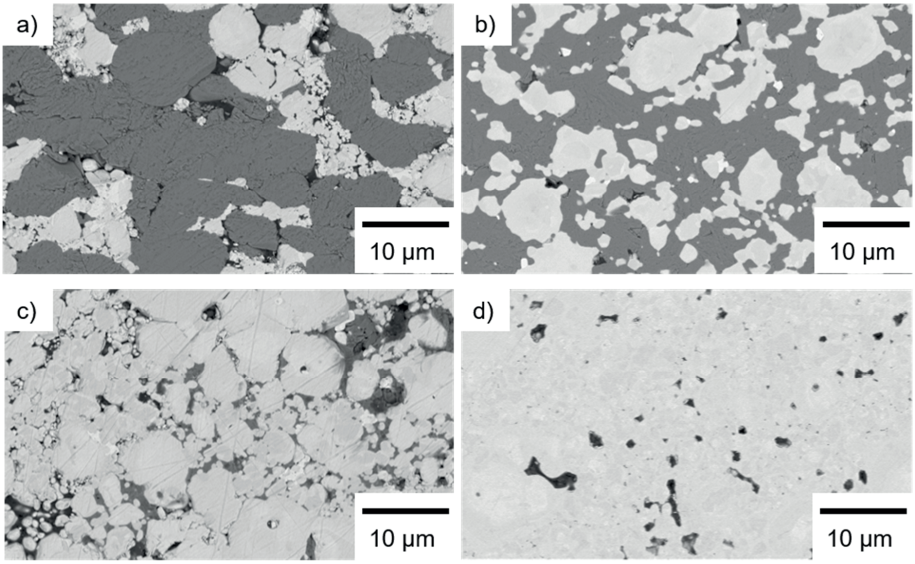

Fig. 4.14. Cross-sectional SEM images of LCO/LLZ:Ta composite cathodes (a, b) and pure LLZ:Ta layers (c, d) after FAST/SPS at 750 °C and 440 MPa in Ar with 10 min dwell time. a) The composite cathode prepared with LLZ:Ta-air powder. b) The composite cathode prepared with LLZ:Ta powder. The bright and dark areas are LLZ:Ta or -air and LCO, black areas represent pores. The LLZ:Ta monolayer prepared with c) LLZ:Ta-air and d) LLZ:Ta.

4.1.7.2. Ionic conductivity of LLZ:Ta pellets

In order to show that the pores in the microstructure of composite cathodes and separators are a result of LiOH and Li_2CO_3 removal, Electrochemical Impedance Spectroscopy (EIS) measurements on pure LLZ:Ta-air and LLZ:Ta separators were performed (Fig. 4.15).

Both LLZ:Ta-air and LLZ:Ta separators sintered at 750 °C (Fig. 4.15a and b) are comparable with each other and show one semicircle at high frequencies, another one at medium frequencies, and the tail from the Au blocking layer. The EIS data was fitted with the equivalent circuits shown in Fig. 4.15, where R represents an ohmic resistance and CPE is a constant phase element. In the case of using a CPE, the capacity C has to be calculated from the fitting values by Eq. 4.7.

$$C = \frac{(Q_0 \cdot R)^{1/\mathrm{n}}}{R} \cdot \sin\left(\frac{\mathrm{n}\pi}{2}\right) \qquad \textbf{Eq. 4.7.}$$

For n > 0.75, Eq. 4.7 can be simplified to Eq. 4.8 [149, 151, 177].

$$C = \frac{(Q_0 \cdot R)^{1/\mathrm{n}}}{R} \qquad \textbf{Eq. 4.8.}$$

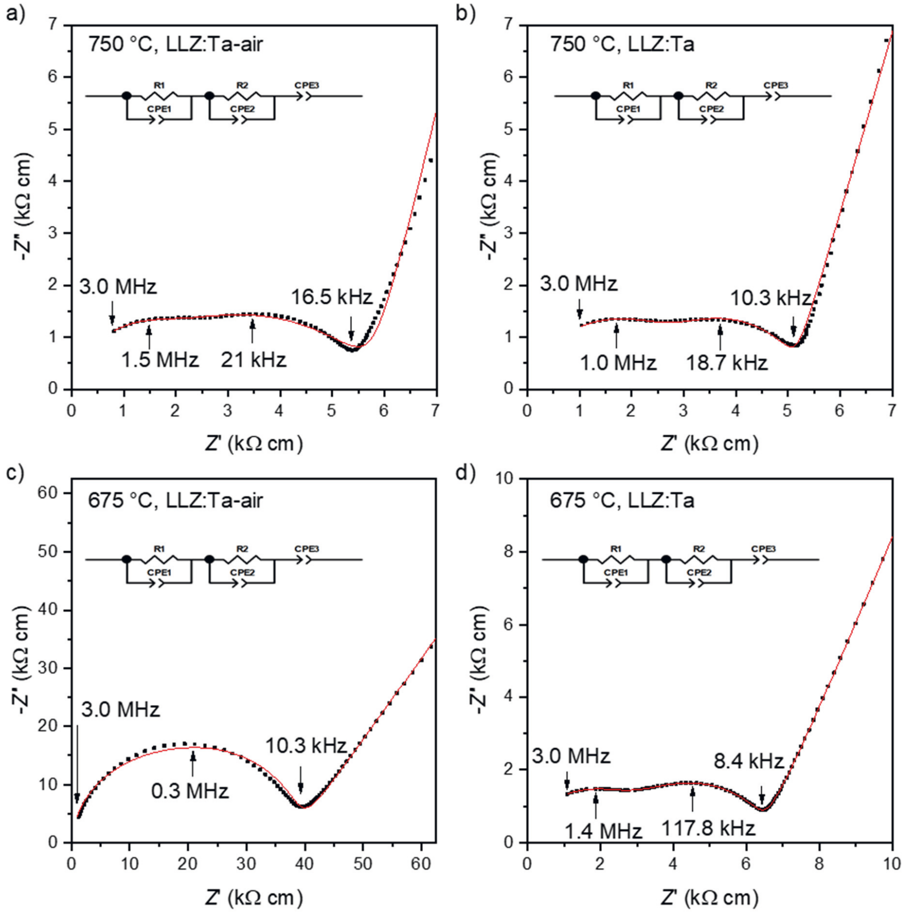

Fig. 4.15. Nyquist-plot for LLZ:Ta-air and LLZ:Ta pellets sintered by FAST/SPS at 675°C and 750°C with 10 min dwell in Ar under a pressure of 440 MPa at RT. Fitting (red lines) was performed with a related equivalent circuit. R represents an ohmic resistance and CPE a constant phase element.

The semicircle at high frequencies (MHz range) is in the capacity range of 10^{-10} F. The semicircle at mid frequencies (kHz range) is in the capacity range of 10^{-8} F. The fitting values can be found in Tab. 4.3. The fitted capacities are not in the expected ranges (Tab. 3.3) [178]. The measurement temperature can alter the dielectric properties and, therefore, the capacity [154]. At elevated temperatures the capacity of bulk and grain boundary can have different values.

Tab. 4.3. Fit results of the RT EIS measurements for LLZ:Ta-air and LLZ:Ta layers sintered at two temperatures. The capacity *C* was calculated by Eq. 4.8.

Sample	LLZ:Ta-air	LLZ:Ta	LLZ:Ta-air	LLZ:Ta
Sintering temperature (°C)	750	750	675	675
Thickness (mm)	3.42	3.65	3.25	6.8
$R1$ (Ω)	704	693	902	2667
CPE1: Q_0 (Ω^{-1} s^n)	$8.46\cdot10^{-10}$	$6.54\cdot10^{-10}$	$4.54\cdot10^{-10}$	$4.47\cdot10^{-10}$
CPE1: n	0.88	0.89	0.91	1
C_1 (F)	$1.20\cdot10^{-10}$	$1.08\cdot10^{-10}$	$1.06\cdot10^{-10}$	$4.47\cdot10^{-10}$
$R2$ (Ω)	878	724	1225	3066
CPE2: Q_0 (Ω^{-1} s^n)	$1.44\cdot10^{-8}$	$1.17\cdot10^{-8}$	$1.47\cdot10^{-8}$	$1.77\cdot10^{-10}$
CPE2: n2	0.83	0.85	0.82	0.96
C_2 (F)	$1.43\cdot10^{-9}$	$1.49\cdot10^{-9}$	$2.21\cdot10^{-8}$	$4.25\cdot10^{-11}$
CPE3: Q_0 (Ω^{-1} s^n)	$1.20\cdot10^{-6}$	$4.85\cdot10^{-7}$	$1.92\cdot10^{-6}$	$9.16\cdot10^{-7}$
CPE3: n3	0.81	0.84	0.74	0.66

Due to the low temperature EIS measurements (-50 °C), the fitted capacities are obtained with the expected values (Fig. 4.16 and Tab. 4.4). The high frequency range semicircle at low temperature has a capacity of $1.13\cdot10^{-12}$ F. The mid frequency range semicircle has a capacity of $1.00\cdot10^{-9}$ F. Hence, the high frequency semicircle can be assigned to the grain and the mid frequency semicircle to the grain boundary.

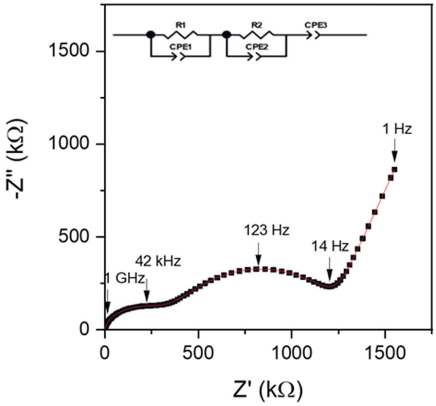

Fig. 4.16. Nyquist-plot for LLZ:Ta-annealed pellets at low temperature (-50 °C). The LLZ-Ta pellet was sintered by FAST/SPS at 675°C with 10 min dwell in Ar and under a pressure of 440 MPa. Fitting (red line) was performed with the shown equivalent circuit. R represents an ohmic resistance and CPE a constant phase element. The capacity can be calculated by Eq. 4.8 and shown in Tab. 4.4.

Tab. 4.4. Fit results of the EIS measurements for LLZ:Ta layer at -50 °C. The capacity *C* was calculated by Eq. 4.8.

Sample	**LLZ:Ta**
Sintering temperature (°C)	675
Thickness (mm)	1.54
$R1$ (Ω)	$2.907 \cdot 10^{5}$
CPE1: Q_0 (Ω^{-1} s^{n})	$3.02 \cdot 10^{-10}$
CPE1: n	0.75
$C1$ (F)	$1.13 \cdot 10^{-12}$
$R2$ (Ω)	$1.01 \cdot 10^{6}$
CPE2: Q_0 (Ω^{-1} s^{n})	$1.05 \cdot 10^{-8}$
CPE2: n2	0.67
$C3$ (F)	$1.00 \cdot 10^{-9}$

The LLZ:Ta-air and LLZ:Ta separators sintered at 750°C have comparable bulk impedance with 3002 Ω cm^{-1} and 2642 Ω cm^{-1}, respectively. Thus, the pretreatment does not alter the bulk conductivity significantly. The grain boundary resistance for the LLZ:Ta-air sample is 2407 Ω cm^{-1} and is similar to that for LLZ:Ta with 2529 Ω cm^{-1}. The resulting total conductivity is around $2 \cdot 10^{-4}$ S cm^{-1} for both types of LLZ:Ta. The rather similar grain boundary resistance of both types of LLZ:Ta proves the removal of LiOH and Li_2CO_3 layers during FAST/SPS sintering at 750°C. In contrast, the LLZ:Ta-air and LLZ:Ta pellets sintered at 675 °C show a completely different behavior (Fig. 4.15c and d). While, the LLZ:Ta pellet shows a similar total ionic conductivity of around $1 \cdot 10^{-4}$ S cm^{-1} (6.9 kΩ cm), the LLZ:Ta-air pellet exhibits only $3 \cdot 10^{-5}$ S cm^{-1} (39 kΩ cm). For LLZ:Ta-air sintered at 675 °C, it is not possible to separate the bulk from the grain boundary contribution (Fig. 4.15c). However, as the bulk impedance is similar for LLZ:Ta-air and LLZ:Ta sintered at 750 °C, the reduction in total ionic conductivity must be caused by the remaining LiOH and Li_2CO_3 layer on the LLZ:Ta-air grains. Although, the removal of LiOH and Li_2CO_3 during sintering at 750°C leads to similar total ionic conductivities as for pretreated samples, the observed formation of pores can result in structural weak points (Fig. 4.14). These might cause mechanical fracturing, and lead to capacity fading due to the volume change of LCO during de-/lithiation.

The grain boundary impedance for LLZ:Ta is comparable with its bulk impedance. For the presented FAST/SPS sintering process, the LLZ:Ta grain size has no significant impact on the total ionic conductivity. In the case the FAST/SPS process is changed i.e. lower applied pressure, the LLZ:Ta grain size might be a relevant parameter to improve the sintering process or increase the total ionic conductivity [41, 169, 170].

The ionic conductivity depends on the sintering temperature. This is shown for LLZ:Ta pellets sintered by FAST/SPS at 675 °C with 440 MPa and 1050 °C with 50 MPa (Fig. 4.17). The resulting grain size is for both pellets 10 µm and the density is 90 % (with a 2 % error bar). For higher sintering temperatures the total ionic conductivity is increased due to lower grain boundary impedance.

LLZ:Ta sintered by FAST/SPS at 1050 °C in Ar has a total ionic conductivity of 0.8 mS cm^{-1} at RT, while the LLZ:Ta sintered by FAST/SPS at 675 °C has a total ionic conductivity of 0.2 mS cm^{-1} at RT (Fig. 4.17b). The grain boundary impedance for LLZ:Ta sintered by FAST/SPS ar 1050 °C is smaller than for low temperature sintered one. As a result, the activation energy decreases from 0.61 eV to 0.45 eV (Fig. 4.17b).

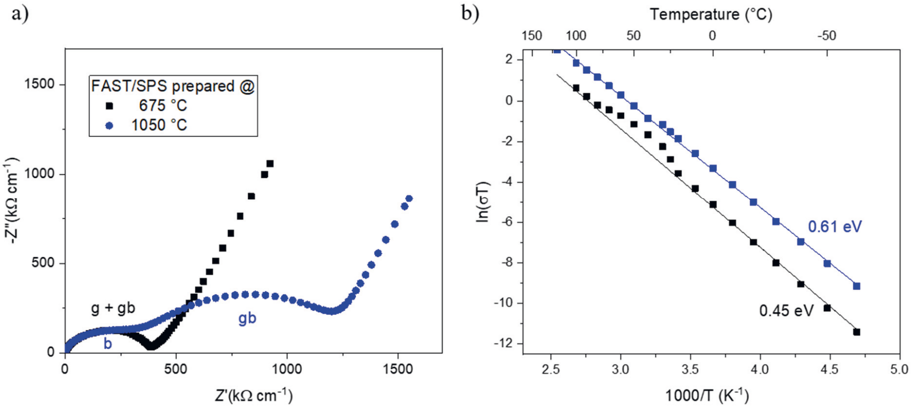

Fig. 4.17. a) EIS spectra of LLZ:Ta sintered for 10 min in and Ar) at 675 °C and 440 MPa and at 1050 °C and 50 MPa at -50 °C. b) Arrhenius plot presenting the temperature dependence of Li$^+$ conductivity of LLZ:Ta sintered by FAST/SPS.

4.1.8. Electrochemical behavior of the FAST/SPS sintered composite cathode

The LLZ:Ta (annealed in Ar atmosphere for 2 h at 750 °C) was chosen for electrochemical characterization based on the results in section 4.1.7.1. To analyze the prepared composite cathode capacity, a half-cell, consisting of a composite cathode and an LLZ:Ta layer, was mechanically attached with an In-foil on the LLZ:Ta side. The assembled ASSLBs were charged to 3.4 V vs In-Li-alloy with a constant current of 50 µA at 100 °C and afterward held at constant voltage until the current dropped to 10 µA (Fig. 4.18a). The off-set voltage was chosen to avoid a major volume change of LCO that could damage the LCO/LLZ:Ta interface [62, 179].

Typically, ASSLBs are electrochemically characterized at temperatures between 50 °C and 80 °C [18, 27, 117]. However, due to the relatively low ionic conductivity observed for the LLZ:Ta layer (section 4.1.7.2), a higher measuring temperature of 100 °C was chosen.

The first charge agrees well with the expected charge curve for LCO (Fig. 4.18a) [180-182]. A small bump in the charge curve is due to the wiring cable movement during the charge process. The initial areal capacity was 0.94 mA h cm^{-2}, representing the successful charge of nearly 72 % of the total LCO loading (106 mA h g^{-1}). This value is comparable with a similar composite cathode reported by Tsai et al. [18], and higher than for many other reported composite cathodes [23, 27]. In comparison with a pure LCO cathode, while having higher CAM loading than the composite cathode (pure: 22 mg, composite: 8 mg), the areal capacity is significantly increased (Fig. 4.18b) [25]. This indicates the successful utilization of more LCO per area due to Li-ion conductivity introduced by LLZ:Ta into the cathode. Hence, the composite cathode allows for higher thickness than the pure one, leading to higher areal capacity and energy density.

The first discharge voltage started at 3.3 V, and the discharge curve shows a steep slope, resulting in a low discharge capacity of 0.05 mA h/cm^2. This suggests only a small portion of the LCO is discharged.

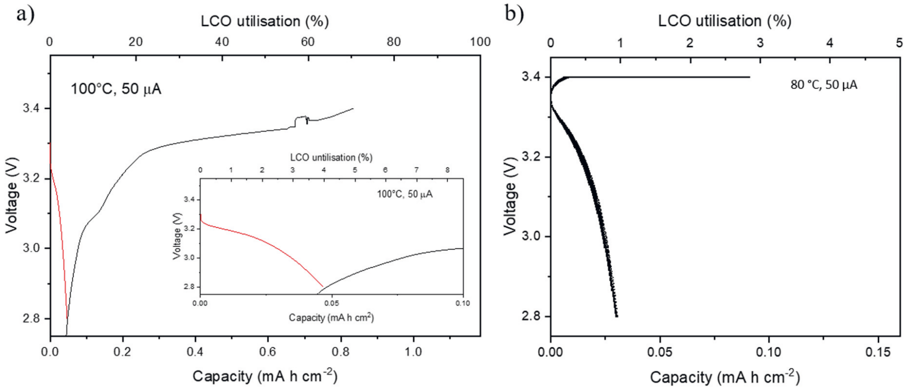

Fig. 4.18. Charge-discharge characteristics of an ASSLB with a) composite cathode (CAM loading 8 mg) and b) pure LCO cathode (CAM loading 22 mg, 5 cycles). The composite cathode was fabricated by FAST/SPS (750 °C, 440 MPa, Ar, and 10 min dwell time).

The small capacity should be caused by an increase in the total impedance of the ASSLB. The Nyquist plot in Fig. 4.20a shows the impedance spectra of the ASSLB before and after charging. Before charging, the EIS spectrum shows an intercept with the x-axis at high frequencies, one semicircle, and one diffusion tail.[5]

After charging, the EIS spectrum is changed. While the high frequency impedance is the same, at medium frequency ranges, the semicircle is more obvious to detect and has significantly increased. The total impedance of the ASSLB has nearly tripled during the first charge. The increased impedance can lead to a drop in the cell potential. The cut-off voltage would be reached without discharging the cell. An increase in impedance can be caused by loss of contact area between LCO and LLZ:Ta, or In-Li and LLZ:Ta, or by electrochemical degradation leading to Li-ion or electron blocking layers.

The ASSLB was disassembled and characterized by SEM (Fig. 4.20).

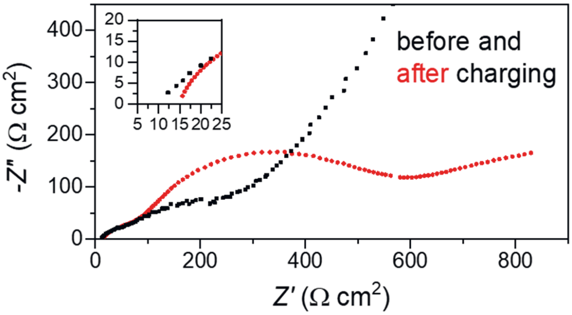

Fig. 4.19. EIS spectra of the ASSLB consisting of a half-cell (LCO/LLZ:Ta |LLZ:Ta) and a metallic In-foil as an anode at 100 °C. The black scatters present the impedance before charge and the red ones after charging.

The SEM shows major cracks within the cycled composite cathode (Fig. 4.20). As no cracks are observed in the composite cathode after FAST/SPS (Fig. 4.14), the cycling, and more precise the charging, must be responsible for the crack formation. The cracks have a length of several micrometers and seem to be preferential at the interface between LCO and LLZ:Ta. Cracks hinder charge transfer, and it can be assumed that most of the cathode regions are not accessible and no longer provide capacity to the ASSLB. As crack formation also alters the electrochemical properties, a homogenous current distribution can no longer be assumed. Due to localized higher currents, an increased degradation should occur in such areas and further increase the crack propagation.

---

[5] A detailed study on the EIS spectra is conducted in section 4.2.1.2.

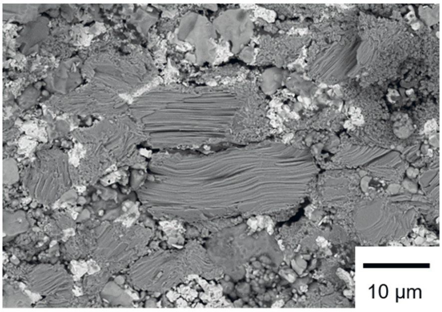

Fig. 4.20. Fracture surface SEM of a cycled composite cathode. The dark areas are LCO and the light ones LLZ:Ta. Around the LCO areas cracks are clearly visible.

The cracks can be formed by the declining volume of LCO during charge which is ascribed to be up to 4 % [62, 179]. However, a previously reported composite cathode was able to be cycled many times [18]. The difference to the here presented composite cathode is the sintering temperature at 1050 °C during conventional sintering. The higher sintering temperature can lead to stronger sinter necks, providing higher mechanical stability to the composite cathode. Additionally, the high applied mechanical pressure during FAST/SPS sintering could cause internal stress in the sample, which is prone for crack formation.

The high mechanical pressure was applied to support the sintering at low temperature 675 °C or 750 °C, Fig. 3.3b) and to prepare composite cathodes with high density and dense, high conductive LLZ:Ta layers. However, it is possible that by applying the high mechanical pressure the particles were pressed together tightly rather than appropriately sintered. An indication for that can be seen in Fig. 4.15. The grain boundary impedance of LLZ:Ta at RT is relatively high and suggests incomplete sintering for LLZ:Ta grains. Furthermore, a composite system has to be co-sintered. Here the LCO forms a rigid sintered network prior to the sintering of the LLZ:Ta (4.1.3) and can hinder the sintering of the LLZ:Ta.

In the case of constant volume during cycling as in the LLZ:Ta layer, no effect can be seen. For components with volume change as the composite cathode in which the LCO shrinks during charge, sinter necks between LCO and LLZ:Ta can be broken. Lower charge voltages or the charge with applied mechanical load can help to confirm this hypothesis. It is also possible to switch the CAM to such as NMC, NCA, or LMO as they might show an improved sintering behavior with LLZ:Ta even at lower sinter temperatures.

Otherwise, so-called zero-strain cathodes by a combination of multiple CAMs could be promising [183-185].[6] Another approach would be to add a small portion of liquid or polymer electrolyte into the composite cathode to fill the formed cracks and maintain the contact to ensure charge transfer [96, 125, 186]. Such a battery type is a “hybrid” or polymer-ceramic ASSLB. One type of a polymer-ceramic ASSLB system will be introduced in section 4.4.1.

4.1.9. Investigation of the annealed LCO/LLZ:Ta interface

4.1.9.1. Structural characterization of the annealed LCO/LLZ:Ta interface

As the FAST/SPS sintered composite cathode shows low mechanical stability during electrochemical cycling (Fig. 4.18a, and Fig. 4.20), the composite cathode was annealed at 1050 °C for 30 min in air. A detailed study of the FAST/SPS and annealed LCO/LLZ:Ta interface by TEM investigation of a composite cathode was performed. The resulting images are shown in Fig. 4.21. The TEM image of the FAST/SPS sintered composite cathode (Fig. 4.21a) shows the crystalline grains of LCO and LLZ:Ta. This is in good agreement with the XRD results (Fig. 4.7). However, between the LCO and LLZ:Ta grains, an amorphous layer with a thickness of roughly 5 nm was formed.

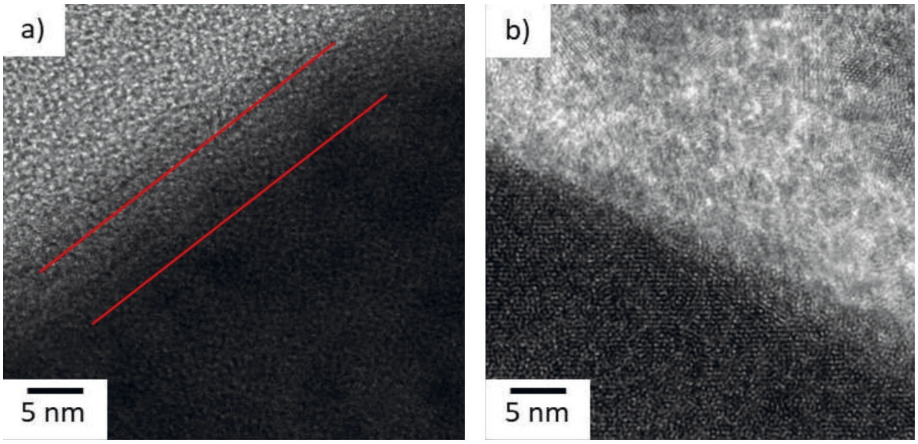

Fig. 4.21. TEM images of the interface between LCO (bright area) and LLZ:Ta (dark area): a) FAST/SPS sintered composite cathode; b) annealed composite cathode. The interface between LCO and LLZ:Ta in the composite cathode after FAST/SPS appears amorphous (marked by red lines). Post-annealing resulted in the crystallization of the amorphous interface.

---

[6] A minimum of two CAMs is used. The CAMs and their mixture is chosen in a way, that the volume changes during cycling cancel themselves out.

Amorphous interfaces are known to be detrimental for conduction processes [187, 188]. In cold sintering of solid electrolytes, amorphous interfaces are normally observed and are considered to be a reason for low total ionic conductivity. Especially, Leng et al. observed a low total ionic conductivity for cold sintered $Na_3Zr_2Si_2PO_{12}$ [188]. The application of a subsequent annealing step increased the total ionic conductivity by an order of magnitude due to the crystallization of the amorphous grain boundary layer [188]. In order to verify this hypothesis, an annealing step at 1050°C for 30 min in air was introduced for the composite cathodes and LLZ:Ta layers. This additional heat treatment crystallized the LCO/LLZ:Ta interface (Fig. 4.21b) without causing significant grain growth or side reaction. (Fig. 4.22).

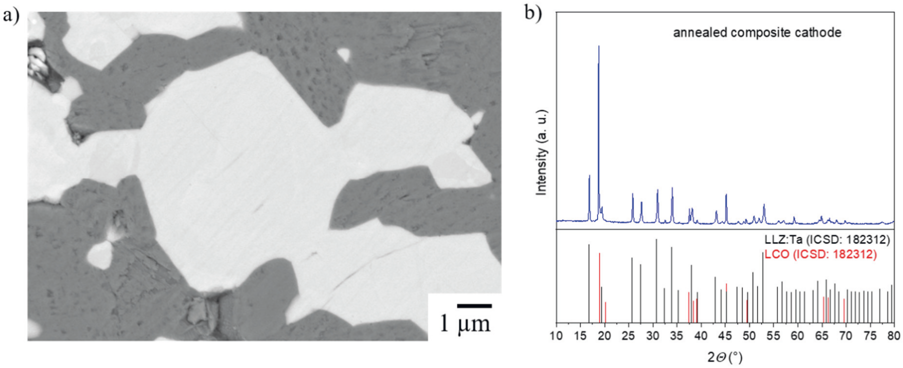

Fig. 4.22. a) Cross-sectional SEM images of an annealed LCO/LLZ:Ta composite cathode obtained with a backscattering electron detector. The sample was sintered by FAST/SPS at 750 °C and 440 MPa in Ar with 10 min dwell time and after annealing at 1050 °C in air for 30 min. The areas in bright are LLZ:Ta. The dark areas are LCO. The LCO and LLZ-annealed phases are clearly distinguishable. b) XRD pattern of the composite cathode (LCO/LLZ:Ta).

However, fingerprint methods are required to characterize the phases, such as TEM/EDX. During the annealing process elemental inter-diffusion can occur [27]. Co from LCO is known to diffuse into LLZ and Al, La, or Zr from LLZ:Ta into LCO. As a result, impurity phases such as La_2CoO_4 and others are formed [1, 3, 10, 27]. These layers show only low Li-ion conductivity and have to be avoided. Short annealing times are beneficial to avoid significant elemental cross-diffusion [17, 18].

TEM/EDX allows a detailed elemental analysis of the LCO/LLZ:Ta interface (Fig. 4.23). The measurements were performed on a bilayer of LCO and LLZ:Ta sintered by FAST/SPS and after annealing. The EDX mapping reveals that the Co is located in the LCO part. A clear edge is seen. Within the LCO area, the Co distribution is homogenous. The same is observed for La within LLZ:Ta area. The accumulation of La within the LCO area should not relate to diffusion. In the preparation process, the LLZ:Ta powder was hand-pressed, and then the LCO powder was added. During this preparation step, the powders can mix partially.

An elemental diffusion causes a gradient in elemental concentration. As no gradient is seen in the whole mapping area, the mixing of LLZ:Ta and LCO powder is the only valid explanation.

Other elements such as Zr, Ta, and Al appear to be homogenously distributed. However, the signal for Zr and Ta is low. In fact, the signal is difficult to separate from the background. The same applies for Al due to its low amount within LLZ:Ta. Owing to these elements low signal, it is not obvious to examine the extent of any possible thermal-induced diffusion during the FAST/SPS and annealing processes.

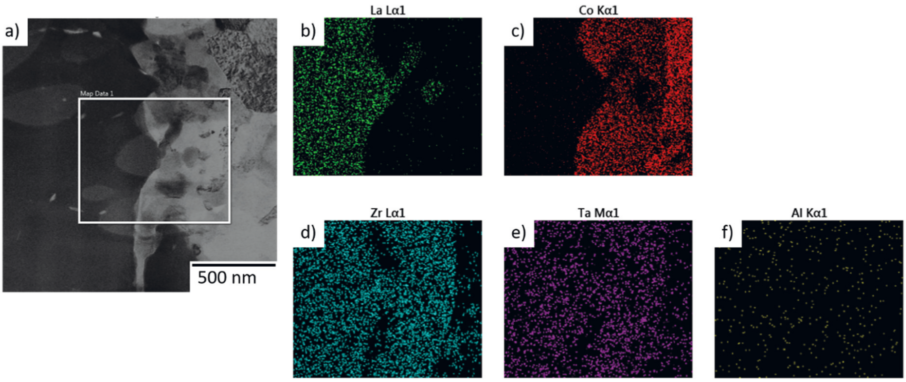

Fig. 4.23. TEM image of the interface between LCO (bright area) and LLZ:Ta (dark area) of the post-annealed composite cathode. The EDX mappings for a) La, b) Co, c) Zr, d) Ta, and e) Al are shown.

Furthermore, the sintering of LCO in Ar with LLZ:Ta and graphite foil can lead to the loss of oxygen atoms in the LCO structure [165, 189]. As a result, the LCO structure can rearrange and form so-called Low Temperature (LT)-LCO on its surface. In LT-LCO, the Co and Li atoms partially switch their position [126]. Hence, the conduction of electrons and Li-ions is hindered. Raman spectroscopic results after FAST/SPS and annealing, suggest the formation of a secondary LCO phase (Fig. 4.24 and Fig. 4.25). In a pure LCO pellet prepared by FAST/SPS, two distinct Raman spectra are visible (Fig. 4.24). Both spectra show a peak at 487 cm^{-1} and 596 cm^{-1}, representing the stretching (E_g) and rotational vibration (A_{1g}) of LCO. However, the intensity ratio is different. For one of the spectrum, the ratio matches with pristine rhombohedral HT-LCO ($R\bar{3}m$). The other one has the same intensities for both peaks. According to Porthault et al., this might suggest formation of a cubic oxygen-deficient LT-LCO ($Fd\bar{3}m$) phase [86, 189, 190]. As other peaks are absent, it can be assumed that the LT-

LCO phase is less than 10 % of the LCO phase [190]. Of course, the composition of the second phase could also be different, but the possible phases would show more than the two visible peaks [143, 189-191].

The formation of LT-LCO at the LCO/LLZ:Ta interface can result in low ionic conductivity at the interface and high interfacial impedance. The observed amorphous layer might not be the only reason for the high impedance of the FAST/SPS prepared ASSLB (Fig. 4.20a).

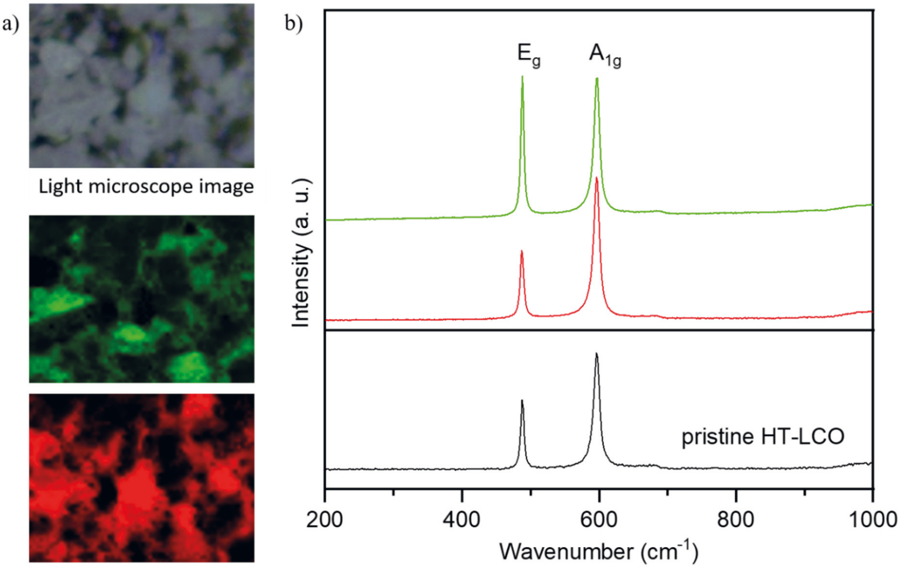

Fig. 4.24. a) Light microscope image of the LCO after FAST/SPS and the intensity mapping for two distinct LCO phases. In b) exemplarily, an associated Raman spectrum is shown in green and red. The pristine LCO spectrum is shown in black. The red Raman spectrum matches well with the pristine LCO spectra, while the green Raman spectrum has a different peak ratio.

The LT-LCO can be transformed back into LCO by annealing in atmospheres containing oxygen [189]. The hypothesized reaction pathway is that parts of the Li in the LCO structure react with O_2 to form Li_2O. At a temperature above 300 °C, Li_2O can be reinserted into the LT-LCO structure to transform into the HT-LCO [189].

The annealing process can lead, to a more crystalline interface and to a transformation of LT-LCO into HT-LCO. However, the Raman spectra of the annealed LCO pellet still show the identical two spectra of LCO as after the FAST/SPS process (Fig. 4.25). The quantification of the two phases, however, is difficult. Above 90 % HT-LCO, the additional Raman peaks of the LT-LCO are absent, and the intensity ratio can only indicate a second phase. However, the intensity mapping of the HT-LCO phase has increased compared to the FAST/SPS sintered one (Fig. 4.25 and Fig. 4.24). This suggests that the annealing is beneficial for retrieving the desired HT-LCO phase.

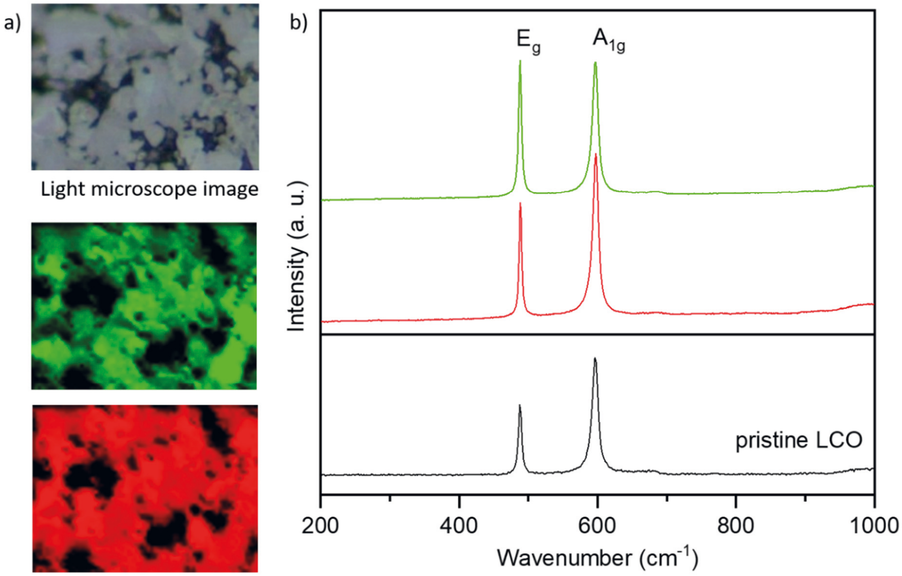

Fig. 4.25. a) Light microscope image of the LCO after annealing and the intensity mapping for two distinct phases. In b) exemplarily, an associated Raman spectrum is shown in green and red. The pristine LCO spectrum is shown in black. The red Raman spectrum matches well with the pristine LCO spectrum, while the green Raman spectra has a different peak ratio.

4.1.9.2. Electrochemical properties after annealing

To evaluate the effect of the post-annealing on total cell resistance, two half-cells were prepared with LLZ:Ta powder. One of them was post-annealed at 1050°C before assembling them into an ASSLB. Both ASSLBs (FAST/SPS sintered, and FAST/SPS and post-annealed) were charged to 3.4 V vs In-Li (4 V vs Li/Li$^+$), and EIS measurements were performed (Fig. 4.26).

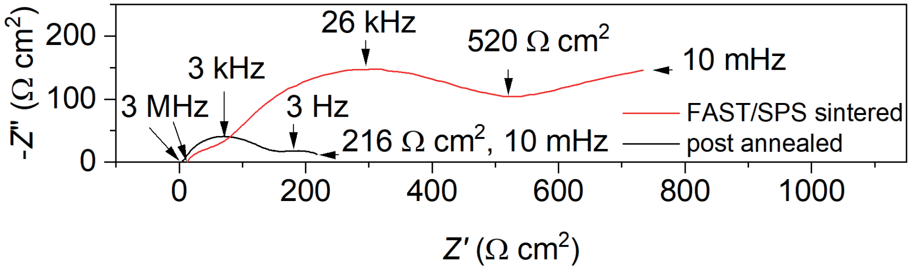

Fig. 4.26. EIS spectra of ASSLBs consisting of LCO/LLZ:Ta|LLZ:Ta|In-Li at 80 °C. The ASSLBs were charged to 3.4 V vs In-Li at 50 µA cm^{-2} beforehand. The composite cathode was used after FAST/SPS sintering (red line) and with post-annealing at 1050 °C for 30 min in the air (black line), respectively.

For the FAST/SPS sintered ASSLB, two depressed semicircles are observed. In the post-annealed ASSLB, two smaller semicircles are observed. While for the FAST/SPS sintered sample, the high frequency semicircle is smaller, this is switched after post-annealing. This can be a result of the different overlap of grain, grain boundary, and interfaces between cathode/LLZ-air and anode/LLZ:Ta (discussed in detail in section 4.2.1.2).

The total impedance of the ASSLB is estimated from the end of the second semicircle at low frequencies. The FAST/SPS sintered ASSLB has an areal resistance of 520 Ω cm^2 and the post-annealed ASSLB only 216 Ω cm^2. Thus, the total cell resistance of ASSLB can be reduced by a post-annealing step. The microstructure and phase of the composite cathode were unaltered after post-annealing (Fig. 4.22a). Therefore, the reduction of total cell resistance is apparently a result of the higher crystallinity of boundary between LCO and LLZ:Ta grains.

4.1.9.3. Effect of LLZ:Ta pretreatment on electrochemical performance

The impact of LLZ surface impurities on the electrochemical performance of ASSLBs was verified by electrochemical cycling (see also section 4.1.7). Two cells were manufactured using LLZ:Ta-air or LLZ:Ta powder. Both ASSLBs were post-annealed to ensure a low LCO/LLZ:Ta interface impedance.

The charge/discharge curves of the ASSLBs are shown in Fig. 4.27. The ASSLB was charged only to 3.4 V (4.0 V vs Li/Li$^+$) to minimize the volume change of LCO during cycling to limit the risk of mechanical degradation, as described in Fig. 4.20b and the literature [62, 192]. The first charge for both ASSLBs is similar and shows the typical behavior of LCO. The LCO utilization of the first charge is for the ASSLB with LLZ:Ta-air is 81 mAh g^{-1} or 1.3 mAh cm^{-2} and LLZ:Ta is 94 mAh g^{-1} or 1.5 mAh cm^{-2}. The high areal capacities for the composite cathodes, compared to pure LCO cathodes (see also Fig. 4.18), is a result of the higher LCO utilization [25].

The discharge significantly varies between LLZ:Ta-air and LLZ:Ta. For the ASSLB prepared with LLZ:Ta-air, the first discharge is untypical for LCO and has only a capacity of 0.2 mAh cm^{-2} as compared to the LLZ:Ta ASSLB of 1.2 mAh cm^{-2}. This is also seen by the LCO utilization of 14 mAh g^{-1} for the LLZ:Ta-air ASSLB and 75 mAh g^{-1} for the LLZ:Ta ASSLB. The low coulombic efficiency indicates a significant degradation of the composite cathode already after the first charge.

The low coulombic efficiency can result from the high polarization and total impedance of the composite cathode. The high impedance can originate from: i) unfavourable chemical composition of the interfaces due to the presence of surface impurities; ii) incomplete sintering of the LCO and LLZ:Ta powders e.g. due to presence of surface impurities; iii) presence of micro-pores and micro-cracks between the LCO and LLZ:Ta phases caused by the decomposition of surface impurities. Micro-pores and micro-cracks can lower the mechanical stability of composite cathodes and cause the loss of LCO/LLZ:Ta interface area during the charging due to the volume change of LCO. Hence the ASSLB can provide high charge capacity but as the LCO/LLZ:Ta interface is damaged, most of the LCO should no longer be utilizable in discharge.

In the ASSLB with LLZ:Ta, the charge and discharge profile maintain the typical LCO behavior over the first cycles. However, the hysteresis between the potential plateaus for charge and discharge gradually increases in each subsequent cycle and continuously reduces the capacity.

As the LLZ:Ta pretreatment is different, while the ASSLBs are otherwise same, it is reasonable to expect that the surface impurities have to be responsible for the very low capacity in the ASSLB with LLZ:Ta-air for the first discharge. The surface impurities can lead to the formation of pores around LLZ:Ta grains due to the removal of the LiOH and Li_2CO_3 layer (Fig. 4.14). The formed pores can cause mechanical weak spots that are prone to crack propagation during de-/lithiation of LCO, due to a volume change by approximately 4 % [62, 179]. Therefore, capacity fading caused by mechanical fracturing, as already discussed in section 4.1.8 or by Tsai et al. for a similar ASSLB, is most probable [18]. For the ASSLB fabricated with LLZ:Ta the crack formation should be reduced as the number of micro-pores is lower as the LiOH and Li_2CO_3 layer were removed prior to sintering (Fig. 4.14). In conclusion, this shows the importance of controlling the surface purity of initial LLZ:Ta powders, as it significantly affects the electrochemical performance and electrochemical cycling stability of ASSLBs.

The drop in first discharge voltage in the LLZ:Ta containing composite cathode could also be related to the incomplete charge of the LCO that leads to concentration polarization and a drop in the first discharge voltage. In a fully charged ASSLB, this behavior is not observed (Fig. 4.29).

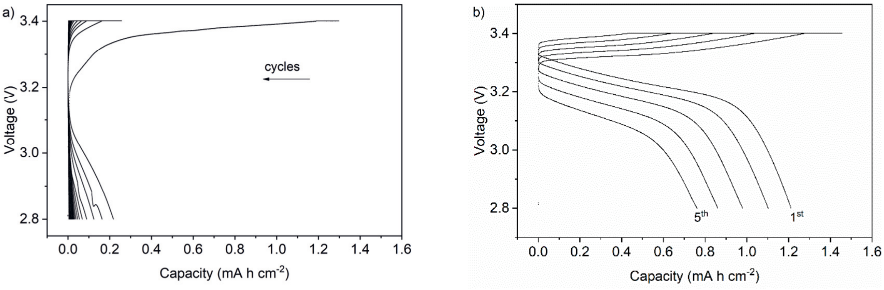

Fig. 4.27. Charge-discharge characteristics of ASSLB (LCO/LLZ:Ta|LLZ:Ta|In-Li) at 80 °C after post-treatment at 1050 °C and with a charge and discharge current density of 50 µA cm^{-2}. a) LLZ:Ta powder stored in air (LLZ:Ta-air), containing surface impurities was used. b) The impurities were removed by annealing in Ar (LLZ:Ta).

4.1.10. Conclusion of the manufacturing part

The developed FAST/SPS process can be used to prepare fully inorganic ASSLB featuring a composite LCO/LLZ:Ta cathode and LLZ:Ta separator layer. Sintering aids are unnecessary. The composite cathodes can provide a high areal discharge capacity of up to 1.2 mAh cm^{-2} but the electrochemical cycling stability is optimizable (Fig. 4.27).

With the high-pressure assisted FAST/SPS process, the sintering temperature and time can be significantly reduced to 750°C or even to 675 °C for 10 min (Fig. 4.7) in comparison to conventional sintering that requires more than 1050 °C for hours [14, 29]. Thereby, the relative density is at least 90 % (Tab. 4.2), and the ionic conductivity at RT (0.4 mS cm^{-1}, Fig. 4.15) is acceptable.

However, it was shown that the sintering temperature has to be higher than the decomposition temperature of Li_2CO_3 (Fig. 4.15). As the removal during the process can lead to pore formation and low cycle stability (Fig. 4.14), it is advisable to remove the Li_2CO_3 prior to the sintering.

The FAST/SPS sintered LCO/LLZ:Ta interface is amorphous and shows high impedance (Fig. 4.21). The LCO/LLZ:Ta interface can be crystallized by applying a subsequent annealing process to achieve low impedance (Fig. 4.20). No significant elemental inter-diffusion was observed after FAST/SPS and annealing (Fig. 4.22).

This shows the challenge for processing is to find parameters that lead to high density and interfaces with low impedances.

The low sintering temperatures of the FAST/SPS process open the opportunity of co-sintering of CAM with low thermal stability such as MNO or NMC but the subsequent annealing step to reduce the CAM/LLZ:Ta interface impedance would destroy any other CAM (see Fig. 4.4). However, FAST/SPS can be used to prepare such CAM/LLZ interfaces and the analysis of the interface impedance could show if for the used CAM an annealing step is required.

4.2. Characterization of the degradation process

4.2.1. Characterization of the cycled composite cathodes

4.2.1.1. Various types of cathodes for all-solid-state Lithium batteries

The developed FAST/SPS process allows the fabrication of dense components for ASSLB such as, a dense LLZ:Ta separator layer, a dense dual phase LCO/LLZ:Ta composite cathode, and an integrated cathode half-cell consisting of a cathode layer, as well as an LLZ separator layer at temperatures as low as 675 °C. Two types of integrated cathode based half-cells were manufactured to study, in detail, the degradation mechanisms of ASSLB. The reference cell is a plain bilayer system of pure LCO as cathode and LLZ:Ta as separator (further referenced as "LCO/LLZ:Ta plain", Fig. 4.28a). The composite half-cells (further assigned as "LCO/LLZ:Ta composite") were prepared using a mixture of LCO and LLZ:Ta to form a dense dual LCO/LLZ:Ta composite cathode layer (Fig. 4.28b). The thickness and LCO loading were controlled by sand polishing the composite cathode after the preparation. An In foil was attached to the half-cells to act as an anode (schematically depicted in Fig. 4.28).

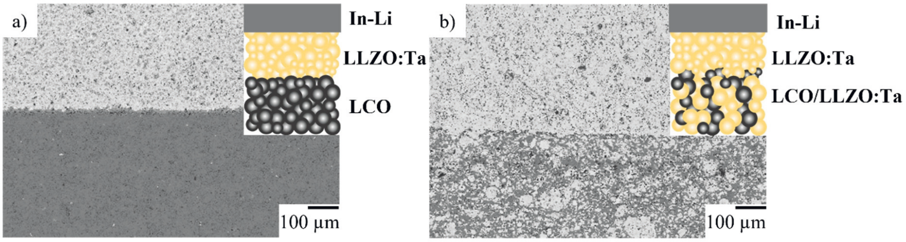

Fig. 4.28. Cross sectional SEM images and below their schematic overview of different integrated solid electrolyte/cathode configurations prepared in this work: the plain bilayer LCO/LLZ:Ta electrodes (a) and the LCO/LLZ:Ta composite cathode layers (b). In the SEM images dark colored areas are LCO and light ones LLZ:Ta.

4.2.1.2. Electrochemical characterization of composite cathodes

The ASSLB full cells with pure and composite cathodes (In-Li|LLZ:Ta|LCO/LLZ:Ta) were electrochemically characterized by CC-CV charge and CC discharge between 2.8 – 3.6 V vs In-Li (4.2 V vs Li/Li$^+$) at 80 °C (Fig. 4.29 and Fig. 4.30). The composite cathode with a thickness of 35 µm provides an initial areal capacity of 1.15 mAh cm^{-2} or 115 mAh g^{-1} (Fig. 4.29a). For the first discharge, 0.9 mAh cm^{-2} (corresponding to 90 mAh g^{-1} specific capacity) is obtained. It is typical for LIBs and garnet-based ASSLB to have a roughly 10 – 20 % higher first charge capacity than in the first discharge. Hence, only a low initial coulombic efficiency of 78 % is obtained, that increases rapidly to around 97 % within

15 cycles. After around 45 cycles the capacity stabilizes around 0.3 mAh cm^{-2}. The more stable first discharge voltage in comparison to Fig. 4.27 can be a result of the LLZ:Ta layer. Here also, the LLZ:Ta powder for the LLZ:Ta separator was annealed in Ar.

For garnet-based composite cathodes, this capacity appears to be kind of a threshold value, as the same observation was made for an ink-based approach (Fig. 4.30a) and by Tsai et al [18]. For a plain LCO-cathode the areal capacity is around 0.03 mAh cm^{-2} (Fig. 4.30b) and confirms the need for composite cathodes to obtain high areal capacity [25, 113].

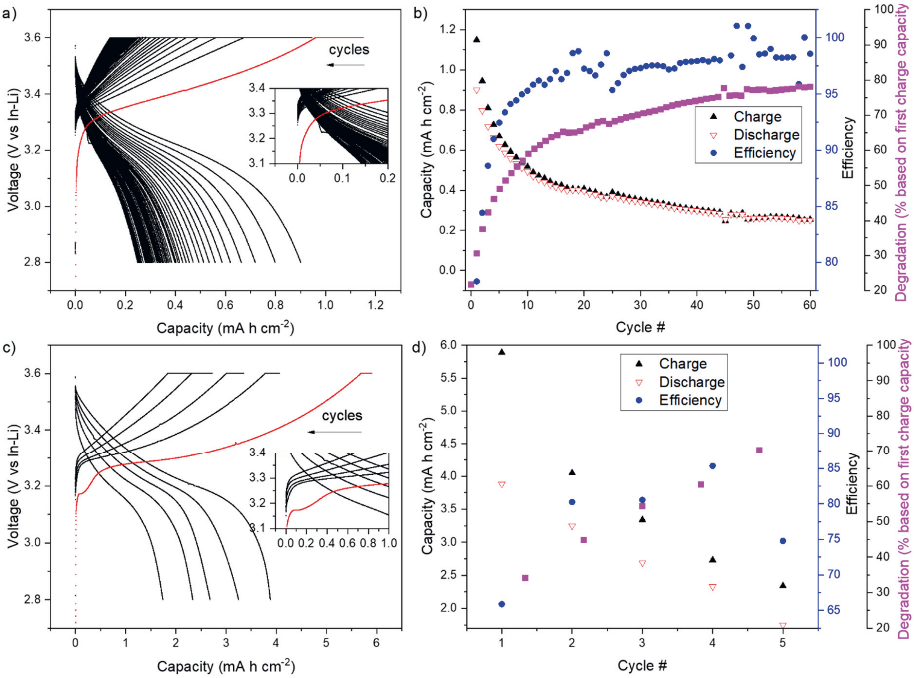

Fig. 4.29. (a,c) Charge/discharge curves and (b,d) respective charge/discharge capacity values and the coulombic efficiencies for ASSLB with (a,b) a thin composite cathode (35 µm) and (c,d) a thick composite cathode (170 µm). The first charge is marked by red (a,c). The degradation is calculated based on the first charge capacity.

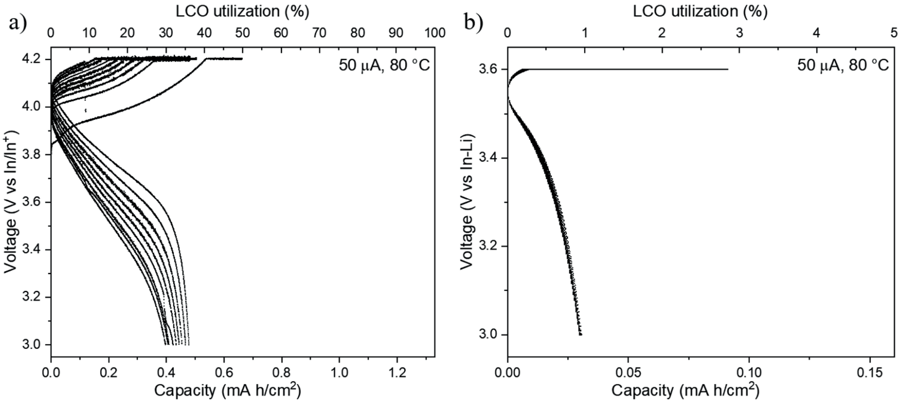

Fig. 4.30. Electrochemical cycling of an ASSLB with a) an ink-based composite cathode and b) a plain LCO-cathode. The ink-based cathode was measured vs a Li anode.

In composite cathodes exceeding a thickness of 50 μm, an Li concentration gradient can be formed due to slow charge propagation caused by relatively low ionic and electronic conductivity [25]. Therefore, and based on the report by Otoyama et al. that shows an inhomogeneous SoC in a solid-state LCO/Li_2S–P_2S_5 composite cathode [132], it is most likely that the SoC of the composite cathodes differ through the layer thickness for the electrochemically charged/discharged composite cathode.

By increasing the thickness of the composite cathode, the areal capacity of the cell is increased. Fig. 4.29b shows the cycling of the thicker composite cathode (170 μm) with similar morphology. The first charge capacity is 6 mAh cm^{-2}, corresponding to the LCO utilization of 116 mAh g^{-1}. A small part of this capacity, around 0.12 mAh cm^{-2}, corresponding to about 2 % of total charge capacity is from a process taking place at potentials between 3.15 V and 3.25 V observed as a plateau in the first charging step. During following charges, the plateau is not observed which suggests an irreversible electrochemical reaction. In thin composite cathodes, this irreversible reaction is easy to overlook as it is indicated only by a small shoulder (Fig. 4.29c).

In the first discharge itself, the cell shows a large capacity loss of nearly 2 mAh cm^{-2} (Fig. 4.29c). The discharge capacity is 4 mAh cm^{-2}, corresponding to the specific capacity of 78 mAh g^{-1} (Fig. 4.29d). The initial coulombic efficiency of thick composite cathodes is lower than that of the thin ones, as here, only 66 % is achieved. Within the first four cycles, the coulombic efficiency increases to 85 %. The fifth cycle, however, shows a slightly lower coulombic efficiency of 75 %.

The EIS plots for both plain and composite cathodes show a semicircle in the high frequency range, attributed to the total resistance (sum of bulk (R_b) and grain boundary (R_{gb}) resistances) of the solid electrolyte, and a stretched semicircle in the mid- to low frequency range (Fig. 4.31a and b). The latter semicircle in ASSLBs is typically interpreted as a superposition of individual impedances of the anode and cathode. The low frequencies contribution to the LLZ:Ta/In-Li impedance [29]. The equivalent circuit used for the fitting of the EIS spectra is shown in Fig. 4.31c.

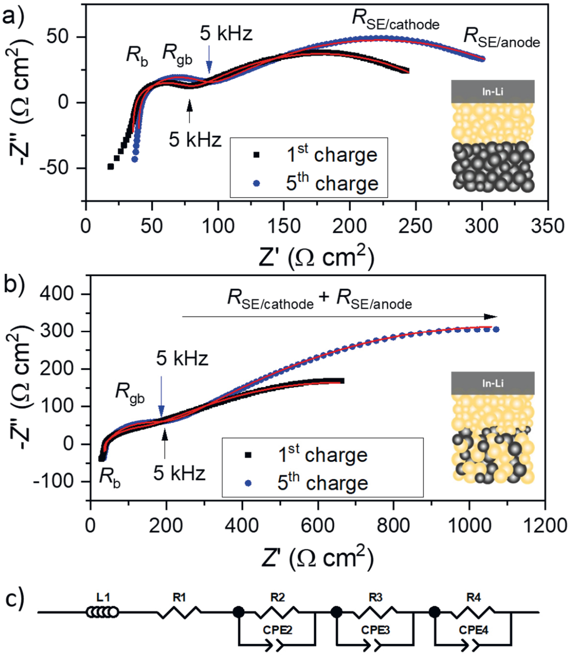

Fig. 4.31. Nyquist plot of ASSLB after the first and fifth charge of the thick composite cathode (170 µm, Fig. 4.29a) at 80 °C. The ASSLBs consists of: a) an LCO-LLZ layered structure and b) a composite cathode. The equivalent circuit for the fitting is provided in c) with L as inductance, R as ohmic resistance, and CPE as constant phase element. The high frequency inductance is caused by the wiring.

In order to assign the semicircles, first a pure LLZ:Ta layer was measured by EIS (Fig. 4.32). It has an inductance and an intercept with the x-axis at 22 Ω cm^2, one semicircle in the high to medium frequency range (3 MHz – 5 kHz), and a diffusion tail at low frequency range. The inductance is caused by the wiring and the intercept with the x-axis is in general accepted to represent the bulk conductivity. Therefore, the semicircle has to represent the grain boundary contribution. The tail can be explained with Li-ion diffusion in the sputter coated Au layer on both sides of the LLZ:Ta acting as current collectors. The value for the grain boundary resistance of 67 Ω cm^2 was fitted with the equivalent circuit in Fig. 4.32. Both, the bulk (22 Ω cm^2) and grain boundary resistance (67 Ω cm^2) are low and, therefore, a high ionic conductivity of 1.5 mS cm^{-1} at 80 °C is obtained.

For "LCO/LLZ:Ta plain" cells (Fig. 4.31a), the impedance of the solid electrolyte is observed in the high frequency range above 5 kHz. A bulk resistance of 33 Ω cm^2, and grain boundary resistance of 44 Ω cm^2 is determined after the first charge. These values are similar to the impedance of individual LLZ:Ta separator layers showing a bulk resistance of 40 Ω cm^2 and a grain boundary resistance of 60 Ω cm^2 (Fig. 4.32).

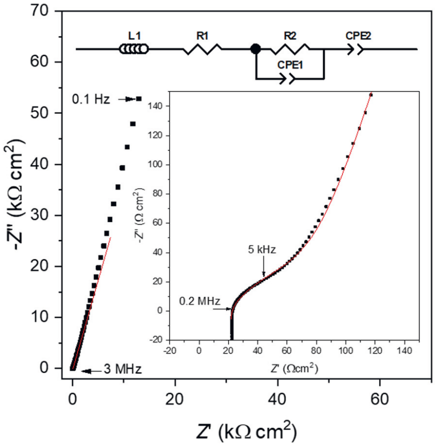

Fig. 4.32. EIS spectra of LLZ:Ta separator at 80 °C. The equivalent circuit used for the fitting is shown (L: inductance, R: ohmic resistance, and CPE: constant phase element).

After the fifth charge the LLZ:Ta impedance in the "LCO/LLZ:Ta plain" cell is slightly increased. While the nearly constant bulk impedance implies the stability of the LLZ:Ta grains, the grain boundary contribution is slightly increased to 47 Ω cm^2 after the fifth cycle. A possible explanation of this effect is provided in section 4.2.1.5.

Since the "LCO/LLZ:Ta plain" cell has geometrically well-defined interfaces, the impedance of the cathode and anode can be approximated with a good accuracy by the interfacial impedance of the respective electrodes. Fitting of the stretched semicircle in the frequency range from 5 kHz to 100 mHz results in 195 Ω cm^2 for the LCO/LLZ:Ta impedance after the first charge, which increases to 260 Ω cm^2 after the fifth charge. Compared to the LCO/LLZ:Ta interface, the impedance of the LLZ:Ta/In-Li interface is much lower with only 25 Ω cm^2 after the first charge. This anode impedance decreases even further after the cycling, reaching 15 Ω cm^2 after the fifth charge, which means that the contact between LLZ:Ta and In improves with cycling. The obtained initial values are in agreement with the interfacial impedance of

LLZ:Ta/LCO (around 170 Ω cm^2 at RT) and LLZ:Ta/In-Li (25 – 28 Ω cm^2 at RT) reported in literature [29]. As a consequence, based on the result of the "LCO/LLZ:Ta plain" cell, the increase in cell impedance observed after electrochemical cycling is attributed to the LCO/LLZ:Ta interface.

The Nyquist plots of the "LCO/LLZ:Ta composite" cell is qualitatively similar in comparison to the "LCO/LLZ:Ta plain" cell, but has a higher total impedance (Fig. 4.31b). The absolute values for the bulk and grain boundary resistance are 35 Ω cm^2 and 79 Ω cm^2, respectively. While the values are slightly higher than for the "LCO/LLZ:Ta plain" cell, they are still within the expected range. However, even more relevant is the fact that the bulk LLZ:Ta impedance remains constant with cycling, while the grain boundary impedances increase from 79 Ω cm^2 to 112 Ω cm^2 after the fifth cycle. Similar to the "LCO/LLZ:Ta plain" cell the majority of the total impedance increase is due to the impedance of the cathode and anode, which increases by over 70% from initial 1081 Ω cm^2 to 1854 Ω cm^2 within five cycles. As the principal configuration of both cells, "LCO/LLZ:Ta plain" and "LCO/LLZ:Ta composite", is same, the respective interfacial impedance value for the anode has been used to fit the anode impedance in the cell with the composite cathode as well.

As for the "LCO/LLZ:Ta plain" cell, the increase in total impedance of the "LCO/LLZ:Ta" composite" cell is caused predominantly by the increased impedance of the LCO/LLZ:Ta interface. This can be considered as the first validation of the proposed interfacial degradation mechanism based on the increasing LCO/LLZ:Ta interface impedance.

As shown in Fig. 4.29 by electrochemical measurements, the cell capacities fade continuously with electrochemical cycling. With regard to the EIS measurements, the increasing LCO/LLZ:Ta interface impedance was observed to be responsible. The increasing LCO/LLZ:Ta impedance can be either due to mechanical failure or from electrochemical degradation as schematically depicted in Fig. 2.15 (discussed in detail in section 2.4.4).

The processing-induced degradation with formation of the high impedance secondary phases is one of the most common explanations of the generally high impedance of all-solid-state ceramic cathodes (Fig. 2.15a). The literature demonstrates that the thermodynamic stability of individual materials at high temperature significantly decreases when they are brought in contact [15, 16, 193]. In the first charge, an irreversible process at 3.15 - 3.25 V, which corresponds to about 2 % of total charge capacity (Fig. 4.29a) indicates the possible formation of secondary phases during the manufacturing of the composite cathodes. Rietveld refinement confirmed the formation ca. 2 wt-% of CoO and $La_2Li_{1-x}Co_xO_4$ of a processing-induced secondary phase (Tab. 4.1) [53]. The oxidation potential of these phases, reported by Park et al., match well with the potential of the first irreversible discharge process observed for the composite cathodes (Fig. 4.29) [27].

4.2.1.3. Microstructural characterization of composite cathodes

Microstructural analysis by SEM (Fig. 4.14) and TEM (Fig. 4.21) of the “as prepared” composite cathode (FAST/SPS sintered and annealed at 1050 °C for 30 min in air) demonstrate that most of the LCO/LLZ:Ta interface is chemically clean without any formation of reaction zones after the processing.

Based on the combined information of different experimental methods, it can be concluded that the reaction products might form a few separated domains, but not continuous interfacial layers (Fig. 4.33a). Hence, even in case some small amounts of processing-induced secondary phases are present in the composite cathode, their impact on the electrochemical properties should be insignificant. Although, the secondary phases contribute a small fraction of the total capacity in the first charge, the following continuous fading of electrochemical performance by lower capacities and higher impedances, require an additional explanation.

One of the most popular explanations of capacity fading in rigid composite cathodes, that is accepted in the literature [3, 153, 194], is the mechanical degradation due to volume changes of the CAM during charge/discharge. For a similar composite cathode but with a high degree of porosity, the formation of cracks has been observed [18, 195]. Thus, the formation of a few micrometer large cracks between the LCO and LLZ grains as well as intra-granular fracturing of LCO grains after cycling of LCO/LLZ:Ta co-sintered composite cathodes with about 20 % porosity, was visualized [18].

The dense composite cathode has the same morphological state after electrochemical cycling (Fig. 4.33). The cross-sectional SEM image of the “as prepared” composite cathode is very dense and only a few dark spots indicating pores are observed (Fig. 4.33a). Based on the image analysis, the cathode density can be assumed to be around 92 %, which is supported by the relative density measurement (Tab. 4.2). The image confirms that LCO and LLZ:Ta grains are distributed homogenously throughout the composite cathode. Furthermore, the interface between the grains is sharp and appears well-sintered, without any visible formation of reaction zones or micro-cracks.

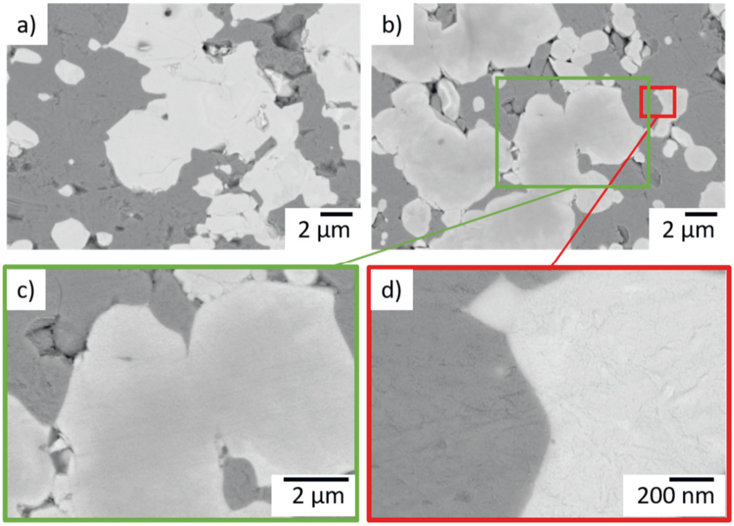

Fig. 4.33. Cross-section SEM images of the LCO/LLZ composite cathode before (a) and after cycling (b). The bright areas correspond to LLZ, the dark ones to LCO; the pores are black. The higher resolution image (c) of the cycled electrode indicates the formation of bright rims on LLZ grains in contact with LCO after cycling, while another high resolution image (d) of the same cathode demonstrates that the LCO/LLZ interface remains mechanically intact after the cycling.

Reports about LCO/LLZ:Ta composite cathodes of this density and purity without the use of sintering aids were not found. The morphology found in the electrochemical cycled composite cathode is same as in the "as prepared" one and appears mechanically intact (Fig. 4.33). In contrast to the porous composite cathodes [18], no macro- or micro-cracks are observed for the electrochemically cycled dense composite cathodes. The high density and homogenous microstructure via FAST/SPS fabrication appears to be beneficial for the mechanical stability of ceramic composite cathodes during electrochemical cycling. In addition, the formation of nano-sized cracks (below the resolution limit of SEM) is excluded, as the TEM image of the electrochemical cycled composite cathode is free of any cracks at the interface (Fig. 4.34). Furthermore, it is unlikely that a TEM lamella can be prepared from a mechanically damaged composite cathode. In conclusion, the mechanical failure of the LCO/LLZ:Ta interface is unlikely to be responsible for the loss of more than 60 % of the initial capacity, as this would mean that a similar amount of interface would be cracked, which is not observed by SEM (Fig. 4.33b to d and Fig. 4.34).

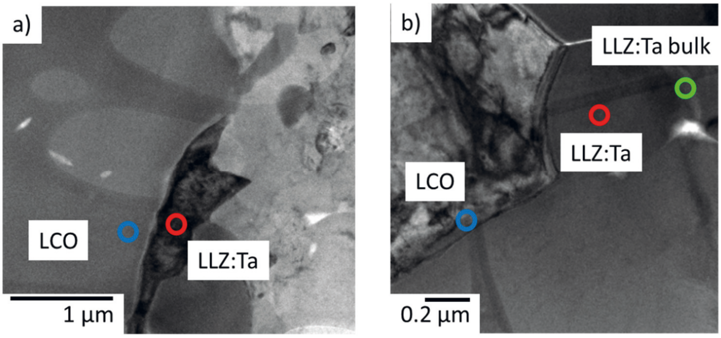

Fig. 4.34. TEM lamellas of the a) uncycled and b) electrochemical cycled LCO/LLZ:Ta interface. The markings are the areas of SAED (blue: LCO, green: LLZ:Ta interface, and red: LLZ:Ta) shown in (Fig. 4.38).

A possible explanation for the increased mechanical stability in the dense composite cathode, in comparison to the free sintered porous cathodes, can be the different stress distribution caused by the volume expansion of LCO (up to 0.3 Å expansion along the *c*-axes for $x \leq 0.5$) [59]. In porous composite cathode structures, the induced stress is inhomogeneous and can result in stress peaks around pores, causing locally high stress levels up to 2 GPa depending on the orientation of the LCO that lead to fracturing [196]. During delithiation the stresses in LCO are compressive and during lithiation tensile. For the LLZ:Ta the vice versa is observed. According to Mücke et al. the stresses depend on the orientation of the LCO grains within a LCO/LLZ composite cathode as the LCO has anisotropic volume changes which is highest in *z*-direction [196]. For future composite cathode it might be advisable to check the impact of the LCO grain orientation in more detail. In addition, Mücke et al. suggest that the stress levels in a composite cathode are highest in close proximity to pores. Hence, a porous LCO/LLZ composite cathode is prone to interface fracturing [196]. In contrast, in dense structures the stress distribution is more homogeneous, and the structure withstands the stresses caused by anisotropic LCO expansion/contraction. This demonstrates that dense composite cathodes with rigid interfaces are mechanically stable during electrochemical cycling. Since reports of other dense LCO/LLZ:Ta composite cathodes have not been found, this can be considered as the first demonstration of an all-solid-state cathode with rigid interfaces that is mechanically stable during electrochemical cycling. The high density of the composite cathode obtained by the FAST/SPS processing is most likely responsible for the mechanical stability, and clearly highlights the relevance of controlling the microstructure and density of the all-solid-state cathode. However, this observation makes it clear that the observed degradation of electrochemical performance has to be linked with another process besides the fracturing of the LCO/LLZ:Ta interface in the case of sufficient mechanical stability.

Although, mechanical degradation is not observed in the cycled composite cathode, SEM (Fig. 4.33), TEM (Fig. 4.37), and XRD (Fig. 4.40) analysis clearly point to a change in the phase composition of the composite cathodes after electrochemical cycling.

As the electrochemical processes start in the composite close to the separator [25], these regions of the composite cathode show more evident changes. SEM images of the composite cathode reveal that the contrast of the LLZ grains changes after electrochemical cycling and that LLZ grains, which have a uniform bright contrast after fabrication, show bright rims of around 0.5 μm thickness at the interface with LCO after electrochemical cycling (Fig. 4.33b and c).

EDX analysis of these rims reveals the presence of Co, which is found only after electrochemical cycling; no Co was found in the bulk of the LLZ:Ta grains (Fig. 4.35). It should be mentioned that no traces of Co were detected in LLZ:Ta (also in the areas close to the LCO) in the "as prepared" composite cathode (Fig. 4.35).

Correspondingly, some Al is detected within the LCO after electrochemical cycling, while the LCO in the "as prepared" composite cathode is Al-free (Fig. 4.36). Thus, an Al↔Co exchange between LCO ($LiCoO_2$) and LLZ:Ta ($Li_{6.45}Al_{0.05}La_3Zr_{1.6}Ta_{0.4}O_{12}$) phases during electrochemical cycling is likely and the increased average atomic number of Co-substituted LLZ:Ta in the vicinity of the LCO/LLZ:Ta interface leads to a brighter contrast in SEM (Fig. 4.33b and c).

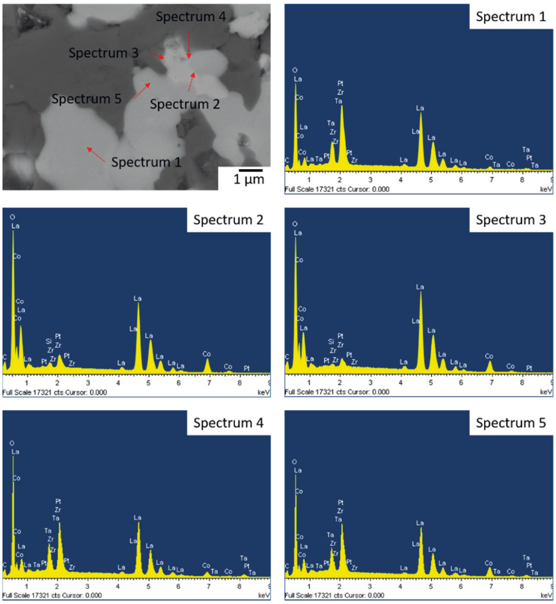

Fig. 4.35. EDX measurements in LLZ:Ta after cycling. The EDX clearly shows that Co is only present in parts of the LLZ:Ta. Therefore, the Co diffusion into the LLZ:Ta can be assumed to be a result of the electrochemical cycling. As the samples were coated with a thin Pt layer before analysis, all show a signal for Pt.

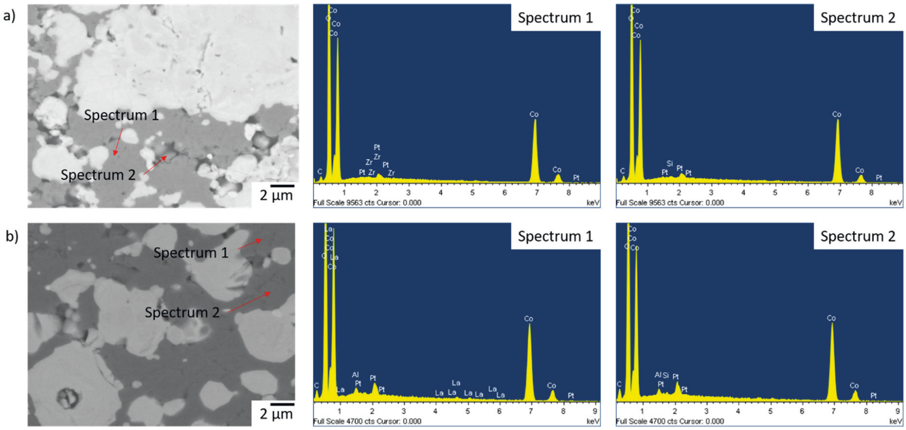

Fig. 4.36. EDX measurements in LCO before (a) and after cycling (b). The EDX clearly shows that Al can only be found after cycling within the LCO. As the samples were coated with a thin Pt layer before analysis, all show a signal for Pt.

This observation is supported by high resolution TEM analysis of the LCO/LLZ:Ta interface (Fig. 4.37). Before cycling both phases, LCO and LLZ:Ta, are crystalline in the vicinity of the interface, and the interface between them is very sharp at the atomic level (Fig. 4.37a).

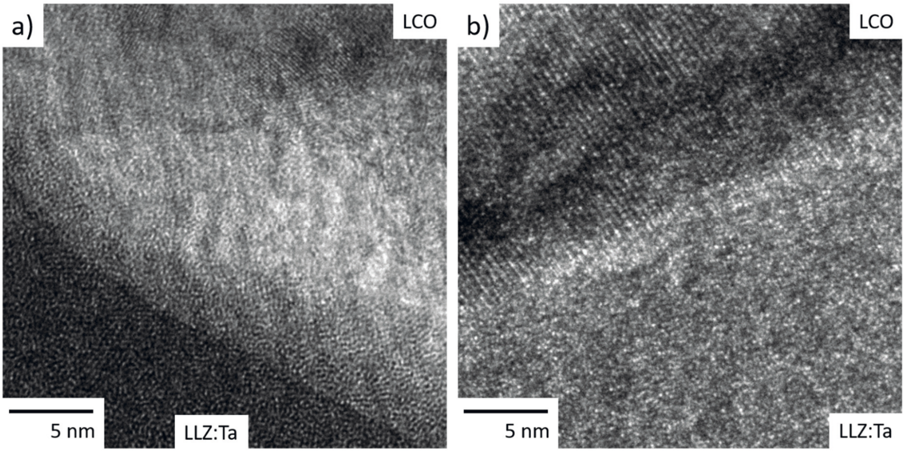

Fig. 4.37. High resolution TEM images of the a) "as prepared" and d) cycled LCO/LLZ:Ta interface.

The crystallinity of LCO and LLZ:Ta is also shown by Selected Area Electron Diffraction (SAED, Fig. 4.38). The SAED pattern of LLZ:Ta shows only the reflections corresponding to the polycrystalline cubic LLZ:Ta phase with a lattice parameter *a* of around 12.9 Å (12.95 Å–12.97 Å are reported in the literature [29]) close to the interface. The same is valid for the LCO domains, which appear to be single crystalline in 100 direction. The SAED pattern are indexed as the rhombohedral crystal structure ($R\bar{3}m$) with the lattice parameters *a*: 2.80 Å and *c*: 13.99 Å, which matches well with the rhombohedral crystal structure of LCO (*a*: 2.81 Å and *c*: 14.05 Å [126]). An elemental inter-diffusion can be excluded based on the results from Fig. 4.37a and by TEM/EDX line scans that show for the two most mobile species, Co and Al [27], a sharp border at the LCO/LLZ:Ta interface (Fig. 4.39a).

While the LCO and LLZ:Ta grains in the "as prepared" composite cathode are crystalline with atomically defined interfaces free of secondary phases, the TEM image of the cycled composite cathodes has a distinctly different appearance (Fig. 4.37b). It looks like a third layer between LCO and LLZ:Ta had formed. This layer is shown by SAED to relate with LLZ:Ta which, however, is no longer crystalline but more amorphous or disordered (Fig. 4.38a). The thickness of the disordered LLZ:Ta layer is approximately 0.1 µm after only five electrochemical cycles and agrees well with the SEM observations (Fig. 4.33b). Disordered LLZ is known to have low ionic conductivity, and explains the increasing grain boundary impedance observed in Fig. 4.31 [3, 29].

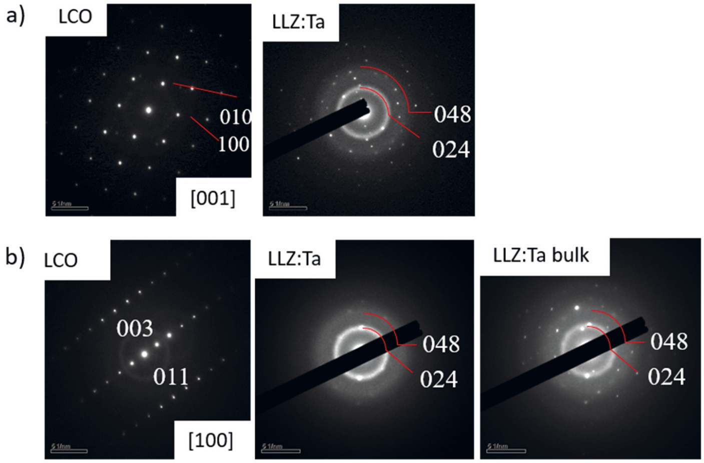

Fig. 4.38. SAED patterns of the LCO and LLZ:Ta are shown in a) for the "as prepared" composite cathode and in b) for the electrochemical cycled one (The exact location can be found in Fig. 4.34).

In addition, a change in the LCO grains is observed after electrochemical cycling. LCO remains crystalline but two phases were detected after electrochemical cycling by SAED analysis (Fig. 4.38b). While one of the phases is the rhombohedral LCO, some satellite peaks suggest that LCO was partially substituted, for example with Al, as $LiCo_{0.9}Al_{0.1}O_2$ is also rhombohedral but has slightly increased lattice parameters in *c*-direction when compared with LCO: *a*: 2.81 Å, *c*: 14.05 Å [126]; $LiCo_{0.9}Al_{0.1}O_2$: *a*: 2.81 Å, *c*: 14.08 Å [197]).

A possible exchange of Al↔Co in the electrochemical cycled composite cathode can be suggested by the TEM/EDX line scan (Fig. 4.39). While for the uncycled LCO/LLZ:Ta interface a sharp drop in the Co signal is observed at the LCO/LLZ:Ta interface, the electrochemical cycled composite cathode shows a different behavior. The Co signal decreases continuously and reaches into the LLZ:Ta area. Additionally, the Al signal has its peak within the LCO area and suggests an accumulation of Al within LCO. This is very important, as for the uncycled composite cathode the Al signal was not distinguishable from the background and after cycling a clear Al signal is detected within LCO. This suggests that after the cycling in the LCO interface area more Al is accumulated as compared to the LLZ:Ta before cycling. Therefore, it is plausible to assume that this exchange of Al↔Co is related to the fading electrochemical performance. The Al↔Co exchange will be discussed based on thermodynamic calculations in section 4.2.1.5.

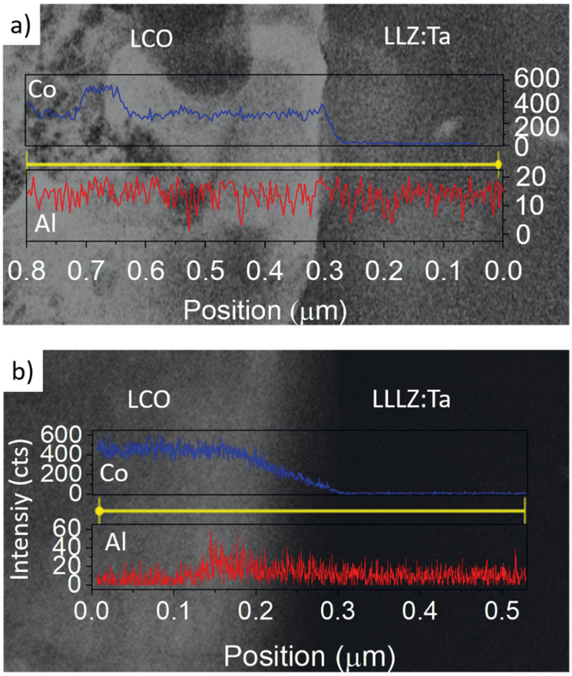

Fig. 4.39. TEM EDX line scan for Al and Co across the interface of the a) as prepared and b) cycled LCO/LLZ:Ta interface.

Co diffusion into LLZ is known to occur during high temperature processing of LCO and LLZ, and is commonly considered to lead to low ionic conductive secondary phases [1, 3]. For the presented composite cathode, however, the Co diffusion into LLZ:Ta is only observed after electrochemical cycling and implies that the Co diffusion can also be electrochemical induced. The composite cathode was additionally analyzed by XRD (Fig. 4.40).

4.2.1.4. Phase characterization of the composite cathode

To get further insight into the phase composition, XRD patterns at different focal planes of the composite cathodes were taken before and after electrochemical cycling (Fig. 4.40). The "as prepared" composite cathodes show sharp reflections corresponding to a mixture of crystalline LCO and LLZ:Ta phases, in a good agreement with the results in Fig. 4.22b [53]. A similar pattern is obtained from the back side of the composite cathode far from the LLZ:Ta separator layer (red label), suggesting that the LCO/LLZ:Ta composite cathode was unchanged or too thick (170 µm) for a full LCO utilization throughout the complete electrode (Fig. 4.40a).

To access the area close to the separator, where the majority of the electrochemical processes takes place, large parts of the composite cathode were removed using sandpaper (inset in Fig. 4.40a). For this part of the electrode, no reflections corresponding to the decomposition products of LCO or LLZ:Ta are identified.

For LCO, the Rietveld analysis suggests that the crystal structure is unchanged throughout the electrode (back: *a*: 2.815 Å, *c*: 14.06 Å and interface: *a*: 2.817 Å, *c*: 14.06 Å). The values match well with the ones reported for LCO (*a*: 2.81 Å, *c*: 14.05 Å [126]). The possible Al substitution, as suggested by TEM/EDX (Fig. 4.39) is unlikely to be detected due to similar lattice parameter ($LiCo_{0.9}Al_{0.1}O_2$: *a*: 2.81 Å, *c*: 14.08 Å [197]) and the relatively large penetration depth of XRD.

In LLZ:Ta a significant decrease in crystalline domain size from 90 nm to 20 nm was determined for the back and at the interface by Rietveld analysis, respectively. This also supports the TEM/SAED (Fig. 4.38b) analysis of amorphous or disordered state of LLZ:Ta after electrochemical cycling. The XRD patterns of the uncycled composite cathode do not show any changes in crystalline domain size throughout the whole thickness, ruling out the preparation process as a cause for the disordered interface. Based on the XRD results, the LCO/LLZ:Ta interface is crystalline throughout the whole composite cathode after the preparation process, hence, the decrease in crystalline domain size of LLZ:Ta is attributed to an electrochemically induced phenomenon, such as the formation of a third LLZ:Ta-based phase between the LCO and LLZ:Ta areas or by lower crystallinity (see section 4.2.1.3).

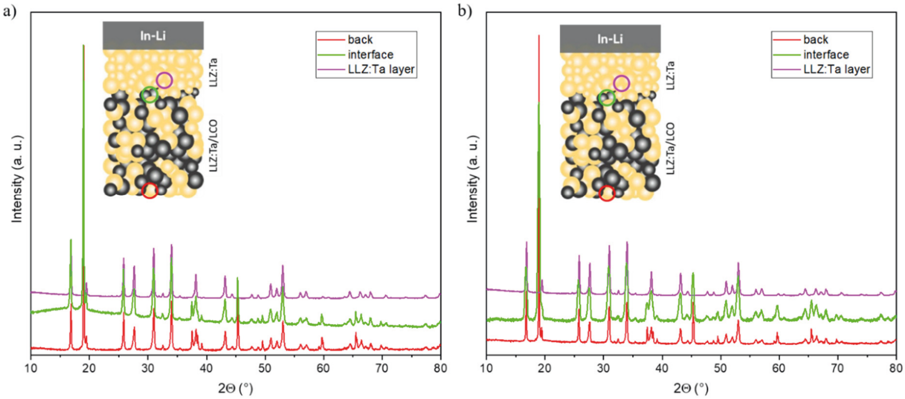

Fig. 4.40. XRD measurements of the electrochemically a) "as prepared" and b) the cycled LCO/LLZ:Ta composite cathode (schematically shown as inset). The colored circles indicate the areas from which XRD patterns (labeled with the same color code) were taken. The "back" measurements (red line) was performed from the back of the cycled composite cathode that was polished afterwards.

4.2.1.5. Thermodynamic calculations of possible secondary phases

The observed ion migration and exchange at the LCO/LLZ:Ta interface by TEM/EDX (Fig. 4.39) was calculated with the help of formation energies by *ab initio* Density-Functional Theory (DFT) calculations for Li-ion migration from/into LCO/LLZ:Ta interface and the exchange of Al-Co between LCO and LLZ:Ta, as well as for both processes simultaneously.[7] The spin-polarized DFT calculations were performed using the Projector Augmented-Wave (PAW) pseudopotential method implemented in the Vienna Ab Initio Simulation Package (VASP) code [198, 199]. The Perdew-Burke-Ernzerhof (PBE) functional was employed to approximate the exchange-correlation (XC) energy for all DFT calculations. Total Coulomb-energy (E_C) calculations were carried out using the *supercell* code and then calculated in formation energy (E_C) per formula unit [200, 201].

The Al^{3+}↔Co^{2+}, Al^{3+}↔Co^{3+}, and Al^{3+}↔Co^{4+} was modelled considering one extra or vacant Li^+ in Li sites of LLZ:Ta for the first and third case, respectively (Tab. 4.5).

Tab. 4.5. Calculated formation energies (per formula unit) of Li-ion migration and cation exchange processes between $LiCoO_2$ and $Li_{6.25}La_3Al_{0.125}Zr_{1.625}Ta_{0.375}O_{12}$

	Process				$\Delta \boldsymbol{E}_f$ **[eV]**
$\mathbf{4.5LiCoO_2}$ **+** $\mathbf{Li_{6.25}La_3Al_{0.125}Zr_{1.625}Ta_{0.375}O_{12}}$ →	I	$4.5Li_{0.972}CoO_2$	+	$Li_{6.375}La_3Al_{0.125}Zr_{1.625}Ta_{0.375}O_{12}$	0.36
	II	$4.5Li_{0.972}Co_{0.972}Al_{0.027}O_2$	+	$Li_{6.375}La_3Co_{0.125}Zr_{1.625}Ta_{0.375}O_{12}$	0.14
	III	$4.5LiCo_{0.972}Al_{0.027}O_2$	+	$Li_{6.25}La_3Co_{0.125}Zr_{1.625}Ta_{0.375}O_{12}$	0.21
$\mathbf{4.5Li_{0.972}CoO_2}$ **+** $\mathbf{Li_{6.25}La_3Al_{0.125}Zr_{1.625}Ta_{0.375}O_{12}}$ →	IV	$4.5LiCoO_2$	+	$Li_{6.125}La_3Al_{0.125}Zr_{1.625}Ta_{0.375}O_{12}$	0.13
	V	$4.5LiCo_{0.972}Al_{0.027}O_2$	+	$Li_{6.125}La_3Co_{0.125}Zr_{1.625}Ta_{0.375}O_{12}$	0.18

The Al^{3+}↔Co^{2+}+ Li^+ (reaction II: 0.14 eV, Tab. 4.5) was found to have the lowest formation energy. The migration process of only Li-ion from LCO to LLZ:Ta is energetically unfavorable (reaction I: 0.363 eV, Tab. 4.5) due to the localization of electrons in LLZ:Ta with the wide bandgap of 5.8 eV (for Al-LLZ) [202] and requires a lot of energy. A combination of Li-ion migration and Al^{3+}↔Co^{3+} is energetically more favorable than for the single reactions. Consequently, the calculations support the possibility of an interaction between the transferred Li and Co-ions in LLZ:Ta.

---

[7] The thermodynamic calculations have been performed by Liang-Yin Kuo and Dr. Payam Kaghazchi in a cooperation work. Manuscript is submitted.

To gain further insight in this interaction, the calculated magnetic moments of ions in all the reactions listed in Tab. 4.5 are shown in Tab. 4.6 as well as the spin density plot for the reaction II (Fig. 4.41).

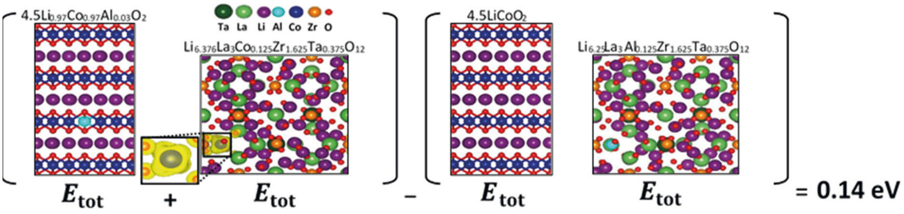

Fig. 4.41. Calculated formation energy of reaction II (Tab. 1) as well as Spin Density Distributions (SDDs) of reactants and products. An SDD isosurface of 0.04 eV Å^{-3} was used for all structures. The isosurface of the zoomed-in image is 0.006 eV Å^{-3}.

Tab. 4.6. Calculated average magnetic moments (in μ_B) of ions in LLZ with extra Li or/and added Co. The average value of magnetic moments of 3 out of 24 La cations in $Li_{6.375}La_3Al_{0.125}Zr_{1.625}Ta_{0.375}O_{12}$ that accommodate electrons is listed separately.

Structure	Li	La	Al	Zr	Ta	Co	O
$Li_{6.375}La_3Al_{0.125}Zr_{1.625}Ta_{0.375}O_{12}$	0.00	0.00, 0.14	0.00	0.00	0.00	-	0.00
$Li_{6.25}La_3Co_{0.125}Zr_{1.625}Ta_{0.375}O_{12}$	0.00	0.00	-	0.00	0.00	2.81	0.01
$Li_{6.375}La_3Co_{0.125}Zr_{1.625}Ta_{0.375}O_{12}$	0.00	0.00	-	0.00	0.00	2.48	0.00

The calculations indicate that the electron of one added Li atom is localized on La (Tab. 4.6). In the case of Co substituted LLZ:Ta, the electron is favored on Co rather than on La cations. The additional electron can lead to the reduction of the Co. Therefore, the required energy for a simultaneous exchange of Al^{3+}↔Co^{3+} combined with an accumulation of Li in LLZ:Ta is more favorable than the single reactions (reaction I and III, Tab. 4.5).

The calculations show that the Al↔Co exchange can lead to an accumulation of Li at the surface and interface of LLZ:Ta resulting in a slowed Li migration and thus capacity fading. The Li accumulation in LLZ:Ta can also lead to a volume expansion and cause disorder. This effect will also lead to lower ionic conductivity.

The results imply that the reaction II (Tab. 4.5) is thermodynamically the most feasible one. The positive Gibbs energy of the reaction II suggests that the reaction is not spontaneous when LCO and LLZ:Ta are brought in contact. This conclusion is backed by the results of the structural characterization of the composite cathode (section 4.2.1.3), that show for the "as prepared" LCO and LLZ:Ta phase no changes in the XRD pattern (Fig. 4.40a).

The hypothesis for the observed processes is that they are enabled by the following kinetic-thermodynamic reasons: i) the kinetics of Li-ion migration should be faster than that of the Al↔Co exchange. Hence, Li accumulation or depletion in LLZ:Ta is the first step in the process. The formed Li rich or Li poor LLZ:Ta compound can be considered intermediate states. ii) The exchange of Al^{3+} with Co^{2+} or Co^{4+} follows the Li migration step. Considering the energies required for Co^{2+} (reaction I, Tab. 4.5) or Co^{4+} (reaction IV, Tab. 4.5) migration, the energy required for Co^{4+}or reaction IV is less. Hence, the Al^{3+}↔Co^{4+} should take place before Al^{3+}↔Co^{2+}. Co^{4+} formation during the charging of LCO can trigger the Al↔Co exchange.

It has to be mentioned that no mechanical degradation of dense composite cathodes is observed to be the major reason for the capacity fading in rigid composite cathodes. This indicates that an optimized microstructure of the composite cathode can lead to reversible cycling of ceramic cells. However, the results of electrochemical characterization as well as the material characterization of the electrodes unambiguously point out that the degradation of the LCO/LLZ:Ta cathodes is electrochemically driven, and that the continuous increase in the impedance of LCO/LLZ:Ta interface in each cycle is related to the irreversible phase transformation and composition change of both LLZ:Ta and LCO materials due to the Li, Co and Al-ion exchange during electrochemical polarization.

The fascinating aspect is the participation of Al^{3+} substituent ions from LLZ:Ta in the electrochemically triggered phase transformation processes, which was not found reported so far. The calculations suggest that Al^{3+}, although not being redox-active, has a crucial part in the observed phase transformations of both materials by enabling the migration of Co-ions in the Al substituted LLZ:Ta. The ion diffusion can also be assumed to take place in the grain boundaries of sintered LLZ:Ta (discussed in detail in section 4.3.2.3) and provides an explanation for the increase in grain boundary impedance after electrochemical cycling Fig. 4.31. The electrochemically driven ion exchange can be assumed to be the generic reason of the cathode degradation on the naked LCO/LLZ:Ta interface. Al-free LLZ could prevent this degradation but also shows lower Li-ion conductivity in comparison to Al substituted LLZ [14, 29] or the use of CAM that suppress Al uptake such as NMC [203, 204]. Although, the structure of NMC and LCO are similar, the Mn substitution in the layered oxides increases the energy barrier of Al diffusion [203]. This would only limit the Al↔Co exchange, as it can be expected that Al ions diffuse into the CAM in the same way as Li-ions. Other crystal structures in the CAM, however, could completely suppress the Al interdiffusion. Also, Co-free CAMs might be interesting to analyze if they also incorporate Al.

Intermediate layers could be necessary for improving the cycling stability. Considering the results found, the guidelines for the design of interfacial coatings should include not only the consideration of potential profiles across the interface, but the suppression of Al^{3+} diffusion through the interphase [205]. In this respect, $LiNbO_3$, which is already commonly accepted as a protective coating for the sulfide electrolytes [206, 207], could be a promising coating for garnet-based solid batteries as well due to the higher charge of Nb^{5+} as compared to Al^{3+} and Co^{3+} ions, and thus the less favorable ion exchange. In general, the calculations of the electrochemical stability of different cathode-garnet interfaces should take into account the possible participation of other ions besides transition metal ions and lithium [122, 208].

4.2.1.6. Simulation of the Co substituted LLZ:Ta secondary phases

The XRD pattern of the Co substituted and pristine LLZ:Ta phases calculated in Tab. 4.5 have been simulated by the software VESTA (Tab. 4.7 and Fig. 4.42). From the simulated XRD pattern it is seen that all alterations lead to slightly different lattice parameters and XRD patterns compared with the pristine LLZ:Ta. The crystal structure of the Co substituted LLZ:Ta has to be slightly different from pristine LLZ:Ta. The sole Co substitution and Co substitution with Li removal has only a minor effect. The biggest change can be seen for the Co substituted and Li rich LLZ:Ta. This can easily be explained by the volume of Co^{2+} (74.5 pm) and Li^{+} (76 pm) in comparison with Al^{3+} (53.5 pm), which is much larger and will lead to an expansion of the crystal structure. The stress formed due to the expansion caused by Co substituted Li rich LLZ:Ta causes disorder within LLZ:Ta and can explain the decrease in the long-range orientation or domain size in LLZ:Ta after electrochemical cycling (see section 4.2.1.4).

Tab. 4.7. Simulated LLZ:Ta species and corresponding lattice parameter.

Structure	**Lattice parameter (Å)**
$Li_{6.25}La_3Al_{0.125}Zr_{1.625}Ta_{0.375}O_{12}$	*a*: 12.94588; *b*: 13.06591; *c*: 12.97844
$Li_{6.25}La_3Co_{0.125}Zr_{1.625}Ta_{0.375}O_{12}$	*a*: 12.90228; *b*: 12.99967; *c*: 13.10645
$Li_{6.125}La_3Co_{0.125}Zr_{1.625}Ta_{0.375}O_{12}$	*a*: 12.96567; *b*: 13.02972; *c*: 13.00250
$Li_{6.375}La_3Co_{0.125}Zr_{1.625}Ta_{0.375}O_{12}$	*a*: 12.89459; *b*: 13.07753; *c*: 13.02920

Besides, the slightly increased peak width, a splitting of the peaks is also observed. The peak split can be a result of the simulation. The unit cell is thermodynamically optimized, and the elements fixed at specific positions. In case not all positions can be occupied, vacancies remain.

In experimental XRD, multiple unit cells were measured. Throughout many unit cells, the vacancies will distribute uniformly and lead for each unit cell to peak at a slightly shifted degree. As a result, the peak splitting disappears.

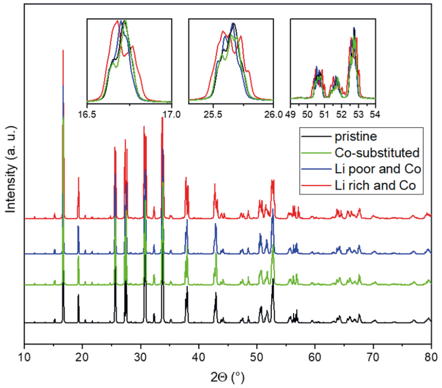

Fig. 4.42. Simulated XRD patterns of pristine LLZ:Ta and modifications as described in Tab. 4.5 with Co substitution only (green line), as well as Co substitution combined with Li excess (red line) or Li deficiency (blue line).

4.2.2. Optimization of the electrochemical stability of the composite cathode

A battery can be optimized on high energy density or cycle life [22].

4.2.2.1. Increasing the energy density

To obtain high energy density in a composite cathode, the amount of CAM has to be maximized, and the amount of solid electrolyte reduced to the threshold level to form a Li-ion conducting percolation network. In general, for a composite material system with equally sized and shaped materials around a third of the volume is required to form a percolation network [40, 41].

For the LCO/LLZ:Ta system used in this work, the Li-on percolation can be reached for LLZ:Ta representing around a third of the total volume. However, to ensure Li-ion percolation, the amount of LLZ:Ta was chosen to be 41 vol-% or 40 wt-%. Correspondingly, the amount of LCO was increased to 59 vol-% or 60 wt-%.

The higher amount of CAM in the composite cathode can result in a faster degradation. Han et al. reported less stable electrochemical properties for their LCO coated with Li_2CO_3 and Li_3BO_3 and LLZ composite cathode with increased CAM loading [22]. Their explanation was the increased interfacial stress during de-/lithiation and the resulting loss of contact area.

The here prepared composite cathode has higher density, and for equal ratio of LLZ:Ta and LCO, no fracturing was found after cycling (Fig. 4.33). Indeed, an electrochemically driven chemical change within the material was the reason for the fading capacity (section 4.2.1). Higher CAM loading might, therefore, also lead to optimized electrochemical stability and performance.

The charge and discharge of the composite cathode (thickness: 90 µm) with increased LCO content (60 wt-%) and 30 mg loading is shown in Fig. 4.43a. The first charge has a high areal capacity of 3.5 mAh cm^{-2} or an LCO utilization of 83 %. However, the charge profile is atypical for LCO. This could indicate the formation of secondary LCO phases at the LCO/LLZ:Ta interface due to the higher LCO amount. LT-LCO (as is indicated by Raman spectroscopy, Fig. 4.25) or different polymorphs of LCO (section 2.4.2) can lead to the observed charge profile of LCO [83, 209]. The first discharge already shows very low capacity of 0.2 mA h cm^{-2}.

The low capacity is a result of the high total impedance. In the EIS spectra shown in Fig. 4.43b, two distinct semicircles are found. The EIS fitting was performed as described in section 4.2.1.2. The bulk impedance of LLZ:Ta (40 Ω cm^2) is quite constant during the electrochemical cycling and fits with the values reported in section 4.2.1.2. However, the grain boundary impedance of LLZ:Ta is large, around 1599 Ω cm^2 even after the first charge. This value rises to 2135 Ω cm^2 after the fifth and to 2836 Ω cm^2 after the tenth charge. Also, the cathode and anode impedance, which cannot be separated increases from 1514 Ω cm^2 after the first charge to 3460 Ω cm^2 after the fifth and to 4587 Ω cm^2 after the tenth. The high total impedance after the first charge and the rapid increase (faster than in comparison to the same LCO/LLZ:Ta ratio, Fig. 4.29) can explain the rapid capacity fading by a large drop in cell potential.

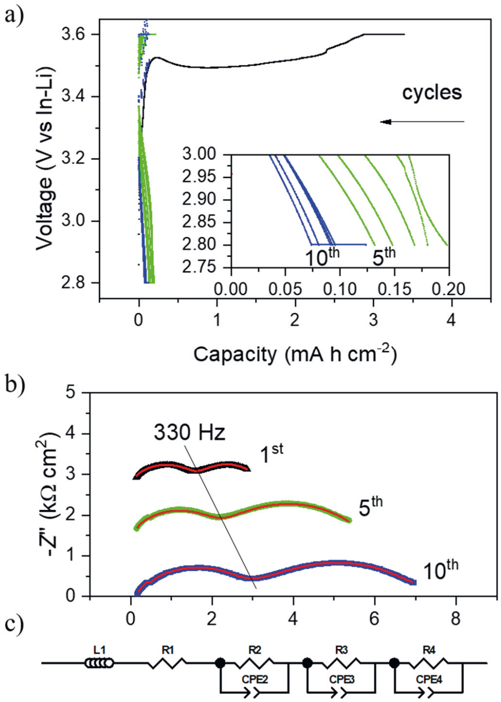

Fig. 4.43. Charge and discharge curves of an ASSLB with a composite cathode containing 60 wt-% LCO and 40 wt-%LLZ:Ta (a). The EIS spectra (3 MHz to 0.1 Hz) obtained after the first, fith, and tenth charge are shown in (b) with an offset in the –*Z*’’-direction. The fitting was performed with the equivalent circuit in (c) with L: inductance, R: ohmic resistance, and CPE: constant phase element.

4.2.2.2. Increasing the cycle stability

In order to obtain a high cycle life in ASSLBs the amount of CAM is decreased [22]. This results in a lower energy density but also in reduced interfacial stress during de-/lithiation processes and lead to less interfacial fracturing. However, as discussed in section 4.2.1 fracturing of the LCO/LLZ:Ta interface is not observed. In this composite cathode an Al↔Co exchange was related to the fading electrochemical properties and reducing capacity. As the limiting factor in the composite cathode could be the low Li-ion conductivity in LLZ:Ta, which is lower than the electronic conductivity of LCO, the Co substitution in LLZ:Ta could determine the electrochemical properties of the composite cathode [196]. In the case of a higher LLZ:Ta amount the Co is diluted and should have a smaller effect on the electrochemical performance of the composite cathode.

An ASSLB with a composite cathode having a mixing ratio of 39:61 by vol-% or 40:60 by wt-% LCO/LLZ:Ta was prepared (212 µm thick, 53 mg LCO). The electrochemical cycling is shown in Fig. 4.44a. The first cycles are comparable to the ones observed in Fig. 4.29 and provide an initial charge of 6.7 mA h cm^{-2} or an LCO utilization of 90 %. The initial high areal discharge capacity of more than 5 mAh cm^{-2} decreases during electrochemical cycling. The decrease is slower than for the composite cathode with increased LCO amount (Fig. 4.44a). However, the discharge profile is different. A sharp potential drop is observed in the first discharge period and afterwards, the discharge profile resembles LCO behavior. The cause for the rapid potential drop is unclear, although a possible explanation could be the formation of monoclinic and/or LT-LCO ($Fd\overline{3}m$). Both LCO types can show a similar potential drop [83, 209].

After an initial capacity fading, the capacity stabilizes after around eight cycles at approximately 3.3 mA h cm^{-2}. For the 20th cycle, a capacity of around 2 mA h cm^{-2} and after the 40th cycle, a capacity of around 1.4 mA h cm^{-2} is observed.

The ASSLB is further characterized by EIS measurements. The impedance spectra of the ASSLB show two distinct semicircles. The EIS fitting was performed according to section 4.2.1.2. The EIS spectra cross the x-axis around 40 Ω cm^{2}. According to section 4.2.1.2, this represents the bulk impedance of LLZ:Ta. The semicircle at higher frequencies represents the grain boundary impedance of LLZ:Ta and the one at lower frequencies the electrodes (anode and cathode). The EIS spectra have been collected during the electrochemical cycling in the charged state (Fig. 4.44b). Within the first 40 cycles the bulk impedance of LLZ:Ta is constant at around 40 Ω cm^{2}.

The major increase is seen in the semicircle at lower frequencies. An increase of around 290 Ω cm^{2} from 190 Ω cm^{2} to 480 Ω cm^{2} is observed within the first 40 cycles. This semicircle represents the composite cathode and anode impedance. Based on section 4.2.1.2, the anode impedance is constant during electrochemical cycling and the increasing impedance was caused by the composite cathode. For the fitting of the EIS spectra the real anode resistance has been fixed at 25 Ω cm^{2}. Hence, the impedance increase is caused by the composite cathode. In comparison to the composite cathode with the 50:50 LCO/LLZ:Ta mixture ratio the increase is slower. After the first five cycles the cathode impedance is increased by 50 % (80 Ω cm^{2}), while for the 50:50 ratio an increase of nearly 80 % is observed (section 4.2.1.2).

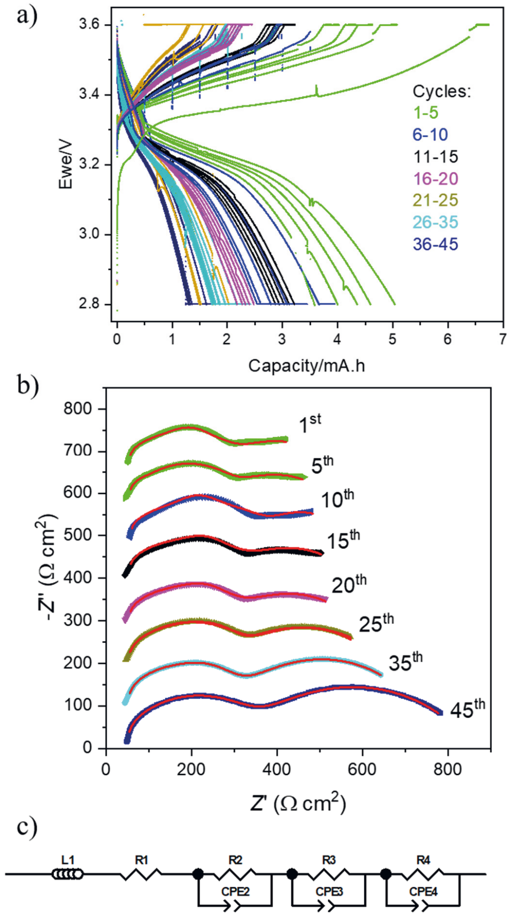

Fig. 4.44 Charge and discharge curves of an ASSLB with a composite cathode containing 40 wt-% LCO and 60 wt-%LLZ:Ta (a). The EIS spectra (3 MHz to 0.1 Hz) obtained after the charging are shown in (b) with an offset in the –*Z*''-direction. The fitting was performed with the equivalent circuit in (c) with L: inductance, R: ohmic resistance, and CPE: constant phase element. The high frequencies semicircle terminates for all measurements around 300 Hz. The spikes in a) are related to the flares in the wiring.

4.2.2.3. Discussion of the mixing ratio in composite cathodes

Three mixing ratios for the LCO/LLZ:Ta composite cathode (40:60; 50:50; 60:40 by weight) have been electrochemically analyzed. Comparing the electrochemical cycling performance, a higher amount of LLZ:Ta leads to more stable capacities and impedances. Commonly, the faster degradation with higher CAM loading is explained with the higher stress due to volume changes within the CAM and the resulting loss of interface [18, 153, 210]. For the presented composite cathodes, however, fracturing is not responsible for the fading capacity (Fig. 4.33). As suggested in section 4.2.1, the degradation of the cell capacity should be caused by an Al↔Co exchange reaction and the accumulation of Li in the LCO/LLZ:Ta interface on the LLZ:Ta side.

Low LCO loading and high LLZ:Ta loading will lead to the accumulation of Al in LCO and a dilution of Co within LLZ:Ta. The opposite is observed for high LLZ:Ta loading and low LCO loading. Potentially, the degradation occurring in the LCO is increased for low CAM loading. However, incorporation of Al into the LCO structure will still allow the de-/lithiation of Li-ions, as $LiCo_{1-x}Al_xO_2$ is a CAM [211]. A certain alteration of the LCO is supported by the discharge profiles (Fig. 4.44a). A full elemental and structural characterization of the LCO at the LCO/LLZ:Ta interface is required to fully determine composition and structure of potentially new formed phases.

The Al↔Co exchange should be limited to a thin layer at the LCO/LLZ:Ta interface as the LCO discharge profile can be observed for most of the discharge. Most likely, the low Al substitution within the LLZ:Ta ($Li_{6.45}Al_{0.05}La_3Zr_{1.6}Ta_{0.4}O_{12}$) does not allow for a deep penetration of the LCO and blocks or hinders itself. Another alternative is that Al is depleted within the LLZ:Ta interface layer and no more Al↔Co exchange can occur. Al is known to be essential to achieve high grain boundary Li-ion conduction in LLZ [21, 164]. A depletion of Al at the LLZ:Ta side of the LCO/LLZ:Ta interface would support the observed increase in LLZ:Ta grain boundary impedance in Fig. 4.43 and possible structural chanfes such as disordering.

The higher LLZ:Ta loading appears to have a beneficial effect on the stability of the electrochemical properties (Fig. 4.45). For low LLZ:Ta loading the ASSLB is basically “dead” within the first cycle. For higher LLZ:Ta loading i.e. 50 wt-% and 60 wt-%, a higher stability is observed but the same degradation trend in both is observed (Fig. 4.45).

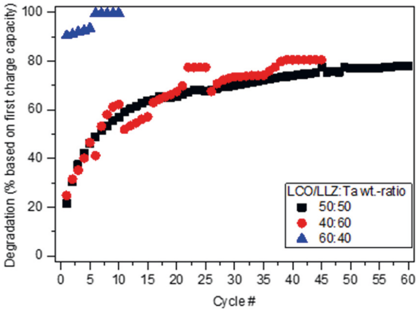

Fig. 4.45. Degradation of the LCO/LLZ:Ta composite cathodes with various mixing ratios (wt-%). The data is taken from Fig. 4.29, Fig. 4.43a, and Fig. 4.44a.

The capacity and the impedance are much more stable for a LLZ:Ta loading of 50 wt-% and 60 wt-% than for the composite cathodes with only 40 wt-% LLZ:Ta loading (Fig. 4.45) Indeed, the increase in the total impedance within the first cycles is only marginal in comparison to lower (40 wt-%) LLZ:Ta loading in the composite cathode. The initial decreasing capacity observed (Fig. 4.44b) is due to Al↔Co exchange (section 4.2.1.5) and possibly some irreversible lithiation of the anode [76, 77]. After the seventh cycle, the mentioned Al↔Co exchange can slow down. A possible saturation of Al in LCO would cause Co-ions to have longer diffusion pathways and the degradation per cycle is slower.

It appears the capacity fading is driven by the Al↔Co exchange in LLZ:Ta. With less LCO in the composite cathode and more LLZ:Ta, the Co concentration in LLZ:Ta will be diluted and have less effect and result in more stable electrochemical properties.

The Co within LLZ:Ta is reported to be detrimental for the ionic conductivity, which is already the limiting factor for the performance as it is much lower than the electronic conductivity of LCO [110, 111, 121]. This is caused by structural changes and the blocking of Li-ion pathways, resulting in high impedances. Furthermore, the Co can also cause the phase changes within LLZ:Ta and form Co-containing phases. For example, $La_2Li_{1-x}Co_xO_4$ can be formed (Tab. 4.1), a phase without Li-ion conductivity [53, 110]. Already small amounts, undetectable with the presented analysis techniques, might have a major impact on the Li-ion conduction of the main cubic LLZ:Ta phase, especially in the case of lower electrolyte loading. Thereby, the LCO/LLZ:Ta interface can mechanically be intact but due to the loss of Li-ion conduction, show the same effect as a fractured interface.

Another important aspect is the Li-ion conductivity within the composite cathode. The Li-ion conduction in LCO is low and normally only a few micrometers can be discharged [112, 212, 213]. For a working bulk composite cathode, the Li-ion conduction has to be provided by the LLZ:Ta. As soon as these Li-ion conduction pathways are blocked the composite cathode behind it can no longer be utilized. In composite cathodes above 50 µm thickness, the Li-ion conduction was shown to be a limiting factor [25]. Therefore, thicker composite cathodes tend to degrade faster, simply due to the loss of Li-ion conduction towards regions close to the current collector. A careful refinement of the conduction pathways created by LLZ:Ta could help overcome this obstacle but is not applicable for a purely powder based preparation process.

4.3. Recovery of the composite cathode

Electrochemical induced changes within the LLZ:Ta and LCO that lead to a disordered or amorphous interface region are considered responsible for the fading electrochemical performance of the presented ASSLB (section 4.2.1). According to thermodynamic calculations and literature [203], these phases are a little less favorable than the initial LLZ:Ta and LCO phases (Tab. 4.5), and the initial phases might be recoverable and the disordered area recrystallized.

The electrochemically cycled ASSLBs have been dismounted and the anode and sputter coated Au layers were polished off by sandpaper. The remaining half-cell (composite cathode and LLZ:Ta separator) was annealed (30 min at 1050 °C in air). Afterwards, the half-cell was reassembled into an ASSLB and electrochemically characterized again. Additionally, the composite cathode was structurally characterized by TEM coupled with SAED and EDX, Raman spectroscopy, and ToF-SIMS analysis.

4.3.1. Electrochemical characterization of the recovered composite cathodes

An ASSLB with a composite cathode has been prepared and electrochemically cycled (Fig. 4.46a). The charge and discharge profiles are similar to those discussed in section 4.2.1.2. After the eighth discharge only one fourth of the initial capacity of remains and the ASSLB was dismounted. The anode and the Au layers were removed by sandpaper polishing and then the composite cathode was recovered. The recovery of the half-cell is the same process as after the FAST/SPS sintering (annealing at 1050 °C for 30 min in air, section 3.2.2).

The ASSLB shows after the recovery process much higher initial capacity than after the last discharge before recovery (Fig. 4.46). The first discharge after the recovery reaches 3.1 mA h cm^{-2}. This means that around 80 % of the initial capacity of the composite cathode can be recovered (Fig. 4.46b). Afterwards, the same capacity fading is observed as for the "as prepared" composite cathode during electrochemical cycling. It has to be mentioned that the voltage dropped from 2.9 V directly to 2.8 V and hence the initial capacity might be even higher. The potential drop could be a result of concentration polarization that increases continuously during discharge or by wiring cable problems. As such a behavior is only observed for the recovered composite cathode, this indicates that the recovery process might not lead to the exact same state as observed in the "as prepared" composite cathode. Such a potential drop can also be seen in other discharge cycles.

The slightly lower capacity after the recovery can be a result of incomplete Al and Co back-migration i.e. not all atoms go back to their initial position and LCO removal by polishing. In order to remove the Au layer and polish the composite cathode after the annealing process, a few micrometers of the composite cathode are removed. Additionally, the recovering process requires optimization of the temperature, the dwell time, and the heating and cooling rate. Therefore, the recovery process might not be completed after just 30 min at 1050 °C in air.

The capacity fades rapidly, and only 1.6 mA h cm^{-2} after the seventh cycle is observed. The reason for the capacity fading should be related to an Al↔Co exchange as described in detail in section 4.2.1.5.

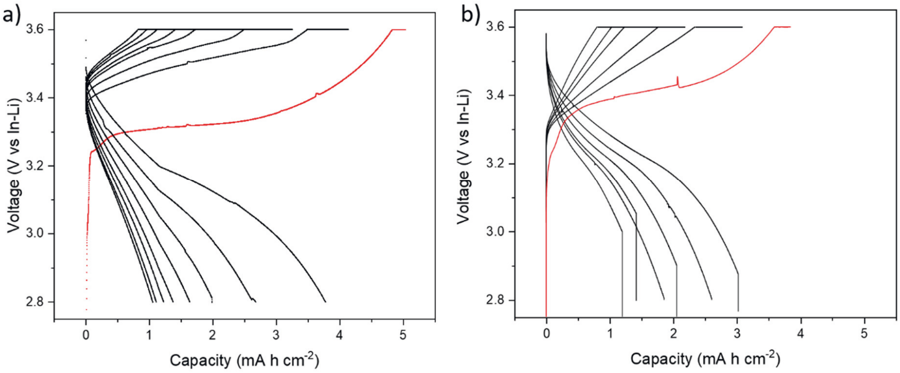

Fig. 4.46. Charge and discharge of an ASSLB with a composite cathode. The composite cathode shown in (a) was disassembled after the eight cycle, polished, annealed again (1050 °C for 30 min in air) and then reassembled into an ASSLB (b). The charge and discharge of this recovered composite cathode is shown in (b). The reason for the potential drop in b) could be material or wiring cable related.

EIS measurements of the recovered ASSLB have been performed after the first and fifth charge (similar to section 4.2.1.2). The EIS spectra show an offset on the x-scale, indicate two semicircles, and a diffusion tail (Fig. 4.47a). After the fifth charge the semicircle in the medium frequency range is increased. The fitting of the EIS data was done with the equivalent circuit shown in Fig. 4.47b, which is the same as used for the “as prepared” ASSLB (Fig. 4.31). Hence, the battery components were assigned accordingly. The high frequency intersection with the x-axis represents the bulk resistance of LLZ:Ta. The semicircle at high frequency range is the grain boundary resistance of LLZ:Ta. In the medium frequency range, a semicircle for the cathode and anode should be seen. As described in section 4.2.1.2, the cathode and anode impedance can overlap and their respective semicircles merge into one semicircle. The diffusion tail cannot be mistaken as a large semicircle. The fitting revealed that the real impedance of the tail of both EIS spectra is in the range of 10^{20} Ω cm^2 (which is the maximum value given by the ZView software package) and by that too large for another semicircle.

The bulk impedance of LLZ:Ta is nearly constant within the measuring and fitting inaccuracies. After the first charge it is 32 Ω cm^2 and after the fifth 42 Ω cm^2 which is similar as for the "as prepared" ASSLB (Fig. 4.31). The grain boundary impedance of LLZ:Ta is in comparison with the "as prepared" ASSLB increased. While for the "as prepared" ASSLB a grain boundary impedance of 47 Ω cm^2 (section 4.2.1.2) was calculated after the first charge, the grain boundary impedance was 74 Ω cm^2 for the recovered ASSLB. After the fifth charge it is 102 Ω cm^2. The increase in the grain boundary impedance of LLZ:Ta can again be attributed to the Al↔Co exchange and the formation of lower or nonconductive phases (section 4.2). The initially increased LLZ:Ta grain boundary impedance suggests that the recovery process is incomplete. This is supported by TEM characterization (section 4.3.2.1).

The electrodes impedance increases from 570 Ω cm^2 to 787 Ω cm^2. A separation between anode and cathode is not possible by the used fitting method. Based on section 4.2.1.2, however, the anode impedance can be assumed small and even slightly decreasing during electrochemical cycling from initial 25 Ω cm^2 to 10 Ω cm^2 after the fifth charge. As the anode for the "as prepared" and recovered ASSLB are same, it can be assumed that the anode impedance is also the same.

The impedance increase is linked to the Al↔Co exchange and the formation of less ordered phases (section 4.2). The impedance increase is smaller than observed for the "as prepared" composite cathode, while the capacity fading is in the same range (Fig. 4.31 and Fig. 4.47). A possible explanation could be that the LLZ:Ta is not fully recovered, as the Al↔Co exchange is not fully reversed (see TEM results in section 4.3.2.1). This can alter the current pathways through the composite cathode and lead to a different impedance behavior. Besides, the LCO/LLZ:Ta interface could change due to the repeated annealing step.

In addition, multiple parameters of the ASSLB assembly can also affect the cell performance. This includes the surface preparation, the attaching of the anode, and the atmosphere during electrochemical cycling. The surface is polished manually and can have roughness. This can lead to locally higher charge currents and faster degradation. The manually attached anode can lead to the same effect. Also the glovebox conditions such as the atmosphere, or possible leakage of oxygen into the Swagelok cell can lead to faster degradation. Other effects due the current collector, the wiring, the measuring temperature, or the applied currents can be neglected.

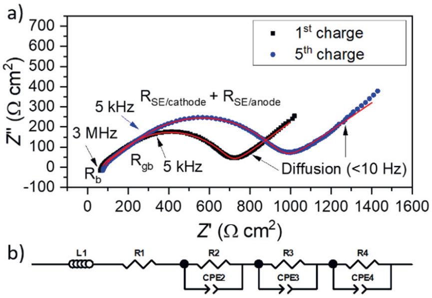

Fig. 4.47. EIS spectra of the ASSLB with recovered composite cathode after the first and fifth charge (a). The fitting was performed with the equivalent circuit shown in (b).

4.3.2. Structural characterization of the recovered composite cathodes

Structural characterization of the composite cathode is important to understand the changes in the electrochemical properties. In section 4.1 the composite cathode was characterized after FAST/SPS sintering and annealing. The structural changes due to electrochemical cycling have been discussed in section 4.2. Here, the focus will first be on the TEM characterization of the recovered composite cathode.

Based on the electrochemical data presented in Fig. 4.46, the thermal treatment impacts the electrochemical properties. Raman spectroscopy and ToF-SIMS analysis were used to analyze the composite cathodes at different stages (FAST/SPS sintered, "as prepared", cycled, and recovered) to get a full understanding of the thermal and electrochemical effects.

4.3.2.1. Interface characterization by TEM

High resolution TEM was used to analyze the LCO/LLZ:Ta interface in detail for the FAST/SPS sintered, "as prepared", and cycled stage (Fig. 4.21, Fig. 4.23, and Fig. 4.37). Analogous investigations have been conducted after the recovery of the LCO/LLZ:Ta interface (Fig. 4.48). After the electrochemical cycling satellite peaks have been found within the LCO and the LLZ:Ta was amorphous at the LCO/LLZ:Ta interface (Fig. 4.38b).

First, the successful preparation of the TEM lamella and the high resolution TEM indicate the mechanical integrity of the recovered composite cathode (Fig. 4.48a and b). The high resolution TEM after the recovery shows a clear separation of LCO and LLZ:Ta (Fig. 4.48b) as can be expected based on the TEM after FAST/SPS and annealing, and electrochemical cycling (Fig. 4.21 and Fig. 4.37). Furthermore, the high resolution TEM of LCO and the LLZ:Ta appear crystalline and layered in most areas (Fig. 4.48b).

However, in the vicinity of the LCO/LLZ:Ta interface the ordering of LLZ:Ta appears a little less than in the bulk LLZ:Ta, but similar to the state in the "as prepared" LCO/LLZ:Ta interface (Fig. 4.48b, and Fig. 4.21b and Fig. 4.37a) The edge between LCO and LLZ:Ta is mostly sharp (Fig. 4.48b). The high resolution TEM resembles those of the "as prepared" LCO/LLZ:Ta interface (Fig. 4.21b). The amorphous areas indicate that the recrystallization induced by the thermal recovery is incomplete and help to understand the initially higher grain boundary impedance in comparison to the uncycled composite cathode (sections 4.2.1.2 and 4.3.1).

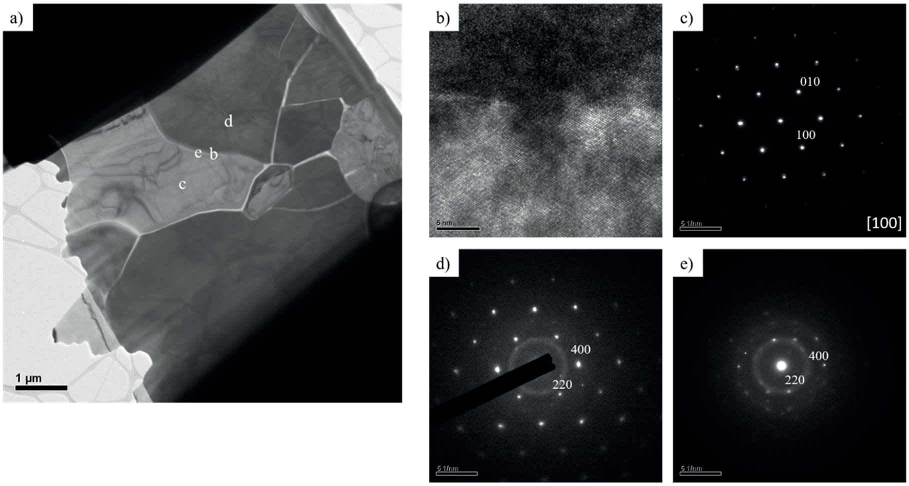

Fig. 4.48. TEM images of the LCO/LLZ:Ta interface in a) high resolution TEM is shown in b). SAED diffraction patterns of c) LCO, d) LLZ:Ta, and e) the LCO/LLZ:Ta interface.

The crystallinity of the LCO and LLZ:Ta is confirmed by SAED (Fig. 4.48c and d). The SAED of LCO shows defined peaks, typical for LCO (Fig. 4.48c). The lattice parameters are *a*: 2.80 Å and *c*: 13.99 Å, which match well with the rhombohedral crystal structure of LCO (*a*: 2.81 Å and *c*: 14.05 Å [126]).

Also, the LLZ:Ta pattern has only defined peaks (Fig. 4.48d), corresponding to the polycrystalline cubic LLZ:Ta phase with a lattice parameter *a* of around 12.9 Å (12.95 Å – 12.97 Å reported in literature [29]) in the bulk. At the interface, the SAED pattern is not fully clear and indicates some amorphous parts, similar to the high resolution TEM (Fig. 4.48b). Nevertheless, the SAED pattern is in comparison to the one after electrochemical cycling much more defined. This shows that the recovery process can lead to a recrystallization of the LLZ:Ta and the recovered LCO/LLZ:Ta interface appears more similar with the "as prepared” LCO/LLZ:Ta interface (Fig. 4.21b). As the recovery process is not optimized, some amorphous areas remain. The crystallinity of the LCO/LLZ:Ta interface is crucial to achieve a low interfacial impedance. In Fig. 4.20 was shown that crystalline LCO/LLZ:Ta interfaces are lower impeded in comparison to amorphous ones [53]. The crystallinity of the LCO/LLZ:Ta interface can help to understand the lower impedance after recovery in comparison with the cycled state (Fig. 4.31 and Fig. 4.47).

The amorphous layer on the side of the LLZ:Ta is expected to be a result of Al↔Co exchange (section 4.2). By TEM/EDX the element distribution was qualitatively analyzed by TEM/EDX line scans (Fig. 4.49). For La and Zr a sharp edge is found and proofs that no diffusion of these elements take place during the electrochemical cycling and annealing. For Ta also a clear edge is found but also a constant signal within the LCO area. As Ta is the largest cation in the LLZ:Ta, it is unlikely to diffuse. The constant Ta signal can be considered as a background signal. The Co signal is constant within the LCO area. Around 0.5 µm from the interface the signal drops. This can be related with the contrast change seen in the TEM image which has a higher contrast in this area (Fig. 4.49a). The TEM sample can have an inhomogeneous thickness. The preparation of the TEM lamella with composite materials can face the challenge that the sputtering rate of the materials is different. LLZ:Ta, as the composition with a higher atomic mass, should be thinned at a lower rate than LCO. Hence, the contrast difference seen in the TEM image can be a result of an incline from the thinner LCO area to the thicker LLZ:Ta area. The electron beam would hit the surface at a different angle and the scattering can be altered or weakened. For oxygen, the same observations are made, which also shows a lower intensity in this region.

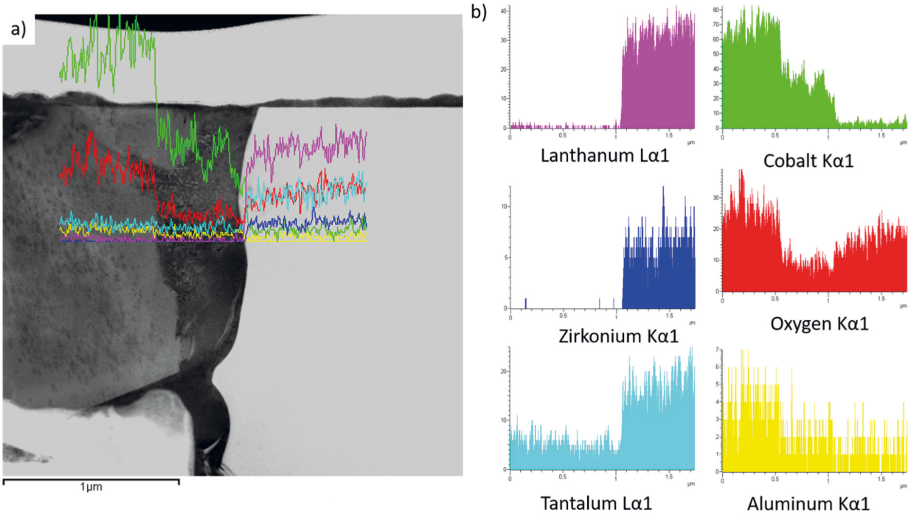

Fig. 4.49. TEM dark field image of the LCO/LLZ:Ta interface (a) including the TEM/EDX line scan. The dark area is LCO and the light area is LLZ:Ta. In b) the single line scans for the single elements are shown. The color code is given in b).

The Co signal does not directly disappear at the LCO/LLZ:Ta interface but reaches a few nanometers into LLZ:Ta (Fig. 4.49b). The low Co signal within the LLZ:Ta is constant and can be considered as background. For Al the highest intensity is measured within the LCO area. In fact, the Al signal nearly is double in intensity within the LCO in comparison with the LLZ:Ta. In the LLZ:Ta, the Al signal is rather constant and difficult so separate from background noise.

Small area scans have been prepared to verify the line scan results (Fig. 4.50a). The small area scans were taken within the LCO, the darker interface, the LCO/LLZ:Ta interface, and the LLZ:Ta area. In the LCO area signals for Co and Al are found (Fig. 4.50b and c). These signals proof that an electrochemical driven Al↔Co exchange occurs. In the “as prepared” LCO/LLZ:Ta interface (stage before cycling) with the same annealing step, no Al is found within the LCO (Fig. 4.23 and Fig. 4.39). Besides, the peaks related to La, Zr, and Ta are found in the recovered sample (Fig. 4.47b). The peaks are of low intensity in comparison with the peaks in the LLZ:Ta area and the main peaks are absent and can therefore be neglected.

In the darker area, the spectra appear same and it supports the idea that the higher contrast is indeed a result of uneven thickness. Right at the LCO/LLZ:Ta interface the peaks of all elements can be observed. In the LLZ:Ta area the peaks of La, Zr, and Ta are the major peaks. Also, the peaks related to Co and Al are found with low intensity. The Al↔Co exchange can, therefore, also be shown within the recovered LLZ:Ta (Fig. 4.50b and c). As no Co is found in LLZ:Ta before electrochemical cycling (Fig. 4.23), the Co within the LLZ:Ta should be due to the electrochemical cycling which is not removed during recovery.

The intensity of the peaks of the relevant elements at the measured areas is shown in Fig. 4.50c. As the sample was exposed to air during the preparation process, the oxygen signal has to be neglected and the obtained atomic-% can be just analyzed as a trend. The Co signal within the LCO areas is high, however, in the inclining area it is slightly elevated. Due to the different electron beam angles a detailed discussion is not possible. Right at the LCO/LLZ:Ta interface the Co signal reduces due to overlap of LCO and LLZ:Ta within the measuring area. Within the LLZ:Ta area the Co signal is still measurable with a low intensity. The Al signal in the LCO area has the same trend within LCO as Co. The Al signal within the LCO area is higher in comparison with the LLZ:Ta area. It can be suggested that Al accumulates at the LCO/LLZ:Ta interface on the LCO side as the signal at the interface is elevated when compared with the Al signal in the LLZ:Ta area. A similar observation is made by ToF-SIMS (Fig. 4.53 to Fig. 4.56).

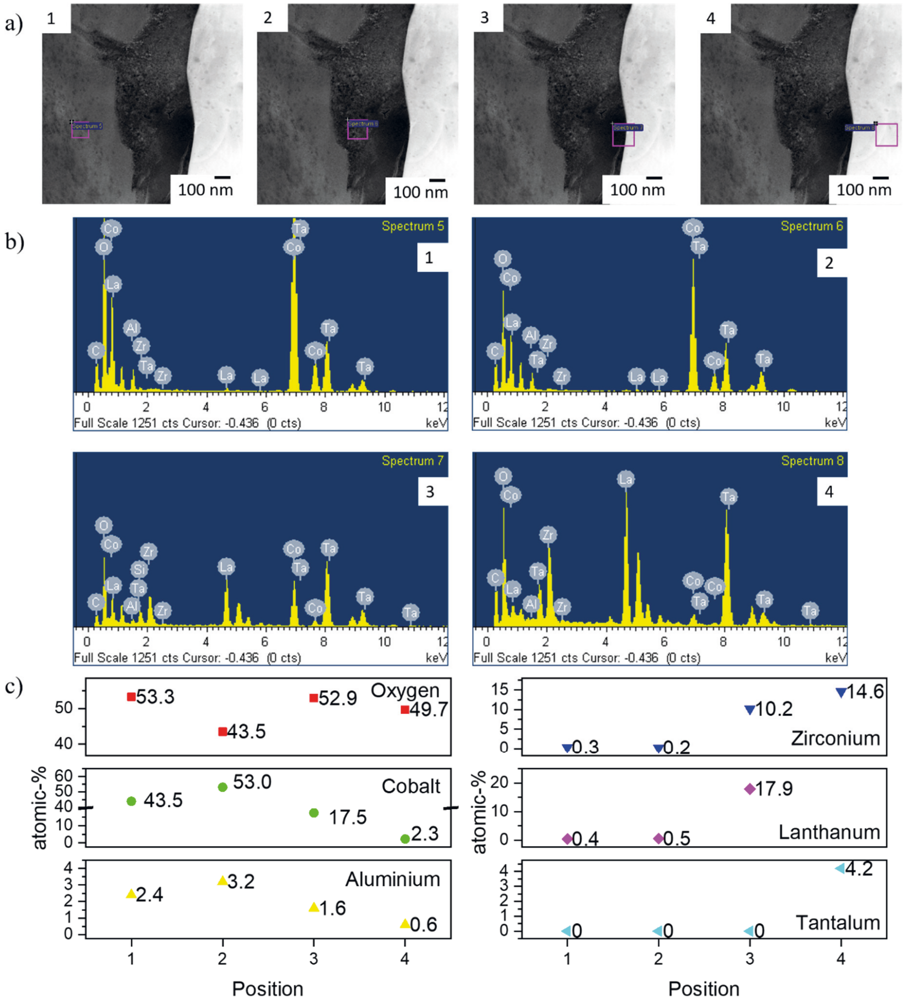

Fig. 4.50. a) Small area TEM EDX scans with the corresponding spectra in (b) and the calculated atomic-% in (c). The dark area is LCO and the light area is LLZ:Ta. As the sample was exposed to air during the preparation process, the oxygen signal has to be neglected and the obtained atomic-% can be just analyzed as a trend.

4.3.2.2. Characterization of the composite cathodes by Raman spectroscopy

Raman spectroscopy is a fingerprint method to characterize the structure of LCO and LLZ:Ta [19, 190, 191, 214-216]. To compare the changes within the LCO and LLZ:Ta, the FAST/SPS, "as prepared", cycled, and recovered state of the composite cathode were analyzed (Fig. 4.51 and Fig. 4.52). The focus will be first on LCO and then on LLZ:Ta.

The LCO shows in the FAST/SPS state two peaks at 497 cm^{-1} (E_g) and 595 cm^{-1} (A_{1g}, Fig. 4.51a). These are the characteristic peaks of rhombohedral HT-LCO. In contrast to the pure LCO sintered by FAST/SPS, the intensity ratio of the peaks nearly match with the pristine LCO spectra [143, 144, 189, 191].

The sintering of LCO in Ar (Fig. 4.24) can lead to a loss of oxygen and alter the LCO structure, by a reduction of Co^{3+} to Co^{2+}, as seen in Fig. 4.24. In case LCO and LLZ:Ta are co-sintered this effect is less observable and could suggest that oxygen is more easily removed from LLZ:Ta than LCO.

After annealing, the peaks are sharper in comparison to the FAST/SPS sintered LCO and could indicate that the crystallinity and the long-range orientation are increased. The full width at half maximum decreases from 11 cm^{-1} - 13 cm^{-1} in the FAST/SPS sintered LCO to 9 cm^{-1} - 12 cm^{-1} after annealing.

In the cycled state the Raman spectra are changed (Fig. 4.51c). Still the characteristic peaks can be observed, however, the peak width and intensity ratio are changed. Starting from the bulk LCO towards the LCO/LLZ:Ta interface, the peaks broaden. In the bulk, the typical LCO Raman spectra are seen. For the measurements closer to the LCO/LLZ:Ta interface, the peaks broaden, and the peak intensity is decreased. These changes within the Raman spectra can be a result of disorder [189, 190]. Several research groups have reported a similar observation for physical vapor deposition or other deposition methods for LCO [189, 190, 217]. After crystallization by a subsequent annealing process at high temperature in air the LCO peaks get more defined.

The LCO peak position is further defined by the Li concentration within $Li_{1-x}CoO_2$ [132, 144, 189]. For the charged LCO state ($Li_{0.5}CoO_2$), the peaks are broadened and shifted slightly to lower wavenumbers. Although, the LCO should be discharged, the SoC was only determined by the cut-off voltage and not by a structural characterization and hence the LCO could still be at least partially charged. Overpotentials within the ASSLB can lower the cell potential and the cut-off voltage is reached while LCO is still partially charged [132]. This could be a reason for the widened Raman peaks.

Another explanation can be the observed Al↔Co exchange. The substitution of Al into LCO will lead to a peak broadening [218]. The Al↔Co exchange is predominantly at the LCO/LLZ:Ta interface and can explain the more significant peak broadening at the interface.

This, however, can only be an assumption as the focus area of the Raman laser is in the micrometer-range while the Al substituted LCO has only a thickness of around 0.1 µm.

The full substitution of Co and the formation of $LiAlO_2$ is unlikely, as the characteristic $LiAlO_2$ peaks at 485 cm^{-1} and 596 cm^{-1} are absent in the Raman spectra [219, 220].

After the recovery, the LCO peaks are again sharp (Fig. 4.51d). Furthermore, the intensity ratio of the two peaks resembles more those of the rhombohedral HT-LCO in comparison to the "as prepared" state (Fig. 4.51b and d). A possible explanation can be the repeated annealing step in oxygen containing atmosphere. It is known that LCO can lose oxygen at high temperature in oxygen-free atmospheres such as Ar (as present in the FAST/SPS process) and faces structural changes that can lead to the formation of LT-LCO (explained in detail in section 4.1.9.1) [189].

As the Raman spectra of the recovered LCO resemble the ones after preparation, it is assumed that the re-annealing after the electrochemical cycling can reverse the chemical changes occurring during the electrochemical cycling and homogenize the SoC in the LCO due to uptake of Li-ions from LLZ:Ta. The possibly formed $LiCo_{1-x}Al_xO_2$ during the electrochemical cycling was not detected (Tab. 4.5). Repeated high temperature treatment of LCO and LLZ:Ta can also lead to elemental inter-diffusion, however, due to the high Raman intensity of LCO, small amounts of any secondary phase is most likely not detectable.

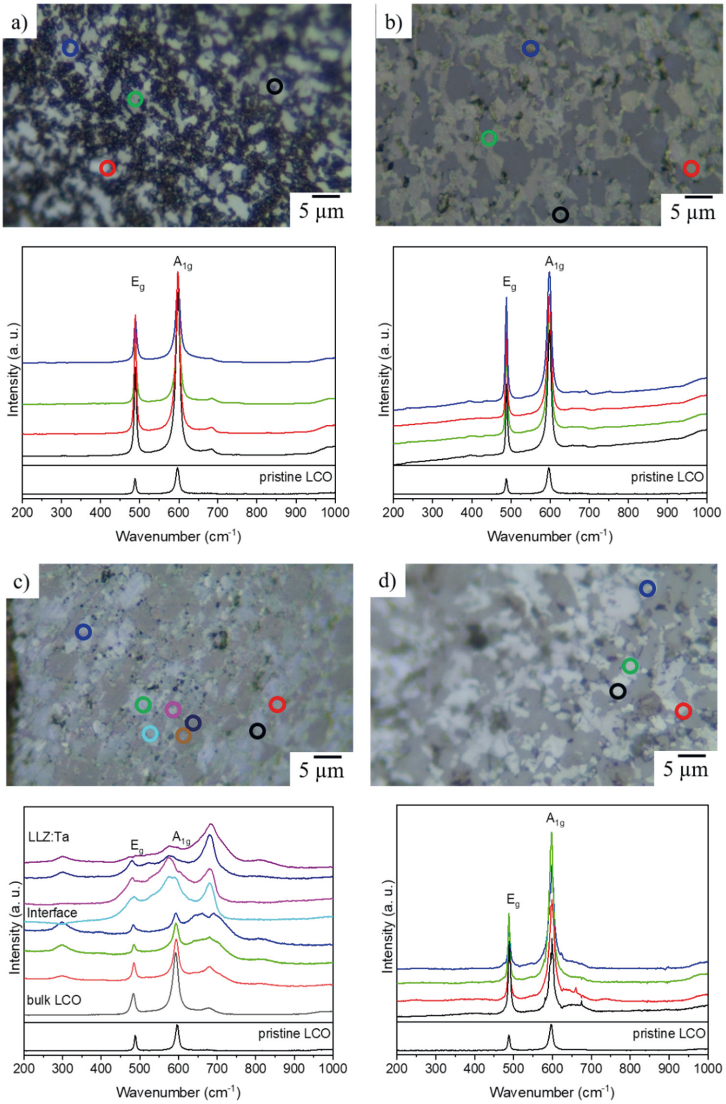

Fig. 4.51. Light microscope images of the composite cathode after different handling steps: a) FAST/SPS, b) “as prepared”, c) cycled, and d) recovered. The locations of the collected Raman spectra within the LCO regions (lighter) are color coded and the spectra are shown below. The lighter regions are LLZ:Ta.

The Raman spectra of LLZ:Ta after the FAST/SPS sintering show the typical peaks for cubic Ta substituted LLZ, however, the intensity is low (Fig. 4.52a) [9, 18, 19, 175]. Additionally, the two peaks of HT-LCO are seen. This is caused by the mixture of LCO and LLZ:Ta. Both materials have a grain size in the micrometer range and the focus area of the Raman laser might always focus some LCO areas. Due to the penetration depth of the Raman laser also underlying LCO areas are detected. The Raman intensity of LCO is higher than that of LLZ:Ta and already small amounts can be detected clearly, even when the focus area is within the LLZ:Ta area. Ren et al. made a comparable observation for a similar LCO/LLZ system [195].

The annealing process increases the peak intensities for the LLZ:Ta. This means the crystallinity is increased in the “as prepared” in comparison the one after FAST/SPS prepared one (Fig. 4.51a and b).

After electrochemical cycling, the Raman spectra of LLZ:Ta have changed (Fig. 4.52c). A very broad peak around 300 cm^{-1} and a large and intense peak at around 700 $cm^{-1}$with a shoulder around 850 cm^{-1} is observed. The reason for the peaks at 300 cm^{-1} and 850 cm^{-1} is unclear but might be related to $La_2Li_{1-x}Co_xO_4$ formation, as it was already found by Rietveld analysis as a small impurity phase after FAST/SPS (Tab. 4.1). However, no Raman spectrum nor the synthesis route for the $La_2Li_{1-x}Co_xO_4$ was found in the literature.

The peak at around 700 cm^{-1} can be a result of the Al↔Co exchange. Tsai et al. prepared $Li_{6.3}Co_{0.1}La_3Zr_{1.6}Ta_{0.4}O_{12}$ and the Raman spectrum shows a very intense peak at 693 cm^{-1}, which is also the most intense peak [18]. As the Co substitution is low, the LLZ:Ta spectra is also observed. The peak was analyzed with multiple laser wavelengths of 457 nm, 532 nm, and 785 nm by Tsai et al. and showed changing intensity, and was assigned to be a photoluminescence peak due to the Co substituted in the LLZ:Ta [18]. In the electrochemical cycled composite cathode, the LLZ:Ta spectra is undetected and suggests that the Co substitution is higher.

Furthermore, the LCO could have formed some Co_3O_4 during the electrochemical cycling as result of local overcharge. Co_3O_4 has in the Raman spectrum one intense peak at 695 cm^{-1} and three less intense peaks in the range from 400 cm^{-1} to 600 cm^{-1} [143]. The low intensity peaks might be overlooked due to the high intensity of the 695 cm^{-1} peak.

After the recovery process, the LLZ:Ta spectra can be observed again (Fig. 4.52d). Depending on the position, the spectra appear different. In some positions in the LLZ:Ta, the peak at around 700 cm^{-1} is still the major peak but also the peaks of cubic structured LLZ:Ta are observed. In other LLZ:Ta areas, especially in the proximity to the LCO/LLZ:Ta interface, the spectra of cubic structured LLZ:Ta are even more pronounced. This suggests that the recovery process starts to crystallize the LLZ:Ta from the LCO/LLZ:Ta interface and that the phases prior to the electrochemical cycling are recovered.

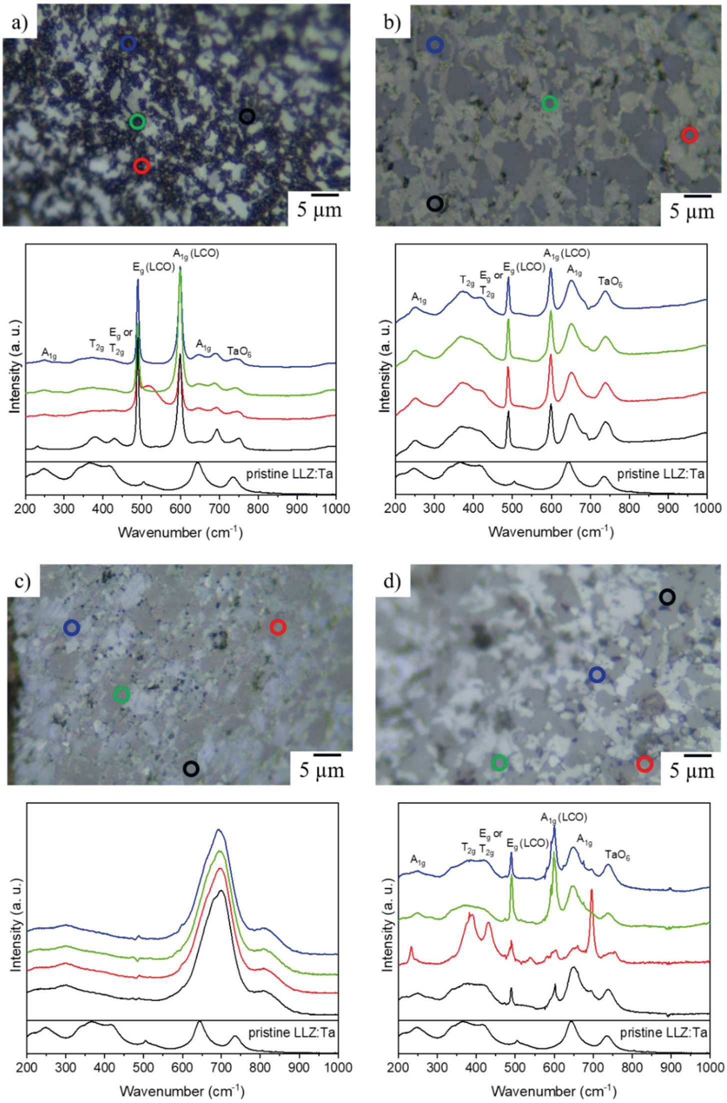

Fig. 4.52. Light microscope images of the composite cathode after different handling steps: a) FAST/SPS, b) "as prepared", c) cycled, and d) recovered. The locations of the collected Raman spectra within the LLZ:Ta regions (darker) are color coded and the spectra are shown below. The darker reqgions are LCO. The LLZ:Ta modi are labeled according to Tietz et al. [221]. In the FAST/SPS, "as prepared", and recovered composite cathode the peaks of LCO (E_g and A_{1g}) can be found.

The thermal recovery process might not be completed after the 30 min annealing in air at 1050 °C, as the observed Raman spectra are different than in the "as prepared" state. The thermodynamically more favorable LCO and LLZ:Ta phases, in comparison to

$LiCo_{1-x}Al_xO_2$ and $Li_{6.45}Al_{0.05-x}Co_xLa_3Zr_{1.6}Ta_{0.4}O_{12}$, should have partially reformed (Tab. 4.5). The incomplete recovery suggests that the process still has optimization potential (dwell time, temperature, and heating and cooling rate). Potentially, a longer annealing time could completely recover the phase pure cubic crystalline LLZ:Ta phase. However, a longer annealing time could lead to the known secondary phase formation at LCO/LLZ:Ta interfaces [27, 113]. The LLZ:Ta in proximity of the LCO/LLZ:Ta interface meanwhile is recovered and provides a low impeded interface and enable good ionic conductivity that lead to the recovery of the capacity (Fig. 4.47).

4.3.2.3. Characterization of the composite cathode by ToF-SIMS

ToF-SIMS analysis can characterize the qualitative elemental composition of the composite cathode and half-cell. The detection limit of ToF-SIMS analysis is in the ppm or even ppb and it can detect Li [146-148]. In combination with TEM (section 4.3.2.1) and Raman spectroscopy (section 4.3.2.2), ToF-SIMS analysis enables a more detailed understanding of the changes occurring within the half-cells (composite cathode and LLZ:Ta separator) at different stages (FAST/SPS sintered, “as prepared”, cycled, and recovered). At all stages, elemental mappings by ToF-SIMS have been performed (Fig. 4.53 to Fig. 4.56).

In all characterized half-cells (composite cathode and LLZ:Ta separator), La, Zr, and Ta show nearly double intensity in the LLZ:Ta separator. As the composite cathode is a nearly 50:50 vol-% mixture of LLZ:Ta and LCO. However, ToF-SIMS cannot quantify the ions and only the elemental distribution should be evaluated. Nevertheless, the trends within similar samples can be discussed.

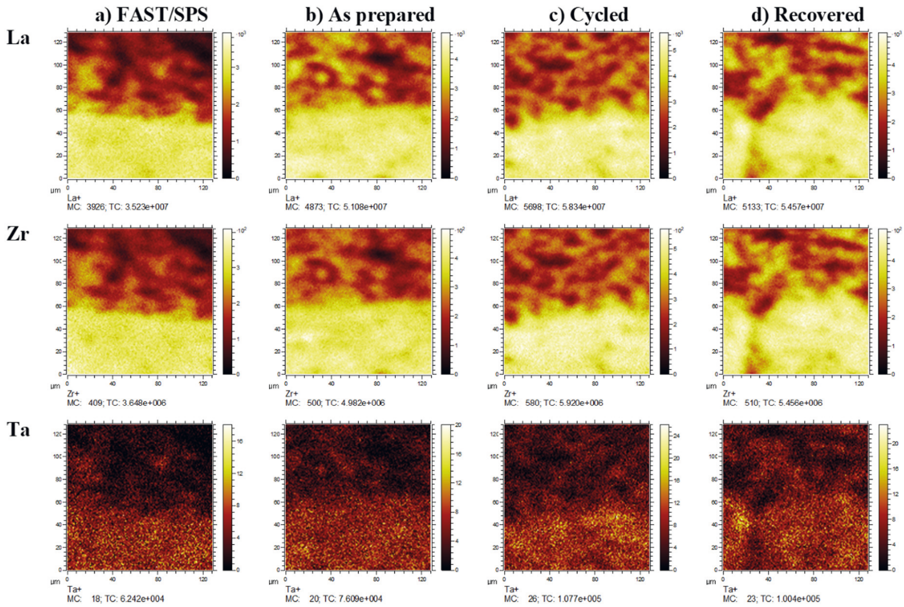

Fig. 4.53. ToF-SIMS mapping of La, Zr, and Ta for the half-cells after a) FAST/SPS, b) "as prepared", c) cycled, and d) recovered. The LCO/LLZ:Ta composite cathode is at the top and the LLZ:Ta separator at the bottom. ToF-SIMS cannot quantify the ions and only the elemental distribution should be evaluated.

The homogeneous intensities show an equal distribution of La, Zr, and Ta. It can be assumed, that in the case secondary phases have formed that an inhomogeneous distribution would be seen. By that ToF-SIMS supports the observations made with other methods (SEM: Fig. 4.28 and Fig. 4.33, and TEM: Fig. 4.21, Fig. 4.34, and Fig. 4.48) that suggest a clean LLZ:Ta phase.

The Co signal is only found within the composite cathode area. In the FAST/SPS sintered sample the Co signal in proximity of the LLZ:Ta separator is increased (Fig. 4.53a). The other samples show a more homogenous Co distribution. To rule out any likelihood of Co diffusion across the interface, a bilayer of LLZ:Ta and LCO was co-pressed, sintered by FAST/SPS, and measured by ToF-SIMS (Fig. 4.54). In this sample the Co signal is homogeneous within the LCO. Diffusion cannot explain the slightly lower Co signal.

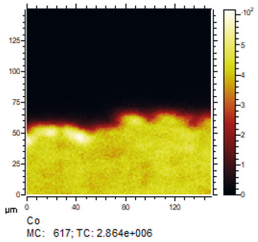

Fig. 4.54. ToF-SIMS mapping of Co of a bilayer of LLZ:Ta (top) and LCO (bottom) sintered by FAST/SPS.

As the FAST/SPS sintered stage is not used for the electrochemical analysis this observation will not be discussed in detail (section 4.1.8).

The "as prepared" sample shows a homogeneous Co distribution within the composite cathode. However, the Co signal at the border to the LLZ:Ta separator is a little less intense. The electrochemical cycled and recovered samples show the same Co distribution as the "as prepared" one.

The Li signal in the composite cathode is higher in all samples than in the LLZ:Ta separator (Fig. 4.55), as expected. In LCO, the Li is roughly 7 wt-% compared to 5 % in the LLZ:Ta. Hence, the highest Li concentrations are detected in the same spots as the highest Co (Fig. 4.55). The FAST/SPS sintered composite cathode shows a lower Li signal on average than the other samples. As reported by Le Van-Jodin et al., high temperature treatment of LCO in Ar can lead to Li loss and a potential decomposition [189]. This process is reversible by high temperature treatment in air and a present Li source. As shown by Raman spectroscopy (Fig. 4.24), the LCO peaks hints towards the formation of LT-LCO secondary phase after the FAST/SPS process. The Li concentration is in LT-LCO lower than in HT-LCO [222]. ToF-SIMS can validate this hypothesis and help explain the improved electrochemical performance after the annealing process (Fig. 4.26). The lower crystallinity after the FAST/SPS process, as observed by TEM (Fig. 4.23) could just be one of the reasons for the high impeded LCO/LLZ:Ta interface (Fig. 4.26). The Li distribution in the cycled and recovered sample are same as the Co distribution (Fig. 4.55b to d).

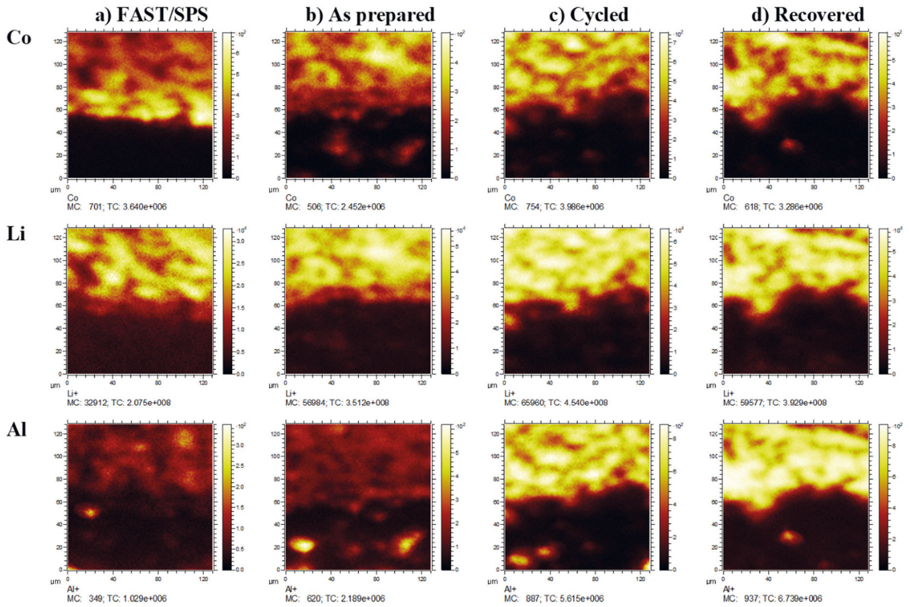

Fig. 4.55. ToF-SIMS mapping of Co, Li, and Al for the half-cells after a) FAST/SPS, b) “as prepared”, c) cycled, and d) recovered. The LCO/LLZ:Ta composite cathode is at the top and the LLZ:Ta separator at the bottom. For the Al signal some intensity peaks are observed. This could be an artefact of the synthesis process which uses rather coarse Al_2O_3 powder (up to 1 mm). ToF-SIMS cannot quantify the ions and only the elemental distribution should be evaluated.

Aluminum is another crucial dopant in the LLZ-Ta that is known for its mobility during the heat treatment process [175]. As Al is substituted only in the LLZ:Ta, and LCO can only have traces, it can be expected that the Al signal is higher in the LLZ:Ta areas than in the LCO areas (Fig. 4.55). However, in the FAST/SPS sample, the Al signal within the composite cathode is slightly increased compared to the LLZ:Ta separator. This effect is enhanced after the annealing process. From Li et al., it is known that Al preferentially diffuses and segregates at the LLZ grain boundaries [164]. Tsai et al. reported the importance of Al in the LLZ grain boundaries [133]. They found that high Al concentrations in the LLZ grain boundaries lead to high Li-ion conductivity. Here, apparently Al prefers to migrate towards the interphase boundaries of LCO and LLZ:Ta phases of the composite cathode (Fig. 4.55). By ToF-SIMS line scans an increase in Al signal is observed from the FAST/SPS, “as prepared”, cycled, and the recovered sample (Fig. 4.56). In the cycled composite cathode, the Al follows the Co signal and might suggest their correlation (Fig. 4.56c and d). These line scan can also be used to validate the TEM/EDX scans (Fig. 4.49) and the hypothesis of an Al↔Co exchange (section 4.2).

In the recovered composite cathode, the highest Al signal is found (Fig. 4.53h). However, the Al↔Co correlation is not as correlated as observed in the cycled sample (Fig. 4.56c to e).

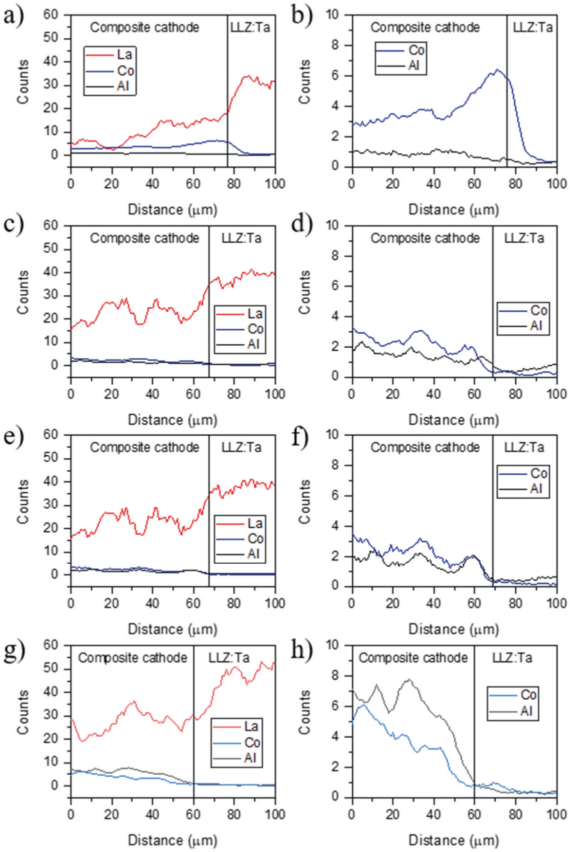

Fig. 4.56. ToF-SIMS line scans for La, Co, and Al across the composite cathode/LLZ:Ta separator interface in the: a,b) FAST/SPS, c,d) as prepared, e,f) cycled, g,h) recovered state. The images in a, e, and g show the La signal to separate the composite cathode and separator. In b, d, and h the focus is on the same area but with a focus on the distribution of Co and Al.

4.3.3. Discussion of the recovery process

The capacity of the electrochemical cycled composite cathodes is recoverable by an annealing process (Fig. 4.46).

After the annealing of the electrochemical cycled composite cathode, the interfacial impedance is reduced (Fig. 4.47), and the electrochemical performance significantly improved. This is based on two effects. First, the amorphous phase in the LLZ:Ta, observed after electrochemical cycling is crystallized as shown with TEM (Fig. 4.48 and Fig. 4.37) and Raman spectroscopy (Fig. 4.52). Second, the electrochemical driven Al↔Co exchange (described in section 4.2), leading to slightly thermodynamic unfavorable phases, is reversed. The more crystalline LLZ:Ta and the lower substituent concentration of Al in LCO and Co in LLZ:Ta lead to lower impeded LCO/LLZ:Ta interfaces and a better electrochemical performance. ToF-SIMS results suggest that after the recovery process the Al concentration within the composite cathode is highest (Fig. 4.55). While TEM/EDX indicates that Al is still within the LCO areas, the Al concentration has decreased in comparison to the cycled state (Fig. 4.49 and Fig. 4.39b). The increased Al concentration in the composite cathode can, as reported by several research groups, lead to increased grain boundary conduction between LLZ:Ta and potentially also between LCO and LLZ:Ta [21, 164, 169, 223].

Therefore, the recovery process could be considered as a process that partially reverses the electrochemical driven Al↔Co exchange and additionally leads to an accumulation of Al within the LLZ:Ta in the composite cathode and by that to increased grain boundary conduction between LLZ:Ta and potentially also between LCO and LLZ:Ta. The recovery process might not retrieve the initial state but lead to a state with similar electrochemical performance.

4.4. Polymer-ceramic composite cathode with enhanced storage capacity

4.4.1. Concept of polymer-ceramic all-solid-state Lithium battery

The electrochemical stability of ASSLBs is improved by the concept of polymer-ceramic ASSLBs [115, 224]. A polymer-ceramic ASSLB combines the high electrochemical stability of a polymer-based Li battery with the high safety level of an ASSLB.

A possible battery design for an LLZ:Ta based polymer-ceramic Li battery is a dense LLZ:Ta framework on one side and a porous one on the other side (see Fig. 3.6) [115]. By this a similar cathode design as presented in sections 4.1 to 4.3 is realized. This design is beneficial for enhanced storage capacity (Fig. 4.29) and would still separate the polymer electrolyte from the anode, guaranteeing the high safety level of solid-state Li batteries.

Commonly the polymer-ceramic ASSLBs are constructed based on a LLZ separator with a dense and porous side that are manufactured by tape-casting [115, 224]. The tape-casting process is not straight forward as it requires the preparation of a slurry with organic solvents. Furthermore, the grain morphology has a major impact on the final LLZ microstructure [109, 169]. Afterwards, the tape-casted LLZ separator is conventionally sintered and grain growth and loss of volatile elements, such as Li, occurs. The sintered LLZ separator is then infiltrated by CAM solution [224]. After drying the CAM solution the polymer electrolyte is added.

In a powder-based process, co-sintering the CAM and LLZ simplifies the manufacturing. Another advantage is that the porous LLZ framework is stabilized by the CAM which allows to reduce the LLZ amount in the porous framework in order to achieve higher CAM loadings [25]. However, the high sintering temperature and long dwell time for the sintering of garnet-based LLZ electrolyte lead to reactions with CAMs and hamper the manufacturing of composite cathodes [3].

A reduction in sintering temperature and dwell time can be achieved by advanced sintering techniques, such as FAST/SPS (section 4.1.4). This shortens the required processing times due to faster heating and an increased sintering rate and reduces the sintering temperatures. Due to that less grain growth is observed (section 4.1.7.1), and the loss of volatile elements is reduced. The porosity is tunable by the applied mechanical pressure during FAST/SPS (Fig. 4.9). However, for low applied mechanical pressure during FAST/SPS the LLZ:Ta separator would be porous and could lead to Li dendrite formation. In this case, either the composite cathode has to be sintered on a dense LLZ:Ta separator or attached by polymer electrolyte on a dense sintered LLZ:Ta separator. Here, the latter option was chosen and the polymer-ceramic ASSLB is prepared by attaching the porous composite cathode with the help of the MEEP (poly[bis(2-

(2-MethoxyEthoxy)Ethoxy)Phosphazene]) polymer onto a dense LLZ:Ta separator (Fig. 3.6). The fully inorganic ASSLB is prepared as a half-cell with a porous LLZ:Ta separator, which detrimental for cycling but allows to measure the total impedance.

4.4.1.1. Characterization of the polymer-ceramic ASSLB

EIS measurements have been performed for the polymer-ceramic ASSLB with a LCO/LLZ:Ta composite cathode infiltrated by MEEP polymer and the impedance spectrum was compared to the impedance spectrum of an all ceramic ASSLB with a porous LCO/LLZ:Ta composite cathode (Fig. 4.57a). The density of the composite cathode was, in both cases, approximately 80 %. Both EIS spectra have a high frequency intersection with the x-axis and indicate one semicircle at the high frequencies and one at medium frequencies, and the low frequencies Li-ion diffusion either in the anode and/or the Au layer (see section 4.2.1.2). The EIS spectra were fitted with the equivalent circuit shown in Fig. 4.57b. However, it was not possible to separate the LCO or LLZ:Ta interfaces with MEEP from the LLZ:Ta grain boundary impedance, and the LCO/LLZ:Ta interface by the fitted capacities (Tab. 4.8). Therefore, only the total impedance of the ceramic and polymer-ceramic ASSLB can be compared.

The porosity in the LCO/LLZ:Ta composite cathode leads to a high total impedance (Fig. 4.57), as for a similar dense composite cathode (shown in sections 4.1.9.2 and 4.2.1.2) a significantly lower total impedance was observed. The same observation is achieved by infiltration of MEEP polymer into the porous composite cathode, the total impedance of the ASSLB was reduced from 1061 Ω cm^2 to 344 Ω cm^2. This shows that the MEEP polymer was successfully infiltrated into the pores of the composite cathode, and that the infiltrated MEEP polymer can increase the total ionic conductivity in the composite cathode.

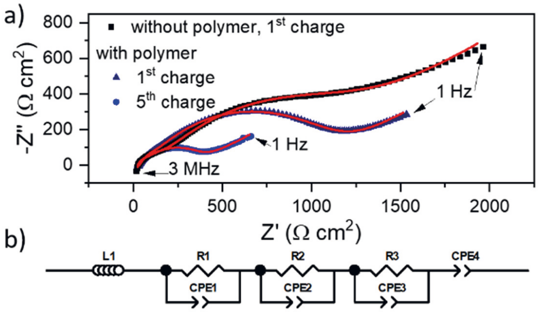

Fig. 4.57. a) EIS spectra of the ASSLB with the porous composite cathode and with the MEEP polymer infiltrated composite cathode after the first and fifth charge at 80 °C. b) The equivalent circuit for fitting (L: inductor, R: ohmic resistor, and CPE: constant phase element).

Tab. 4.8. Fitting parameter for the fully inorganic and the polymer-ceramic ASSLB after the first and fifth charge at 80 °C. The equivalent circuit is shown in Fig. 4.57b.

Sample	**fully inorganic ASSLB, 1st charge**	**polymer-ceramic ASSLB, 1st charge**	**polymer-ceramic ASSLB, 5th charge**
Area (cm^2)	1.13	1.13	1.13
*L*1 (H)	2.07E-06	7.49E-07	5.64E-07
*R*1 (Ω)	22.59	22.27	32.43
CPE1: Q_0 (Ω^{-1} s^n)	1.34E-09	3.75E-11	1.21E-06
CPE1: n	1.00	0.91	0.47
*C*1	9.01E-10	4.70E-12	8.75E-12
*R*2 (Ω)	114.1	30.60	51.17
CPE2: Q_0 (Ω^{-1} s^n)	1.23E-05	3.18E-06	3.91E-06
CPE2: n2	0.68	0.88	0.41
*C*2	4.90E-07	8.86E-07	1.12E-11
*R*3(Ω)	925.20	292.30	979.6
CPE3: Q_0 (Ω^{-1} s^n)	1.09E-4	4.44E-05	4.40E-07
CPE3: n3	0.61	0.63	0.0041
*C*3	2.06E-05	2.89E-06	3.79E-12
CPE4: Q_0 (Ω^{-1} s^n)	1.07E-3	3.33E-03	4.15E-05
CPE4: n4	0.38	0.32	0.0068

The increased total ionic conductivity allows the electrochemical cycling of the polymer-ceramic ASSLB (Fig. 4.58a), which was not possible for the porous fully inorganic one as the potential immediately jumped to 3.4 V. This should be related to the thickness of the composite cathode as Tsai et al. reported the functionality of a thin (30 µm) porous (around 20 %) LCO/LLZ:Ta composite cathode [18].

The MEEP polymer infiltrated porous composite cathode is able to provide a high initial charge capacity of 3.4 mAh cm^{-2} or 64 % LCO utilization, although the ASSLB was not fully charged. The cut-off voltage was chosen as for porous LCO/LLZ:Ta composite cathodes fracturing of LCO/LLZ:Ta interface due to volume changes within the LCO (Fig. 4.58a) was reported [62]. The first discharge shows a high capacity, which however, is much lower than the initial charge capacity. Nevertheless, the achieved areal capacity is comparable to the dense LCO/LLZ:Ta composite cathodes presented in sections 4.1.9.2 and 4.2.1.2 and higher than for composite cathodes with similar configuration reported in the literature [18, 57].

The charge and discharge capacity decreases continuously, which is attributed to an increase in total impedance and thereby the rapid potential increase during charge. Although, it is not possible to separate all impedances (bulk and grain boundary of LLZ:Ta, and the LCO/LLZ:Ta, LCO/MEEP polymer, and LLZ:Ta/MEEP polymer interfaces, Tab. 4.8), it can be estimated that the majority of the impedance increase is due to the interfaces, as was reported in sections 4.1.9.2 and 4.2.1.2. The bulk impedance of LLZ:Ta is stable within the measuring inaccuracies and the grain boundary impedance is only slightly increased. A degradation of the MEEP polymer can be excluded as it is reported to be stable vs LCO or LLZ:Ta at the used potential window and temperature [225-229].

To get a more detailed understanding of the reason for the interfacial impedance increase, the polymer-ceramic ASSLB was dismounted and characterized by SEM (Fig. 4.58b). The SEM cross section shows homogeneously mixed LLZ:Ta and LCO grains coated with MEEP polymer. However, the MEEP polymer only forms a thin layer around the LCO and LLZ:Ta grains. Most of the pores remain open.

During the electrochemical cycling, cracks are formed and are clearly visible between LCO and LLZ:Ta and also LCO grains. Within these cracks no MEEP polymer is detected. The cracks must, therefore, have formed during the electrochemical cycling due to the volume changes of LCO. As this leads to a loss of interface, the impedance increases, and the cell capacity fades.

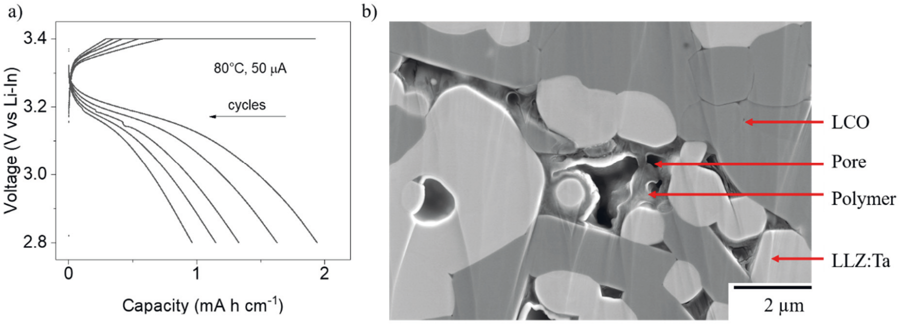

Fig. 4.58. Charge and discharge of a hybrid ASSLB with a porous composite cathode infiltrated with MEEP polymer in a). The cross-sectional SEM after electrochemical cycling in b) shows the infiltration of the polymer into the pores but also lost contact between LCO and LLZ:Ta areas.

Fig. 4.58b shows, the MEEP polymer infiltrated into the porous composite cathode is low. The infiltrated amount of MEEP polymer is unknown. Hence, one possible solution to avoid the cell degradation could be a higher infiltration of the composite cathode with MEEP polymer. This would result in thicker polymer layer around the grains and ensure better Li-ion conductivity. The higher polymer loading would also be able to “heal” the formed cracks. After polymerization, the MEEP polymer is not fully solidified yet but hardens during electrochemical cycling [134, 135]. During the first cycles, a high charge and discharge current could be applied during the first cycle to break the weak LCO/LLZ:Ta, LCO/LCO, and LLZ:Ta/LLZ:Ta grain boundaries intentionally. The viscous polymer might be able to diffuse into these cracks and ensure an ionic conductivity, after which capacity fading might stop

For the optimization of the infiltration process it is relevant to find the most suitable porosity. For example the composite cathode with only 5 % porosity did not show any infiltrated MEEP polymer (Fig. 4.59), as at such density levels usually only closed porosity is observed. Therefore, the composite cathode would be a fully inorganic one and show the behavior as described in section 4.2.1.

Furthermore, the viscosity of the polymer electrolyte solution is essential. Lower viscosity might benefit the infiltration of the polymer into the pores. Additionally, applying vacuum during the infiltration process could also be advisable.

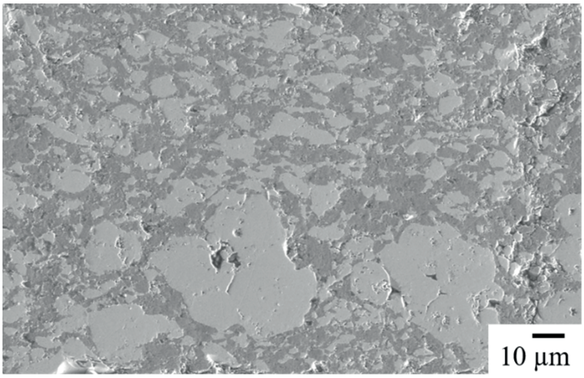

Fig. 4.59. A dense LCO/LLZ:Ta composite cathode with 5 % porosity does not show any infiltrated MEEP polymer due to closed porosity. The LCO is in the darker areas and the LLZ: Ta in lighter ones.

4.4.1.2. Conclusion of the polymer-ceramic ASSLB concept

Porous LCO/LLZ:Ta composite cathodes can be manufactured by FAST/SPS (Fig. 4.9). The developed FAST/SPS process offers the tailoring of the porosity up to 20 % of the composite cathodes (Fig. 4.10) which can help the infiltration process with polymer to lower the total impedance (Fig. 4.57) and offer the chance of high energy density in polymer-ceramic ASSLBs. The polymer electrolyte loading could play a crucial role in maintaining the electrochemical properties. The shown electrochemical data proves that garnet-based polymer-ceramic ASSLBs can be successfully prepared with low total impedance (Fig. 4.57) and high capacity (Fig. 4.58).

To further improve the electrochemical performance, the preparation process requires further optimization. First, the pores have to be filled up completely with polymer electrolyte. Second, the pores and the pore network have to be optimized. This is possible via a higher porosity or by designed pore structures. Third, the polymer is known to be viscous within the first cycles and can potentially heal a fractured LCO/LLZ:Ta interface. The fracturing of weak interfaces should be initiated by higher currents in the first cycles. The rather viscous polymer infiltrates into the cracks and "heal" them by forming new electrochemically conductive contacts.

5. Summary and Conclusion

Until now, the development of garnet LLZ-based ASSLBs was hampered by integration problems in electrochemical cells. Preliminary material characterization revealed that LCO and LLZ:Ta are the most suitable CAM/solid electrolyte combination. Based on a high-pressure assisted FAST/SPS process, a dense composite cathode with clean interfaces and without sintering aids was prepared. After a subsequent annealing process, the interface was crystallized and had low impedance.

ASSLBs based on such a composite cathode showed a very high areal capacity of more than 4 mA h cm^{-2} and a high LCO utilization in the first discharge which proves that a true working bulk composite cathode was prepared. However, the stability of the electrochemical performance still needs to be optimized. An increase in LCO/LLZ:Ta interfacial impedance within a few cycles leads to a rapid capacity fading. A thorough structural characterization of the cycled composite cathode exposed that the interface contact is unbroken, and cracking can be excluded as cause of the degradation. However, the interface appeared to have formed a third phase between LCO and LLZ:Ta after cycling. This was linked to an elemental exchange of Al- and Co-ions. The Al-ion diffusion from LLZ:Ta into LCO is most likely negligible for the electrochemical performance. But the Co-ions replacing the Al-ions in LLZ:Ta can lead to the formation of less conductive LLZ:Ta phases. The electrochemically active Co-ions can be reduced and the accumulation of Li-ions to keep the charge balance, can lead to stresses within the LLZ:Ta and cause a disordered lattice. Disordered LLZ:Ta has a significantly reduced Li-ion conductivity and in combination with Co substituted LLZ:Ta provides an excellent explanation for the rapid increase in interfacial impedance and drop in cycle capacity. The whole process is visualized in Fig. 5.1.

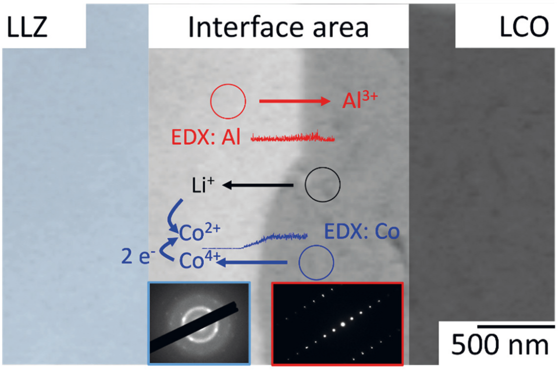

Fig. 5.1. Visualization of the Al-Co exchange during electrochemical cycling.

Thermodynamic simulation exposed the newly formed Co substituted and potentially Li rich LLZ:Ta phase to be less thermodynamically favorable than the pure phased LLZ:Ta. After cycling the composite cathode was extracted from the cell and heat treated to recover the initial phases. The electrochemical performance of the recovered composite cathode is comparable with the as prepared composite cathode. Based on the thermodynamic simulation it is clear that the degradation process is reversible and that potentially an electrochemically induced Al↔Co exchange, causing disordering of the LLZ:Ta leads to the fading electrochemical performance.

In order to overcome the presented limitations, initial experiments on an alternative polymer-ceramic (solid and polymer electrolyte) ASSLB have been started.

6. Outlook

Future work should focus on finding more suitable CAM and solid electrolyte combinations to increase and obtain more reliable battery performance. As the degradation process is linked to the Al↔Co exchange, a suitable CAM might be Co-free. Co-free CAM are already in the focus of researchers [87, 88], and if the thermal stability is high enough, such Co-free CAMs could replace LCO and thus eliminate the degradation based on Al↔Co exchange. Also, operando analysis during electrochemical characterization could provide a more detailed insight into the degradation process and if it occurs during charge or discharge and at which potential the degradation is initiated.

The new developed Ultra-fast High-temperature Sintering (UHS) method is a promising alternative to the presented FAST/SPS processing [230, 231]. UHS allows the high densification and sintering within seconds and can enable CAM/solid electrolyte combinations which were unsuitable so far and pave the way for a completely new generation of composite cathodes.

Potentially, it can also be of relevance to focus on different solid electrolytes for the cathode side. LLZ, while being one of the most relevant ceramic based solid electrolytes, could be replaced to simplify the processing. $Li_{1.5}Al_{0.5}Ti_{1.5}(PO_4)_3$ (LATP) has similar properties than LLZ and could be a suitable candidate if the side reactions of LATP and CAMs are circumvented [232, 233].

Furthermore, the new battery concept described in section 4.4 could open new opportunities for garnet LLZ-based ASSLBs. Optimization of the solid/polymer interface for the polymer-ceramic ASSLB might help overcome the Al-Co exchange-based degradation mechanism by providing alternative stress absorption pathways, and utilize the beneficial electrochemical properties of the polymer electrolyte for high performance polymer-ceramic ASSLBs. Also, an optimization of the infiltration process and the mixing ratio, as well as the porosity in the composite cathode can enhance the electrochemical cycling stability and the increase the full cell capacity.

References

[1] Y. Xiao, Y. Wang, S.-H. Bo, J.C. Kim, L.J. Miara, G. Ceder, Nature Reviews Materials, 5 (2020) 105-126.
[2] J. Janek, W.G. Zeier, Nature Energy, 1 (2016) 16141.
[3] C. Wang, K. Fu, S.P. Kammampata, D.W. McOwen, A.J. Samson, L. Zhang, G.T. Hitz, A.M. Nolan, E.D. Wachsman, Y. Mo, V. Thangadurai, L. Hu, Chemical Reviews, 120 (2020) 4257-4300.
[4] N. Zhao, W. Khokhar, Z. Bi, C. Shi, X. Guo, L.-Z. Fan, C.-W. Nan, Joule, 3 (2019) 1190-1199.
[5] J.M. Tarascon, M. Armand, Nature, 414 (2001) 359-367.
[6] M. Rahimi, Batteries, 7 (2021) 8.
[7] T. Chen, Y. Jin, H. Lv, A. Yang, M. Liu, B. Chen, Y. Xie, Q. Chen, Transactions of Tianjin University, 26 (2020) 208-217.
[8] Y. Xiao, L.J. Miara, Y. Wang, G. Ceder, Joule, 3 (2019) 1252-1275.
[9] Y. Ren, K. Chen, R. Chen, T. Liu, Y. Zhang, C.-W. Nan, Journal of the American Ceramic Society, 98 (2015) 3603-3623.
[10] D. Wang, C. Zhu, Y. Fu, X. Sun, Y. Yang, Advanced Energy Materials, 10 (2020) 2001318.
[11] A. Banerjee, X. Wang, C. Fang, E.A. Wu, Y.S. Meng, Chemical Reviews, 120 (2020) 6878-6933.
[12] T. Famprikis, P. Canepa, J.A. Dawson, M.S. Islam, C. Masquelier, Nature Materials, 18 (2019) 1278-1291.
[13] M. Rawlence, I. Garbayo, S. Buecheler, J.L.M. Rupp, Nanoscale, 8 (2016) 14746-14753.
[14] V. Thangadurai, S. Narayanan, D. Pinzaru, Chemical Society Reviews, 43 (2014) 4714-4727.
[15] L. Miara, A. Windmuller, C.L. Tsai, W.D. Richards, Q.L. Ma, S. Uhlenbruck, O. Guillon, G. Ceder, ACS Applied Materials & Interfaces, 8 (2016) 26842-26850.
[16] Y. Ren, T. Liu, Y. Shen, Y. Lin, C.-W. Nan, Journal of Materiomics, 2 (2016) 256-264.
[17] A.M. Laptev, H. Zheng, M. Bram, M. Finsterbusch, O. Guillon, Materials Letters, 247 (2019) 155-158.
[18] C.-L. Tsai, Q. Ma, C. Dellen, S. Lobe, F. Vondahlen, A. Windmüller, D. Grüner, H. Zheng, S. Uhlenbruck, M. Finsterbusch, F. Tietz, D. Fattakhova-Rohlfing, H.P. Buchkremer, O. Guillon, Sustainable Energy & Fuels, (2019) 280-291.
[19] R. Pfenninger, M. Struzik, I. Garbayo, E. Stilp, J.L.M. Rupp, Nature Energy, 4 (2019) 475-483.
[20] S.P. Woo, W. Lee, Y.S. Yoon, Journal of the Korean Physical Society, 73 (2018) 1019-1024.
[21] C.-L. Tsai, E. Dashjav, E.-M. Hammer, M. Finsterbusch, F. Tietz, S. Uhlenbruck, H.P. Buchkremer, Journal of Electroceramics, 35 (2015) 25-32.
[22] F. Han, J. Yue, C. Chen, N. Zhao, X. Fan, Z. Ma, T. Gao, F. Wang, X. Guo, C. Wang, Joule, 2 (2018) 497-508.
[23] J. van den Broek, S. Afyon, J.L.M. Rupp, Advanced Energy Materials 6(2016) 1600736.
[24] C. Shao, Z. Yu, H. Liu, Z. Zheng, N. Sun, C. Diao, Electrochimica Acta, 225 (2017) 345-349.
[25] M. Finsterbusch, T. Danner, C.-L. Tsai, S. Uhlenbruck, A. Latz, O. Guillon, ACS Applied Materials & Interfaces, 10 (2018) 22329-22339.
[26] J. Wakasugi, H. Munakata, K. Kanamura, Electrochemistry, 85 (2017) 77-81.
[27] K. Park, B.-C. Yu, J.-W. Jung, Y. Li, W. Zhou, H. Gao, S. Son, J.B. Goodenough, Chemistry of Materials, 28 (2016) 8051-8059.

[28] M. Bram, A. Laptev, T. Prasad Mishra, K. Nur, M. Kindelmann, M. Ihrig, J. Pereira da Silva, R. Steinert, H.-P. Buchkremer, A. Litnovsky, F. Klein, J. Gonzalez-Julian, O. Guillon, Advanced Engineering Materials, 22 (2020) 2000051.
[29] A.J. Samson, K. Hofstetter, S. Bag, V. Thangadurai, Energy & Environmental Science, 12 (2019) 2957-2975.
[30] K. Tadanaga, R. Takano, T. Ichinose, S. Mori, A. Hayashi, M. Tatsumisago, Electrochemistry Communications, 33 (2013) 51-54.
[31] H. Zhu, J. Liu, Journal of Power Sources, 391 (2018) 10-25.
[32] O. Guillon, J. Gonzalez-Julian, B. Dargatz, T. Kessel, G. Schierning, J. Räthel, M. Herrmann, Advanced Engineering Materials, 16 (2014) 830-849.
[33] J. Langer, M.J. Hoffmann, O. Guillon, Journal of the American Ceramic Society, 94 (2011) 24-31.
[34] R. Kali, A. Mukhopadhyay, Journal of Power Sources, 247 (2014) 920-931.
[35] J.E. Garay, Annual Review of Materials Research, 40 (2010) 445-468.
[36] Y. Zhang, F. Chen, R. Tu, Q. Shen, L. Zhang, Journal of Power Sources, 268 (2014) 960-964.
[37] S.P. Kammampata, R.H. Basappa, T. Ito, H. Yamada, V. Thangadurai, ACS Applied Energy Materials, 2 (2019) 1765-1773.
[38] X. Wei, J. Rechtin, E. Olevsky, Metals, 7 (2017) 372.
[39] R. German, Sintering theory and practice, Wiley-VCH, 1996.
[40] J.S. Reed, Principles of ceramics processing, 2nd ed., John Wiley & Sons, Inc. (US), 1995.
[41] M.N. Rahaman, Ceramic processing and sintering, 2. ed. ed., Dekker, Dekker New York [u.a.] :, 2003.
[42] C. Herring, Journal of Applied Physics, 21 (1950) 301-303.
[43] J. Selsing, Journal of the American Ceramic Society, 44 (1961) 419-419.
[44] R.K. Bordia, G.W. Scherer, Acta Metallurgica, 36 (1988) 2393-2397.
[45] R.K. Bordia, G.W. Scherer, Acta Metallurgica, 36 (1988) 2399-2409.
[46] R.K. Bordia, G.W. Scherer, Acta Metallurgica, 36 (1988) 2411-2416.
[47] G.W. Scherer, Journal of the American Ceramic Society, 70 (1987) 719-725.
[48] U. Anselmi-Tamburini, S. Gennari, J.E. Garay, Z.A. Munir, Materials Science and Engineering: A, 394 (2005) 139-148.
[49] P. Cavaliere, B. Sadeghi, A. Shabani, Spark Plasma Sintering: Process Fundamentals, in: P. Cavaliere (Ed.) Spark Plasma Sintering of Materials: Advances in Processing and Applications, Springer International Publishing, Cham, 2019, pp. 3-20.
50] T. Takeuchi, M. Tabuchi, A. Nakashima, T. Nakamura, Y. Miwa, H. Kageyama, K. Tatsumi, Journal of Power Sources, 146 (2005) 575-579.
[51] T. Takeuchi, M. Tabuchi, A. Nakashima, H. Kageyama, K. Tatsumi, Electrochemical and Solid-State Letters, 8 (2005) A195.
[52] Z.-Y. Hu, Z.-H. Zhang, X.-W. Cheng, F.-C. Wang, Y.-F. Zhang, S.-L. Li, Materials & Design, 191 (2020) 108662.
[53] M. Ihrig, M. Finsterbusch, C.-L. Tsai, A.M. Laptev, C.-h. Tu, M. Bram, Y.J. Sohn, R. Ye, S. Sevinc, S.-k. Lin, D. Fattakhova-Rohlfing, O. Guillon, Journal of Power Sources, 482 (2021) 228905.
[54] T.P. Mishra, A.M. Laptev, M. Ziegner, S.K. Sistla, A. Kaletsch, C. Broeckmann, O. Guillon, M. Bram, Materials, 13 (2020) 3184.
[55] A.M. Laptev, M. Bram, K. Vanmeensel, J. Gonzalez-Julian, O. Guillon, Journal of Materials Processing Technology, 262 (2018) 326-339.
[56] S.K. Sistla, T.P. Mishra, Y.B. Deng, A. Kaletsch, M. Bram, C. Broeckmann, Journal of the American Ceramic Society, (2021) 1-19.

[57] S.-W. Baek, J.-M. Lee, T.Y. Kim, M.-S. Song, Y. Park, Journal of Power Sources, 249 (2014) 197-206.
[58] H. Yamada, T. Ito, R. Hongahally Basappa, Electrochimica Acta, 222 (2016) 648-656.
[59] T. Okumura, T. Takeuchi, H. Kobayashi, Solid State Ionics, 288 (2016) 248-252.
[60] A. Aboulaich, R. Bouchet, G. Delaizir, V. Seznec, L. Tortet, M. Morcrette, P. Rozier, J.-M. Tarascon, V. Viallet, M. Dollé, Advanced Energy Materials, 1 (2011) 179-183.
[61] B.M. Gallant, Joule, 4 (2020) 2254-2256.
[62] R. Koerver, W. Zhang, L. de Biasi, S. Schweidler, A.O. Kondrakov, S. Kolling, T. Brezesinski, P. Hartmann, W.G. Zeier, J. Janek, Energy & Environmental Science, 11 (2018) 2142-2158.
[63] N. Nitta, F. Wu, J.T. Lee, G. Yushin, Materials Today, 18 (2015) 252-264.
[64] C. Liu, Z.G. Neale, G. Cao, Materials Today, 19 (2016) 109-123.
[65] P. Zhu, D. Gastol, J. Marshall, R. Sommerville, V. Goodship, E. Kendrick, Journal of Power Sources, 485 (2021) 229321.
[66] P. Verma, P. Maire, P. Novák, Electrochimica Acta, 55 (2010) 6332-6341.
[67] J.B. Goodenough, K.-S. Park, Journal of the American Chemical Society, 135 (2013) 1167-1176.
[68] F. Jiang, P. Peng, Scientific Reports, 6 (2016) 32639.
[69] X. Judez, G.G. Eshetu, C. Li, L.M. Rodriguez-Martinez, H. Zhang, M. Armand, Joule, 2 (2018) 2208-2224.
[70] J. Schnell, T. Günther, T. Knoche, C. Vieider, L. Köhler, A. Just, M. Keller, S. Passerini, G. Reinhart, Journal of Power Sources, 382 (2018) 160-175.
[71] W. Xu, J. Wang, F. Ding, X. Chen, E. Nasybulin, Y. Zhang, J.-G. Zhang, Energy & Environmental Science, 7 (2014) 513-537.
[72] D. Aurbach, E. Zinigrad, Y. Cohen, H. Teller, Solid State Ionics, 148 (2002) 405-416.
[73] S. Yu, R.D. Schmidt, R. Garcia-Mendez, E. Herbert, N.J. Dudney, J.B. Wolfenstine, J. Sakamoto, D.J. Siegel, Chemistry of Materials, 28 (2016) 197-206.
[74] X. Liang, Q. Pang, I.R. Kochetkov, M.S. Sempere, H. Huang, X. Sun, L.F. Nazar, Nature Energy, 2 (2017) 17119.
[75] A.L. Santhosha, L. Medenbach, J.R. Buchheim, P. Adelhelm, Batteries & Supercaps, 2 (2019) 524-529.
[76] S.A. Webb, L. Baggetto, C.A. Bridges, G.M. Veith, Journal of Power Sources, 248 (2014) 1105-1117.
[77] S. Choudhury, Z. Tu, S. Stalin, D. Vu, K. Fawole, D. Gunceler, R. Sundararaman, L.A. Archer, Angewandte Chemie International Edition, 56 (2017) 13070-13077.
[78] C.J. Wen, R.A. Huggins, Materials Research Bulletin, 15 (1980) 1225-1234.
[79] C.E.L. Foss, S. Müssig, A.M. Svensson, P.J.S. Vie, A. Ulvestad, J.P. Mæhlen, A.Y. Koposov, Scientific Reports, 10 (2020) 13193.
[80] D. Ma, Z. Cao, A. Hu, Nano-Micro Letters, 6 (2014) 347-358.
[81] C.-J. Huang, B. Thirumalraj, H.-C. Tao, K.N. Shitaw, H. Sutiono, T.T. Hagos, T.T. Beyene, L.-M. Kuo, C.-C. Wang, S.-H. Wu, W.-N. Su, B.J. Hwang, Nature Communications, 12 (2021) 1452.
[82] Z. Xie, Z. Wu, X. An, X. Yue, J. Wang, A. Abudula, G. Guan, Energy Storage Materials, 32 (2020) 386-401.
[83] C.M.M. Julien, A.; Zaghib, K.; Groult, H. , Inorganics (2014) 132-154.
[84] N. Yabuuchi, Y. Kawamoto, R. Hara, T. Ishigaki, A. Hoshikawa, M. Yonemura, T. Kamiyama, S. Komaba, Inorganic Chemistry, 52 (2013) 9131-9142.
[85] Y. Gong, J. Zhang, L. Jiang, J.-A. Shi, Q. Zhang, Z. Yang, D. Zou, J. Wang, X. Yu, R. Xiao, Y.-S. Hu, L. Gu, H. Li, L. Chen, Journal of the American Chemical Society, 139 (2017) 4274-4277.

[86] C.M. Julien, A. Mauger, O.M. Hussain, Materials (Basel), 12 (2019) 2687.
[87] F. Wu, G.-T. Kim, M. Kuenzel, H. Zhang, J. Asenbauer, D. Geiger, U. Kaiser, S. Passerini, Advanced Energy Materials, 9 (2019) 1902445.
[88] J. Asenbauer, J.R. Binder, F. Mueller, M. Kuenzel, D. Geiger, U. Kaiser, S. Passerini, D. Bresser, ChemSusChem, 13 (2020) 3504-3513.
[89] C. Yin, H. Zhou, Z. Yang, J. Li, ACS Applied Materials & Interfaces, 10 (2018) 13625-13634.
[90] A. Manthiram, Nature Communications, 11 (2020) 1550.
[91] N. Mohamed, N.K. Allam, RSC Advances, 10 (2020) 21662-21685.
[92] K. Kang, Y.S. Meng, J. Bréger, C.P. Grey, G. Ceder, Science, 311 (2006) 977-980.
[93] S.-H. Yu, X. Feng, N. Zhang, J. Seok, H.D. Abruña, Accounts of Chemical Research, 51 (2018) 273-281.
[94] F. Wu, G. Yushin, Energy & Environmental Science, 10 (2017) 435-459.
[95] D. Karabelli, K.P. Birke, M. Weeber, Batteries, 7 (2021) 18.
[96] A. Manthiram, X. Yu, S. Wang, Nature Reviews Materials, 2 (2017) 16103.
[97] X. Zhang, Y. Yang, Z. Zhou, Chemical Society Reviews, 49 (2020) 3040-3071.
[98] M. Xu, M.S. Park, J.M. Lee, T.Y. Kim, Y.S. Park, E. Ma, Physical Review B, 85 (2012) 052301.
[99] C.A. Geiger, E. Alekseev, B. Lazic, M. Fisch, T. Armbruster, R. Langner, M. Fechtelkord, N. Kim, T. Pettke, W. Weppner, Inorganic Chemistry, 50 (2011) 1089-1097.
[100] S. Adams, R.P. Rao, Journal of Materials Chemistry, 22 (2012) 1426-1434.
[101] J. Awaka, N. Kijima, H. Hayakawa, J. Akimoto, Journal of Solid State Chemistry, 182 (2009) 2046-2052.
[102] A. Logéat, T. Köhler, U. Eisele, B. Stiaszny, A. Harzer, M. Tovar, A. Senyshyn, H. Ehrenberg, B. Kozinsky, Solid State Ionics, 206 (2012) 33-38.
[103] M. Matsui, K. Takahashi, K. Sakamoto, A. Hirano, Y. Takeda, O. Yamamoto, N. Imanishi, Dalton Transactions, 43 (2014) 1019-1024.
[104] A.A. Hubaud, D.J. Schroeder, B. Key, B.J. Ingram, F. Dogan, J.T. Vaughey, Journal of Materials Chemistry A, 1 (2013) 8813-8818.
[105] L. Dhivya, R. Murugan, ACS Applied Materials & Interfaces, 6 (2014) 17606-17615.
[106] E. Rangasamy, J. Wolfenstine, J. Sakamoto, Solid State Ionics, 206 (2012) 28-32.
[107] T. Thompson, J. Wolfenstine, J.L. Allen, M. Johannes, A. Huq, I.N. David, J. Sakamoto, Journal Materials Chemistry A, 2 (2014) 13431-13436.
[108] G. Larraz, A. Orera, M.L. Sanjuán, Journal of Materials Chemistry A, 1 (2013) 11419-11428.
[109] L. Cheng, E.J. Crumlin, W. Chen, R. Qiao, H. Hou, S. Franz Lux, V. Zorba, R. Russo, R. Kostecki, Z. Liu, K. Persson, W. Yang, J. Cabana, T. Richardson, G. Chen, M. Doeff, Physical Chemistry Chemical Physics, 16 (2014) 18294-18300.
[110] T. Kato, T. Hamanaka, K. Yamamoto, T. Hirayama, F. Sagane, M. Motoyama, Y. Iriyama, Journal of Power Sources, 260 (2014) 292-298.
[111] K.H. Kim, Y. Iriyama, K. Yamamoto, S. Kumazaki, T. Asaka, K. Tanabe, C.A.J. Fisher, T. Hirayama, R. Murugan, Z. Ogumi, Journal of Power Sources, 196 (2011) 764-767.
[112] M. Kotobuki, K. Kanamura, Y. Sato, T. Yoshida, Journal of Power Sources, 196 (2011) 7750-7754.
[113] M. Kotobuki, H. Munakata, K. Kanamura, Y. Sato, T. Yoshida, Journal of the Electrochemical Society, 157 (2010) A1076-A1079.
[114] X. Chen, W. He, L.-X. Ding, S. Wang, H. Wang, Energy & Environmental Science, 12 (2019) 938-944.
[115] X. Yu, A. Manthiram, Energy Storage Materials, 34 (2021) 282-300.

[116] Y. Li, X. Chen, A. Dolocan, Z. Cui, S. Xin, L. Xue, H. Xu, K. Park, J.B. Goodenough, Journal of the American Chemical Society, 140 (2018) 6448-6455.
[117] K.J. Kim, J.L.M. Rupp, Energy & Environmental Science, 13 (2020) 4930-4945.
[118] C.-L. Tsai, S. Yu, H. Tempel, H. Kungl, R.-A. Eichel, Materials Technology, 35 (2020) 656-674.
[119] S. Ohta, T. Kobayashi, J. Seki, T. Asaoka, Journal of Power Sources, 202 (2012) 332-335.
[120] F. Han, Y. Zhu, X. He, Y. Mo, C. Wang, Advanced Energy Materials, 6 (2016) 1501590.
[121] G. Vardar, W.J. Bowman, Q. Lu, J. Wang, R.J. Chater, A. Aguadero, R. Seibert, J. Terry, A. Hunt, I. Waluyo, D.D. Fong, A. Jarry, E.J. Crumlin, S.L. Hellstrom, Y.-M. Chiang, B. Yildiz, Chemistry of Materials, 30 (2018) 6259-6276.
[122] Z. Wang, D. Santhanagopalan, W. Zhang, F. Wang, H.L. Xin, K. He, J. Li, N. Dudney, Y.S. Meng, Nano Letters, 16 (2016) 3760-3767.
[123] F. Chen, J. Li, Z. Huang, Y. Yang, Q. Shen, L. Zhang, The Journal of Physical Chemistry C, 122 (2018) 1963-1972.
[124] X. Han, Y. Gong, K. Fu, X. He, G.T. Hitz, J. Dai, A. Pearse, B. Liu, H. Wang, G. Rubloff, Y. Mo, V. Thangadurai, E.D. Wachsman, L. Hu, Nature Materials, 16 (2016) 572.
[125] G.T. Hitz, D.W. McOwen, L. Zhang, Z. Ma, Z. Fu, Y. Wen, Y. Gong, J. Dai, T.R. Hamann, L. Hu, E.D. Wachsman, Materials Today, 22 (2019) 50-57.
[126] L. Bendersky, H. Tan, K. Bharathi Karuppanan, Z.-P. Li, A. Johnston-Peck, Crystals, 7 (2017).
[127] A. Junji, T. Akira, K. Kunimitsu, K. Norihito, I. Yasushi, A. Junji, Chemistry Letters, 40 (2011) 60-62.
[128] S. Panahian Jand, P. Kaghazchi, MRS Communications, 8 (2018) 591-596.
[129] N. Zhang, X. Long, Z. Wang, P. Yu, F. Han, J. Fu, G. Ren, Y. Wu, S. Zheng, W. Huang, C. Wang, H. Li, X. Liu, ACS Applied Energy Materials, 1 (2018) 5968-5976.
[130] Y. Zhu, X. He, Y. Mo, Journal of Materials Chemistry A, 4 (2016) 3253-3266.
[131] Z. Wang, J.Z. Lee, H.L. Xin, L. Han, N. Grillon, D. Guy-Bouyssou, E. Bouyssou, M. Proust, Y.S. Meng, Journal of Power Sources, 324 (2016) 342-348.
[132] M. Otoyama, Y. Ito, A. Hayashi, M. Tatsumisago, Journal of Power Sources, 302 (2016) 419-425.
[133] C.L. Tsai, V. Roddatis, C.V. Chandran, Q. Ma, S. Uhlenbruck, M. Bram, P. Heitjans, O. Guillon, ACS Applied Materials & Interfaces, 8 (2016) 10617-10626.
[134] Z. Wang, I. Manners, Macromolecules, 38 (2005) 5047-5054.
[135] B. Wang, E. Rivard, I. Manners, Inorganic Chemistry, 41 (2002) 1690-1691.
[136] M. Otto, Analytische Chemie, 5. Auflage ed., Wiley-VCH Verlag GmbH & Co. KGaA, Wiley-VCH Verlag GmbH & Co. KGaA Weinheim, 2019.
[137] H. Abrams, Metallography, 4 (1971) 59-78.
[138] W. Massa, W. Massa, Crystal structure determinationwith 16 tables, Springer, Springer Berlin [u.a.], 2000.
[139] Y.-B.P. Kwan, J.R. Alcock, Journal of Materials Science, 37 (2002) 2557-2561.
[140] R. Inada, K. Kusakabe, T. Tanaka, S. Kudo, Y. Sakurai, Solid State Ionics, 262 (2014) 568-572.
[141] D.B. Williams, C.B. Carter, Transmission electron microscopya textbook for materials science, 2. ed. ed., Springer, New York [u.a.].
[142] G.G. Hoffmann, Raman spectroscopy. 1. Principles and applications in chemistry, physics, materials science, and biology. 1. Principles, Momentum Press, 2019.
[143] K. Hara, T.-a. Yano, K. Suzuki, M. Hirayama, T. Hayashi, R. Kanno, M. Hara, Analytical Sciences, 33 (2017) 853-858.

[144] Y. Matsuda, N. Kuwata, T. Okawa, A. Dorai, O. Kamishima, J. Kawamura, Solid State Ionics, 335 (2019) 7-14.

[145] C. Deviannapoorani, L. Dhivya, S. Ramakumar, R. Murugan, Journal of Power Sources, 240 (2013) 18-25.

[146] C. Dellen, H.G. Gehrke, S. Möller, C.L. Tsai, U. Breuer, S. Uhlenbruck, O. Guillon, M. Finsterbusch, M. Bram, Journal of Power Sources, 321 (2016) 241-247.

[147] A. Klump, C. Zhou, F.A. Stevie, R. Collazo, Z. Sitar, Journal of Vacuum Science & Technology B, 36 (2018) 03F102.

[148] M.S. Wagner, S.L. McArthur, M. Shen, T.A. Horbett, D.G. Castner, Journal of Biomaterials Science, Polymer Edition, 13 (2002) 407-428.

[149] M.E. Orazem, B. Tribollet, Electrochemical Impedance Spectroscopy, Wiley, 2011.

[150] Z. He, F. Mansfeld, Energy & Environmental Science, 2 (2009) 215-219.

[151] E. Barsoukov, Impedance spectroscopytheory, experiment, and applications, 2. ed. ed., Wiley-Interscience, Wiley-Interscience Hoboken, NJ, 2005.

[152] W. Zhang, D.A. Weber, H. Weigand, T. Arlt, I. Manke, D. Schröder, R. Koerver, T. Leichtweiss, P. Hartmann, W.G. Zeier, J. Janek, ACS Applied Materials & Interfaces, 9 (2017) 17835-17845.

[153] R. Koerver, I. Aygün, T. Leichtweiß, C. Dietrich, W. Zhang, J.O. Binder, P. Hartmann, W.G. Zeier, J. Janek, Chemistry of Materials, 29 (2017) 5574-5582.

[154] J.T.S. Irvine, D.C. Sinclair, A.R. West, Advanced Materials, 2 (1990) 132-138.

[155] A. Sakuda, A. Hayashi, M. Tatsumisago, Chemistry of Materials, 22 (2010) 949-956.

[156] P.W. Atkins, Physical chemistry, 4. ed., repr. with corr. ed., Oxford Univ. Press, Oxford Univ. Press 1992.

[157] C. Deviannapoorani, S. Ramakumar, N. Janani, R. Murugan, Solid State Ionics, 283 (2015) 123-130.

[158] G. Larraz, A. Orera, J. Sanz, I. Sobrados, V. Diez-Gómez, M.L. Sanjuán, Journal of Materials Chemistry A, 3 (2015) 5683-5691.

[159] S. Uhlenbruck, J. Dornseiffer, S. Lobe, C. Dellen, C.-L. Tsai, B. Gotzen, D. Sebold, M. Finsterbusch, O. Guillon, Journal of Electroceramics, 38 (2017) 197-206.

[160] A. Sharafi, S. Yu, M. Naguib, M. Lee, C. Ma, H.M. Meyer, J. Nanda, M. Chi, D.J. Siegel, J. Sakamoto, Journal of Materials Chemistry A, 5 (2017) 13475-13487.

[161] W. Xia, B. Xu, H. Duan, Y. Guo, H. Kang, H. Li, H. Liu, ACS Applied Materials & Interfaces, 8 (2016) 5335-5342.

[162] W. Xia, B. Xu, H. Duan, X. Tang, Y. Guo, H. Kang, H. Li, H. Liu, Journal of the American Ceramic Society, 100 (2017) 2832-2839.

[163] Y. Wang, W. Lai, Journal of Power Sources, 275 (2015) 612-620.

[164] Y. Li, Z. Wang, C. Li, Y. Cao, X. Guo, Journal of Power Sources, 248 (2014) 642-646.

[165] H. Takahara, T. Takeuchi, M. Tabuchi, H. Kageyama, Y. Kobayashi, Y. Kurisu, S. Kondo, R. Kanno, Journal of the Electrochemical Society, 151 (2004) A1539-A1544.

[166] E. Antolini, M. Ferretti, Journal of Solid State Chemistry, 117 (1995) 1-7.

[167] E. Antolini, Solid State Ionics, 170 (2004) 159-171.

[168] V.V.K. D. G. Kellerman, V. S. Gorshkov, Y. Blinovskov, Chemistry for Sustainable Development, 10 (2002) 721-726.

[169] L. Cheng, J.S. Park, H. Hou, V. Zorba, G. Chen, T. Richardson, J. Cabana, R. Russo, M. Doeff, Journal of Materials Chemistry A, 2 (2014) 172-181.

[170] Y. Matsuki, K. Noi, K. Suzuki, A. Sakuda, A. Hayashi, M. Tatsumisago, Solid State Ionics, 342 (2019) 115047.

[171] L. Cheng, W. Chen, M. Kunz, K. Persson, N. Tamura, G. Chen, M. Doeff, ACS Applied Materials & Interfaces, 7 (2015) 2073-2081.

[172] S. Yu, D.J. Siegel, Chemistry of Materials, 29 (2017) 9639-9647.
[173] E.A. Olevsky, Materials Science and Engineering: R: Reports, 23 (1998) 41-100.
[174] L. Cheng, M. Liu, A. Mehta, H. Xin, F. Lin, K. Persson, G. Chen, E.J. Crumlin, M. Doeff, ACS Applied Energy Materials, 1 (2018) 7244-7252.
[175] N. Janani, C. Deviannapoorani, L. Dhivya, R. Murugan, RSC Advances, 4 (2014) 51228-51238.
[176] N. Janani, S. Ramakumar, S. Kannan, R. Murugan, Journal of the American Ceramic Society, 98 (2015) 2039-2046.
[177] B.-Y. Chang, Journal of Electrochemical Science and Technology, 11 (2020) 318-321.
[178] Y. Ren, H. Deng, R. Chen, Y. Shen, Y. Lin, C.-W. Nan, Journal of the European Ceramic Society, 35 (2015) 561-572.
[179] J.N. Reimers, J.R. Dahn, Journal of the Electrochemical Society, 139 (1992) 2091-2097.
[180] J. Qian, L. Liu, J. Yang, S. Li, X. Wang, H.L. Zhuang, Y. Lu, Nature Communications, 9 (2018) 4918.
[181] K. Kishida, N. Wada, H. Adachi, K. Tanaka, H. Inui, C. Yada, Y. Iriyama, Z. Ogumi, Acta Materialia, 55 (2007) 4713-4722.
[182] H. Wakayama, Y. Kawai, Journal of Materials Chemistry A, 5 (2017) 18816-18822.
[183] J. Cho, Y.J. Kim, T.-J. Kim, B. Park, Angewandte Chemie International Edition, 40 (2001) 3367-3369.
[184] L. de Biasi, G. Lieser, C. Dräger, S. Indris, J. Rana, G. Schumacher, R. Mönig, H. Ehrenberg, J.R. Binder, H. Geßwein, Journal of Power Sources, 362 (2017) 192-201.
[185] E. Lee, B.J. Kwon, F. Dogan, Y. Ren, J.R. Croy, M.M. Thackeray, ACS Applied Energy Materials, 2 (2019) 6170-6175.
[186] M.R. Busche, T. Drossel, T. Leichtweiss, D.A. Weber, M. Falk, M. Schneider, M.-L. Reich, H. Sommer, P. Adelhelm, J. Janek, Nature Chemistry, 8 (2016) 426-434.
[187] J. Guo, H. Guo, A.L. Baker, M.T. Lanagan, E.R. Kupp, G.L. Messing, C.A. Randall, Angewandte Chemie International Edition, 55 (2016) 11457-11461.
[188] H. Leng, J. Huang, J. Nie, J. Luo, Journal of Power Sources, 391 (2018) 170-179.
[189] L. Le Van-Jodin, D. Rouchon, V.-H. Le, I. Chevalier, J. Brun, C. Secouard, Journal of Raman Spectroscopy, 50 (2019) 1594-1601.
[190] H. Porthault, R. Baddour-Hadjean, F. Le Cras, C. Bourbon, S. Franger, Vibrational Spectroscopy, 62 (2012) 152-158.
[191] F.S. Gittleson, K.P.C. Yao, D.G. Kwabi, S.Y. Sayed, W.-H. Ryu, Y. Shao-Horn, A.D. Taylor, ChemElectroChem, 2 (2015) 1446-1457.
[192] M. Duffiet, M. Blangero, P.-E. Cabelguen, C. Delmas, D. Carlier, The Journal of Physical Chemistry Letters, 9 (2018) 5334-5338.
[193] Y. Zhu, X. He, Y. Mo, ACS Applied Materials & Interfaces, 7 (2015) 23685-23693.
[194] T. Liu, Y. Zhang, R. Chen, S.-X. Zhao, Y. Lin, C.-W. Nan, Y. Shen, Electrochemistry Communications, 79 (2017) 1-4.
[195] T. Liu, Y. Ren, Y. Shen, S.-X. Zhao, Y. Lin, C.-W. Nan, Journal of Power Sources, 324 (2016) 349-357.
[196] R. Mücke, M. Finsterbusch, P. Kaghazchi, D. Fattakhova-Rohlfing, O. Guillon, Journal of Power Sources, 489 (2021) 229430.
[197] M. Nasir Khan, J. Bashir, Materials Research Bulletin, 41 (2006) 1589-1595.
[198] P.E. Blöchl, Physical Review B, 50 (1994) 17953-17979.
[199] G. Kresse, J. Furthmüller, Physical Review B, 54 (1996) 11169-11186.
[200] J.P. Perdew, K. Burke, M. Ernzerhof, Physical Review Letters, 77 (1996) 3865-3868.
[201] K. Okhotnikov, T. Charpentier, S. Cadars, Journal of Cheminformatics, 8 (2016) 17.
[202] A. Moradabadi, P. Kaghazchi, Solid State Ionics, 338 (2019) 74-79.

[203] S. Buta, D. Morgan, A. Ven, M. Aydinol, G. Ceder, Journal of the Electrochemical Society, 146 (1999) 4335-4338.
[204] B. Han, T. Paulauskas, B. Key, C. Peebles, J.S. Park, R.F. Klie, J.T. Vaughey, F. Dogan, ACS Applied Materials & Interfaces, 9 (2017) 14769-14778.
[205] T. Nakamura, K. Amezawa, J. Kulisch, W.G. Zeier, J. Janek, ACS Applied Materials & Interfaces, 11 (2019) 19968-19976.
[206] N. Ohta, K. Takada, I. Sakaguchi, L. Zhang, R. Ma, K. Fukuda, M. Osada, T. Sasaki, Electrochemistry Communications, 9 (2007) 1486-1490.
[207] K. Takada, N. Ohta, L. Zhang, K. Fukuda, I. Sakaguchi, R. Ma, M. Osada, T. Sasaki, Solid State Ionics, 179 (2008) 1333-1337.
[208] Y. Zhu, J.G. Connell, S. Tepavcevic, P. Zapol, R. Garcia-Mendez, N.J. Taylor, J. Sakamoto, B.J. Ingram, L.A. Curtiss, J.W. Freeland, D.D. Fong, N.M. Markovic, Advanced Energy Materials, 9 (2019) 1803440.
[209] S. Kim, V.I. Hegde, Z. Yao, Z. Lu, M. Amsler, J. He, S. Hao, J.R. Croy, E. Lee, M.M. Thackeray, C. Wolverton, ACS Applied Materials & Interfaces, 10 (2018) 13479-13490.
[210] T. Liu, Y. Ren, Y. Shen, S.-X. Zhao, Y. Lin, C.-W. Nan, Journal of Power Sources, 324 (2016) 349-357.
[211] T. Teranishi, Y. Yoshikawa, M. Yoneda, A. Kishimoto, J. Halpin, S. O'Brien, M. Modreanu, I.M. Povey, ACS Applied Energy Materials, 1 (2018) 3277-3282.
[212] K. Takada, N. Ohta, L.Q. Zhang, K. Fukuda, I. Sakaguchi, R. Ma, M. Osada, T. Sasaki, Solid State Ionics, 179 (2008) 1333-1337.
[213] S. Randau, D.A. Weber, O. Kötz, R. Koerver, P. Braun, A. Weber, E. Ivers-Tiffée, T. Adermann, J. Kulisch, W.G. Zeier, F.H. Richter, J. Janek, Nature Energy, 5 (2020) 259-270.
[214] M. Li, Z. Feng, P. Ying, Q. Xin, C. Li, Physical Chemistry Chemical Physics, 5 (2003) 5326-5332.
[215] M. Ramaswamy, T. Venkataraman, W. Werner, Angewandte Chemie International Edition, 46 (2007) 7778-7781.
[216] P. Colomban, A. Slodczyk, Acta Physica Polonica A, 116 (2009) 7-12.
[217] C. Snyder, C. Apblett, A. Grillet, T. Beechem, D. Duquette, Journal of the Electrochemical Society, 163 (2016) A1036-A1041.
[218] G. Chen, W. Hao, Y. Shi, Y. Wu, S. Perkowitz, Journal of Materials Research, 15 (2000) 583-585.
[219] Q. Hu, L. Lei, X. Jiang, Z.C. Feng, M. Tang, D. He, Solid State Sciences, 37 (2014) 103-107.
[220] J. Gong, W. Liu, J.-X. Li, C.-Z. Wang, Z.-G. Zong, G. Chen, Chemical Journal of Chinese Universities, 23 (2002) 102-104.
[221] F. Tietz, T. Wegener, M.T. Gerhards, M. Giarola, G. Mariotto, Solid State Ionics, 230 (2013) 77-82.
[222] E. Rossen, J.N. Reimers, J.R. Dahn, Solid State Ionics, 62 (1993) 53-60.
[223] D. Wohlmuth, V. Epp, P. Bottke, I. Hanzu, B. Bitschnau, I. Letofsky-Papst, M. Kriechbaum, H. Amenitsch, F. Hofer, M. Wilkening, Journal of Materials Chemistry A, 2 (2014) 20295-20306.
[224] L. Chen, Y. Li, S.-P. Li, L.-Z. Fan, C.-W. Nan, J.B. Goodenough, Nano Energy, 46 (2018) 176-184.
[225] L. Long, S. Wang, M. Xiao, Y. Meng, Journal of Materials Chemistry A, 4 (2016) 10038-10069.
[226] S. Yu, S. Schmohl, Z. Liu, M. Hoffmeyer, N. Schön, F. Hausen, H. Tempel, H. Kungl, H.D. Wiemhöfer, R.A. Eichel, Journal of Materials Chemistry A, 7 (2019) 3882-3894.
[227] R.C. Agrawal, G.P. Pandey, Journal of Physics D: Applied Physics, 41 (2008) 223001.
[228] K.M. Abraham, M. Alamgir, Journal of Power Sources, 43 (1993) 195-208.

[229] K.M. Abraham, M. Alamgir, Chemistry of Materials, 3 (1991) 339-348.
[230] W. Ping, C. Wang, R. Wang, Q. Dong, Z. Lin, A.H. Brozena, J. Dai, J. Luo, L. Hu, Science Advances, 6 (2020) eabc8641.
[231] C. Wang, W. Ping, Q. Bai, H. Cui, R. Hensleigh, R. Wang, A.H. Brozena, Z. Xu, J. Dai, Y. Pei, C. Zheng, G. Pastel, J. Gao, X. Wang, H. Wang, J.-C. Zhao, B. Yang, X. Zheng, J. Luo, Y. Mo, B. Dunn, L. Hu, Science, 368 (2020) 521.
[232] Q. Zhao, S. Stalin, C.-Z. Zhao, L.A. Archer, Nature Reviews Materials, 5 (2020) 229-252.
[233] F. Zheng, M. Kotobuki, S. Song, M.O. Lai, L. Lu, Journal of Power Sources, 389 (2018) 198-213.

List of Figures

List of Tables

Acknowledgements

I would like to thank the many colleagues and cooperation partners that helped me realize this work.

First, I want to thank Dr. Martin Finsterbusch for giving me the opportunity to work on the EvaBatt project (BMBF project, under the grant number 13XP0134A), that has funded my dissertation. I also want to thank Martin for the numerous scientific discussions that helped to proceed with my results and findings.

I want to thank Prof. Dr. Olivier Guillon to supervise me as “doctoral advisor” for my dissertation and his support and encouragement during me PhD time, and Prof. Dr. Egbert Figgemeier, who agreed to evaluate my dissertation as “reviewer” as well as Prof. Dr. Jesus Gonzalez as “referee”.

I also want to thank all my colleagues from the solid battery group, the battery department, and the institute.

Besides I acknowledge the support I received from the sintering group of Prof. Dr. Martin Bram. Their support enabled the fast progress in preparation of composite cathodes and half cells and by that gave me the chance to start with the electrochemical characterization. Here, I thank especially, Prof. Dr. Alexander M. Laptev and Ralf Steinert, who took time to teach me to operate the FAST/SPS and get many samples. Prof. Dr. Alexander M. Laptev further discussed my results with me and helped me to develop new ideas and improve my scientific talks, thank you.

Thanks to the many colleagues supporting me in the characterization of my samples. Marie-Theres Gerhards for the TGA measurements, Dr. Yoo Jung Sohn for help with the XRD results and Rietveld refinements, Dr. Enkhtsetseg Dashjav for the help with the polymer-ceramic ASSLBs, Mark Kappertz for showing me how to polish good SEM samples and polishing my samples for TEM, Dr. Doris Sebold and Daniel Grüner for collecting SEM images, Dr. Sandra Lobe and Walter Scheld for the Raman spectroscopy measurements and the discussion of the results, Dr. Sahir Naqash for the ToF-SIMS, Prof. Dr. Dina Fattakhova-Rohlfing for the help preparing my manuscripts and the many other colleagues that have contributed.

I also would like to thank my former colleague Dr. Chih-Long Tsai for his ideas for the first electrochemical characterizations.

I am very thankful for the detailed TEM analysis provided by Prof. Dr. Shih-kang Lin and Dr. Chih-hao Tu. Their interface characterizations helped to gain a detailed understanding of the processes in the composite cathode during the battery operation. I also thank Prof. Dr. Shih-kang Lin for allowing me to visit his group at NCKU, Taiwan. During my stay in Taiwan, I was also able to visit Prof. Dr. Bing Joe Hwang and get valuable insights into synchrotron characterization.

Also, the great simulation work performed by Dr. Payam Kaghazchi and Liang-Yin Kuo requires acknowledgement. Their simulations are one pillar to explain the degradation of garnet-based ASSLB.

Furthermore, I would like to thank my parents and family for the support and unconditional encouragement I have received along the way.

Band / Volume 558
Synthese von Cr_2AlC MAX-Phasen Kompositen und Bestimmung ihrer oxidativen Eigenschaften
T. Go (2021), ii, 119 pp
ISBN: 978-3-95806-598-7

Band / Volume 559
Distribution of Relaxation Times for Analysis of Solid Oxide Fuel Cell Stacks
K. Fitzek (2021), 237 pp
ISBN: 978-3-95806-599-4

Band / Volume 560
Machine Learning in Modeling of the Dynamics of Polymer Electrolyte Fuel Cells
W. Zou (2021), vii, 139 pp
ISBN: 978-3-95806-601-4

Band / Volume 561
Introduction Strategies for Hydrogen Infrastructure
S. Cerniauskas (2021), viii, 179 pp
ISBN: 978-3-95806-602-1

Band / Volume 562
Noble Metal Coated Porous Transport Layers for Polymer Electrolyte Membrane Water Electrolysis
C. Liu (2021), 139 pp
ISBN: 978-3-95806-603-8

Band / Volume 563
Modeling and Diagnosis of the Stratospheric Circulation
E. J. Charlesworth (2021), v, 103, A2 pp
ISBN: 978-3-95806-605-2

Band / Volume 564
Potentialfeldmessungen zur Qualitätsbewertung von Bipolarplatten
M. Sietmann (2021), ix, 160 pp
ISBN: 978-3-95806-606-9

Band / Volume 565
Sequential and coupled inversion of time-lapse borehole GPR measurements for vadose zone model parameterization
Y. Yu (2022), XX, 121 pp
ISBN: 978-3-95806-607-6

Band / Volume 566
Cirrus clouds in the extratropical tropopause and lowermost stratosphere region
I. Bartolomé García (2022), iii, 155 pp
ISBN: 978-3-95806-610-6

Band / Volume 567
Stationary and Transient Behaviour of Polymer Electrolyte Fuel Cells
Y. Shi (2022), viii, 172 pp
ISBN: 978-3-95806-611-3

Band / Volume 568
14th Carolus Magnus Summer School on Plasma and Fusion Energy Physics
D. Reiser (Ed.), (2022), 207 pp
ISBN: 978-3-95806-613-7

Band / Volume 569
Spectral induced polarization of calcite precipitation in porous media
S. Izumoto (2022), xviii, 106 pp
ISBN: 978-3-95806-614-4

Band / Volume 570
Technische und ökonomische Bewertung der Polymer-Elektrolyt-Membran Elektrolyse
S. M. Saba (2022), IV, 263 pp
ISBN: 978-3-95806-615-1

Band / Volume 571
Advanced Sintering of Garnet-Based Ceramic Composite Cathodes for All-Solid-State Lithium Batteries
M. Ihrig (2022), VIII, 160 pp
ISBN: 978-3-95806-616-8

Weitere ***Schriften des Verlags im Forschungszentrum Jülich*** unter
http://wwwzb1.fz-juelich.de/verlagextern1/index.asp

Energie & Umwelt / Energy & Environment
Band / Volume 571
ISBN 978-3-95806-616-8

Mitglied der Helmholtz-Gemeinschaft

JÜLICH
Forschungszentrum